Boston University

OpenBU **http://open.bu.edu**

Boston University Theses & Dissertations Boston University Theses & Dissertations

2023

Mechanical and failure mechanisms of descending thoracic aorta: implications for health and disease

https://hdl.handle.net/2144/46260

Downloaded from DSpace Repository, DSpace Institution's institutional repository

BOSTON UNIVERSITY

COLLEGE OF ENGINEERING

Dissertation

MECHANICAL AND FAILURE MECHANISMS OF DESCENDING THORACIC AORTA: IMPLICATIONS FOR HEALTH AND DISEASE

by

RUIZHI WANG

B.E., Huazhong University of Science and Engineering, 2015
M.S., University of Florida, 2017

Submitted in partial fulfillment of the

requirements for the degree of

Doctor of Philosophy

2023

© 2023 by
RUIZHI WANG
All rights reserved

Approved by

First Reader

Katherine Yanhang Zhang, Ph.D.
Professor of Mechanical Engineering
Professor of Biomedical Engineering
Professor of Materials Science and Engineering

Second Reader

Béla Suki, Ph.D.
Professor of Biomedical Engineering
Professor of Materials Science and Engineering

Third Reader

Michael B. Albro, Ph.D.
Assistant Professor of Mechanical Engineering
Assistant Professor of Materials Science and Engineering
Assistant Professor of Biomedical Engineering

Fourth Reader

Joyce Y. Wong, Ph.D.
Professor of Biomedical Engineering
Professor of Materials Science and Engineering

DEDICATION

To my family.

ACKNOWLEDGMENTS

First and foremost, I would like to express my sincere gratitude to my advisor, Dr. Katherine Yanhang Zhang, for her support and guidance throughout the past six years. Dr. Zhang's passion and unparalleled vision for soft tissue biomechanics has always been a source of inspiration and motivation for me. This dissertation would not have been completed without her trust, patience and selfless mentorship, which has made me grow not only as a researcher but also as a person.

I would also like to thank other members of my dissertation committee, Dr. Bela Suki, Dr. Michael Albro and Dr. Joyce Wong, for their insightful comments and constructive feedback to my research.

I appreciate the friendship and enjoyable time spent together with members of the Multi-Scale Tissue Biomechanics Lab: Anastasia Gkousioudi, Xiaozhu Liu, Nicholas Milkovich and Samuel Halvorsen. I am deeply grateful to Dr. Xunjie Yu for offering me help constantly both in research and in life.

I would like to thank my parents and my in-laws for their support and understanding. Most of all, I thank my wife Xiaoyu Chen for her love, tolerance, and optimism; and my daughter Ivy Wang for the happiness she brings to me.

MECHANICAL AND FAILURE MECHANISMS

OF DESCENDING THORACIC AORTA:

IMPLICATIONS FOR HEALTH AND DISEASE

RUIZHI WANG

Boston University College of Engineering, 2023

Major Professor: Katherine Yanhang Zhang, Ph.D., Professor of Mechanical Engineering, Professor of Biomedical Engineering, Professor of Materials Science and Engineering

ABSTRACT

Structural organization of the extracellular matrix components of the aorta is critical to its loading-bearing capacity and homeostasis. Aortic elastic fibers form concentric lamellar layers with a closely interwoven three-dimensional network of collagen and elastic fibers in the narrow interlamellar space. Aging and cardiovascular diseases are closely associated with disrupted microstructural organization, integrity, as well as altered mechanical and failure properties of the aortic wall. The overall goal of this research is to advance the current understanding of the mechanical and failure mechanisms of human descending thoracic aorta and provide insights for aortic remodeling during aging and disease progression using integrated biomechanical testing, imaging, and computational modeling approaches.

Biaxial tensile tests revealed anisotropic stiffening of the aortic wall with aging with a more drastic stiffening behavior in the longitudinal direction. A newly developed constitutive model considering collagen crosslinking suggested that collagen crosslinking has an increasing contribution to the stress-stretch behavior and elastic energy storage in

aortic senescence. The aorta relies on interlamellar structural components, mainly elastic and collagen fibers, for maintaining its structural and mechanical integrity. Our study using peeling and direct tension tests demonstrated that elastic and collagen fibers both play an important role in bonding of the arterial wall, while collagen fibers dominate the interlamellar stiffness, strength and toughness. Our study further reveals that the interlamellar strength and toughness both increase due to nonenzymatic glycation, which is in accordance with the reported inverse relation between diabetes and a reduced risk of aortic dissection. On the other hand, however, our study showed decreasing interlamellar bonding toughness of the medial layer of human descending thoracic aorta with aging. Avalanches and power-law behavior in dissection propagation was found for all age groups investigated. Finite element simulations incorporating discrete interlamellar collagen fibers successfully recapitulates the power-law behavior and points to prominent structural alterations in interlamellar collagen fibers with aging including reduced fiber density and higher degree of dispersion.

In aging and diseases, changes to the extracellular matrix microstructure can trigger a cascade of effects on tissue and cellular function. The knowledge gained from this research provide insights into the microstructural mechanisms in determining the physiological and failure properties of aorta and will potentially generate clinical impact on the developments of new diagnostics and interventions.

TABLE OF CONTENTS

DEDICATION…….. iv

ACKNOWLEDGMENTS v

ABSTRACT……..... vi

TABLE OF CONTENTS..... viii

LIST OF TABLES…..... xii

LIST OF FIGURES… xiv

CHAPTER 1 INTRODUCTION 1

1.1 Objectives 1

1.2 Microstructure of the aorta 1

1.3 Aortic remodeling in cardiovascular diseases 3

1.4 Outline of research..... 4

CHAPTER 2 EXPERIMENTAL METHODS 7

2.1 Overview..... 7

2.2 Biaxial tensile test..... 7

2.3 Peeling test..... 8

2.4 Direct tension test 9

2.5 Multiphoton microscopy..... 10

CHAPTER 3 EFFECT OF AGING ON THE BIAXIAL MECHANICAL BEHAVIOR OF HUMAN DESCENDING THORACIC AORTA: EXPERIMENTS AND CONSTITUTIVE MODELING CONSIDERING COLLAGEN CROSSLINKING 12

3.1 Overview..... 12

3.2 Introduction 13
3.2 Material and methods 16
3.2.1 Sample preparation 16
3.2.2 Planar biaxial tensile testing 17
3.2.3 Constitutive model development 18
3.2.4 Parameter estimation 23
3.2.5 Statistical analysis 25
3.3 Results 25
3.4 Discussion 37
3.5 Limitations 43
3.6 Conclusions 44
CHAPTER 4 MECHANICAL AND STRUCTURAL CONTRIBUTIONS OF ELASTIN AND COLLAGEN FIBERS TO INTERLAMELLAR BONDING IN THE ARTERIAL WALL 46
4.1 Overview 46
4.2 Introduction 47
4.3 Material and methods 51
4.3.1 Sample preparation 51
4.3.2 Peeling test 53
4.3.3 Planar biaxial tensile test 53
4.3.4 Statistical analysis 54
4.3.5 Finite element model setup 54

4.3.6 Constitutive modeling 57
4.3.7 Identification of model parameters 58
4.3.8 Multiphoton imaging 62
4.3 Results 63
4.4 Discussions 68
4.5 Limitations 73
4.6 Conclusions 75
CHAPTER 5 EFFECT OF GLYCATION ON INTERLAMELLAR BONDING OF ARTERIAL ELASTIN 76
5.1 Overview 76
5.2 Introduction 77
5.3 Material and Methods 80
5.3.1 Sample preparation 80
5.3.2 Peeling test 80
5.3.3 Direct tension test 81
5.3.4 Statistical analysis 82
5.3.5 Multiphoton imaging 84
5.3.6 Finite element modeling of peeling test 84
5.3.7 Constitutive modeling of elastin network 87
5.4 Results 88
5.5 Discussion 98
5.6 Limitations 104

5.7 Conclusions 105
CHAPTER 6 EFFECT OF AGING ON THE DISSECTION BEHAVIOR OF HUMAN DESCENDING THORACIC AORTA 106
6.1 Overview 106
6.2 Introduction 107
6.3 Material and methods 109
6.3.1 Sample preparation 109
6.3.2 Peeling test 110
6.3.3 Model setup and implementation 111
6.3.4 Statistical analysis 114
6.4 Results 115
6.5 Discussion 120
6.6 Conclusions 122
CHAPTER 7 CONCLUSIONS AND OUTLOOK 124
7.1 Conclusions 124
7.2 Outlook 126
APPENDIX A KINEMATICS OF BONDED FIBER AND CROSSLINK UNDER BIAXIAL TENSION 128
BIBLIOGRAPHY…. 133
CURRICULUM VITAE 154

LIST OF TABLES

Table 3.1 Age, gender and selected medical information of human descending thoracic aorta donors used in this study. HTN - hypertension; HLP - hyperlipidemia; BMI - body mass index; F - female; M - male; Y - yes; N - no; * - during pregnancy; SIGSW - self-inflicted gunshot wound; MVA - motor vehicle accident; CPA - cardiopulmonary arrest; CVA - cerebrovascular accident; ABI - anoxic brain injury; HD - heart disease; COPD - chronic obstructive pulmonary disease. 18

Table 3.2 Model parameters of the two-fiber family model without considering the effect of crosslinking, and the associated root mean square error (RMSE), coefficient of determination (R^2), and corrected Akaike information criterion (AIC_C) as measures of the goodness of fit. Two samples were obtained from each aorta except for N8 and N16. In the column of "Sample", numbers 1 and 2 in the parentheses denote the first and second sample obtained from the corresponding aorta..... 32

Table 3.3 Model parameters of the two-fiber family model considering the effect of crosslinking, and the associated root mean square error (RMSE), coefficient of determination (R^2), and corrected Akaike information criterion (AIC_C) as measures of the goodness of fit. Two samples were obtained from each aorta except for N8 and N16. In the column of "Sample", numbers 1 and 2 in the parentheses denote the first and second sample obtained from the corresponding aorta..... 33

Table 3.4 Correlation coefficients and p-values of the correlation between age and model parameters as well as crosslinking-related strain energy contributions. μ - shear modulus of the non-collagenous components, θ - the angle between collagen fiber orientation and the longitudinal direction of the aorta, α_0 - angle between orientations of bonded crosslink and fiber, W_c - strain energy density of crosslink stretch, W_{cf} - strain energy density of crosslink-fiber interaction, W - total strain energy density. 37

Table 4.1 Material parameters for the anisotropic hyperelastic behavior of arterial media and elastin network. 61

Table 4.2 Material parameters for the cohesive zones of arterial media and elastin network. (Circ: circumferential; Long: longitudinal; G_c: energy release rate; $\delta 0$: separation distance at damage initiation; t_0: traction at damage initiation; K: initial interlamellar stiffness; δ_c: separation distance at complete delamination; MAPE: mean absolute percentage error). 65

Table 5.1 Material parameters for the constitutive model of arterial elastin in Equation 5.2 for the untreated and glucose treated elastin, and the value of the objective function in Equation 5.3..... 88

Table 5.2 Experimental results of peeling force (F), energy release rate (G_c) from peeling test; and interlamellar strength (t_{DT}) from direct tension test (Circ: circumferential; Long: longitudinal). 92

Table 5.3 Material parameters for the CZM of arterial elastin before and after glucose treatment. (Circ: circumferential; Long: longitudinal; G_c: energy release rate; δ_i: separation distance at damage initiation; t_{CZM}: traction at damage initiation; δ_c: separation distance at complete delamination; MAPE: mean absolute percentage error). 92

Table 6.1. Age, gender and selected medical information of the donor of the additional human descending thoracic aorta used in this study. HTN - hypertension; HLP - hyperlipidemia; BMI = body mass index; M = male; Y=yes; CHF = congestive heart failure. 110

Table 6.2 Interlamellar fiber structural parameters including the number of fibers per 2 mm of bonded length and the maximum angle of interlamellar fiber dispersion (θ) estimated from finite element simulations. 120

LIST OF FIGURES

Figure 1.1. Microstructure of the aortic wall (Holzapfel et al. 2000). 2

Figure 1.2. Three-dimensional scanning electron microscopy images showing the architecture of arterial elastin (O'Connell et al. 2008). 3

Figure 3.1 Schematic of a sample with two families of collagen fibers and crosslinks. $E_{1,2}$ is the unit vector in the orientation of collagen fibers; $E_{1,2R}$ is the unit vector normal to the orientation of collagen fibers; $L_{1,2}^{\pm}$ is the unit vector in the orientation of crosslinks; θ denotes the angle between the longitudinal direction of the aorta and the orientation of collagen fibers; and α_0 denotes the angle between the orientations of collagen fibers and their associated crosslinks. 20

Figure 3.2 Cauchy stress-stretch curves in the circumferential and longitudinal directions of human descending thoracic aortas under 200 N/m equibiaxial tension test from the <40 yrs (years), 40-60 yrs, and >60 yrs age groups. 28

Figure 3.3 Effect of aging on a peak stretch and b tangent modulus of human descending thoracic aortas under 200 N/m equibiaxial tensile test. Boxes in the plots represent the middle 50% (from the first quartile to the third quartile) of the data set; the horizontal line inside the box represents the median; the cross symbol represents the mean; and the dotted symbols represent individual data points. (*p<0.05, **p<0.01, ***p<0.001, ****p<0.0001) 29

Figure 3.4 Effect of aging on the degree of anisotropy (DA) of human descending thoracic aortas under 200 N/m equibiaxial tensile test. The absolute value of DA increases suggesting a more anisotropic behavior of the sample. A positive DA corresponds to a higher circumferential stiffness while a negative DA corresponds to a higher longitudinal stiffness. Boxes in the plot represent the middle 50% (from the first quartile to the third quartile) of the data set; the horizontal line inside the box represents the median; the cross symbol represents the mean; and the dotted symbols represent individual data points. (*p<0.05) 29

Figure 3.5 Representative curve fitting results of the two-fiber family model without considering the effect of crosslinking. Symbols represent experimental data and curves represent constitutive model fitting. 35

Figure 3.6 Representative curve fitting results of the two-fiber family model considering the effect of crosslinking. Symbols represent experimental data and curves represent constitutive model fitting. 36

Figure 3.7 Comparison of a root mean square error (RMSE), b coefficient of determination (R^2) and c corrected Akaike information criterion (AIC_C) as

measurements of the goodness of fit for the two-fiber family model (2FF) and the two-fiber family with crosslinking model (2FFC). Boxes in the plots represent the middle 50% (from the first quartile to the third quartile) of the data set; the horizontal line inside the box represents the median; the cross symbol represents the mean; and the dotted symbols represent individual data points. (**p<0.01, ***p<0.001, ****p<0.0001)..... 38

Figure 3.8 Contributions of the strain energy density due to a crosslink deformation (W_c) and b crosslink-fiber interaction (W_{cf}) to the total strain energy density (W) of human descending thoracic aorta samples under 200 N/m equibiaxial tensile test. Boxes in the plots represent the middle 50% (from the first quartile to the third quartile) of the data set; the horizontal line inside the box represents the median; the cross symbol represents the mean; and the dotted symbols represent individual data points. (*p<0.05, **p<0.01)..... 39

Figure 4.1 a A rectangular porcine aorta sample; and b mode-I peeling test of the aortic media..... 52

Figure 4.2 Three-dimensional finite element model of mode-I peeling of the arterial media. a Undeformed configuration; b deformed configuration; c and d detailed views of the cohesive elements (blue) sandwiched between the brick elements (gray) in the undeformed configuration; and e detailed view of the damaged zone containing 9 rows of cohesive elements in the simulation of damage propagation in the deformed configuration..... 56

Figure 4.3 Bilinear traction-separation law for the cohesive elements..... 57

Figure 4.4 a A representative peeling force/width-displacement curve and its zoom-in graphs showing the high frequency oscillation of the peeling force; and b-e distribution of Δd from peeling tests of aortic media and elastin in the circumferential (Circ) and longitudinal (Long) directions. Dashed lines in b-e indicate the location of the median. Note that the vertical axis in b-e are in the logarithmic scale. 60

Figure 4.5 Experimental Cauchy stress-stretch curves of biaxial tensile tests of porcine aortic media in the a circumferential and b longitudinal directions. The thick black curves represent the arithmetic means. 61

Figure 4.6 a The custom-built device for multiphoton imaging of the peeling forefront; b experimental setup of multiphoton imaging of peeling of aortic tissues in the circumferential direction and c longitudinal direction with preferred orientation of in-plane fiber distribution; d-f multiphoton image of different depth of the peeling site of porcine aortic media obtained from a circumferential tissue strip and g-i a longitudinal tissue strip. Imaging depth increases from d to f and from g to i. 62

Figure 4.7 Experimental (gray) and simulated (black) curves of peeling force/width-displacement for aortic media and purified elastin network in the a circumferential and b longitudinal directions. 64

Figure 4.8 a-c Experimental and d-f simulation results from peeling of aortic media and purified elastin network in the circumferential and longitudinal directions. ($^{*}p<0.05$). 66

Figure 4.9 Traction-separation relations for the cohesive zone of aortic media and purified elastin network determined from peeling tests in the circumferential and longitudinal directions. Inset figure shows the initial regime of the cohesive zone. (Circ=circumferential, Long=longitudinal). 66

Figure 5.1 Schematic of the experimental setup for a peeling and b direct tension tests. 81

Figure 5.2 Custom-built device for multiphoton imaging of the separation site (inset pictures) of arterial elastin during a peeling and e direct tension tests; b-d multiphoton images of the dissection site in peeling of a circumferential porcine arterial elastin strip at different imaging depths (imaging depth increases from b to d); and f-h multiphoton images of different sub-locations of the separation site in direct tension of porcine arterial elastin. 83

Figure 5.3 a Bilinear traction-separation law for the cohesive zone model; and b a representative peeling force/width-displacement curve and its zoom-in graphs showing the high frequency oscillation of the peeling force and the displacement increment (Δd) associated with a ramp up of the peeling force..... 85

Figure 5.4 Experimental and simulated curves of peeling force/width vs. displacement from peeling of arterial elastin in the circumferential (Circ) and longitudinal (Long) directions before (a and e) and after (b-d and f-h) glucose treatment. 90

Figure 5.5 a and b peeling force per unit tissue width (F); and c and d energy release rate (G_c) of arterial elastin for untreated, glucose treated (7, 14, and 21 days), and PBS treated (21days) in the circumferential and longitudinal directions. The box represents the middle 50% (from the first quartile to the third quartile) of the data set; the horizontal line inside the box represents the median; the cross symbol represents the mean; the red dots represent individual data points. ($^{*}p<0.05$, $^{**}p<0.01$). 91

Figure 5.6 Probability distribution of the displacement increment (Δd) associated with each ramp up of the peeling force from peeling tests of arterial elastin in the a-d circumferential (Circ) and e-h longitudinal (Long) directions before and after glucose treatment; and whisker plots of the distribution of Δd with varying durations of glucose treatment in the i circumferential and j longitudinal directions. The box in the whisker plots represents the middle 50% (from the first quartile to the third

quartile) of the data set; the horizontal line inside the box represents the median; the cross represents the mean; individual data points are not shown in i and j because of the large size of the data set. Red lines in a-h indicate the location of the median; note that the vertical axis in a-j are in logarithmic scale. ($^{*}p<0.05$, $^{**}p<0.01$). 93

Figure 5.7 a A representative force-displacement curve obtained from the direct tension test of arterial elastin; and b pictures showing different stages of a sample during direct tension test: I elastic deformation, II damage onset, III peeling-like damage mode, and IV complete separation. c-f Force-displacement curves from direct tension tests of arterial elastin c before and d-f after glucose treatment. 96

Figure 5.8 Interlamellar strength obtained from direct tension tests (t_{DT}) as well as estimated values from finite element simulations of peeling tests (t_{CZM}) for arterial elastin before and after glucose treatment. The box in the whisker plots represents the middle 50% (from the first quartile to the third quartile) of the data set; the horizontal line inside the box represents the median; the cross represents the mean; red dots represent individual data points. (*p<0.05, **p<0.01). 97

Figure 5.9 Traction-separation relations for the cohesive zone of untreated and glucose treated arterial elastin determined from peeling tests in the a circumferential and b longitudinal directions. 97

Figure 6.1 A representative experimental peeling force/width (F/W) – displacement curve of human descending thoracic aortic media and its zoom-in graphs showing the high frequency oscillation of the peeling force and the drop of peeling force/width ($\Delta F/W$). 111

Figure 6.2 Finite element model (a) and a local zoom-in view (b) showing nonuniformly oriented interlamellar fibers. θ denotes the (maximum) degree of interlamellar fiber dispersion and d denotes interlamellar distance. A representative peeling force/width (F/W) – displacement curve obtained from finite element simulations is shown in c. 112

Figure 6.3 Experimental curves of peeling force/width (F/W) vs. displacement from peeling tests of human descending thoracic aortic media in the circumferential and longitudinal directions. 116

Figure 6.4 Changes of the mean peeling force/width (a) and energy release rate (b) of human descending thoracic aortic media with aging in the circumferential and longitudinal directions. Error bars represent standard error of the mean (SEM). (*p<0.05, **p<0.01) 116

Figure 6.5 Changes of the thickness of aortic media (a) and shear modulus (b) of human descending thoracic aortic media with aging. Error bars represent standard error of the mean (SEM). (*p<0.05) 117

Figure 6.6 Double logarithmic plots of the probability density ($\Pi\Delta F/W$) distribution of force drop/width ($\Delta F/W$). Experimental data are shown in black and simulation data are shown in red. The straight lines represent the best power-law fit to the data. In the figure legend, subscripts "EXP" and "SIM" denote experimental and simulation data, respectively. 119

Figure 6.7 Correlation between the number of interlamellar fibers and the interlamellar energy release rate (G_c) for both the circumferential and longitudinal directions. Straight dashed lines represent the best linear fit. The correlation coefficient ® and the p-value of the correlation analysis are given. 120

Figure A.1 Change of a $\cos\alpha + \cos\alpha_0$ and b $\cos\alpha$-$\cos(180°\text{-}\alpha_0)$ with varying θ (the angle between the longitudinal direction of the aortic sample X_1 and collagen fiber direction E_1) and α_0 (the angle between collagen fiber direction E_1 and crosslink direction L_1^+) when the biaxial stretch ratio between the circumferential (λ_2) and longitudinal (λ_1) directions is 2:1. 130

Figure A.2 Change of a $\cos\alpha + \cos\alpha_0$ and b $\cos\alpha$-$\cos(180°\text{-}\alpha_0)$ with varying θ (the angle between the longitudinal direction of the aortic sample X_1 and collagen fiber direction E_1) and α_0 (the angle between collagen fiber direction E_1 and crosslink direction L_1^+) when the biaxial stretch ratio between the circumferential (λ_2) and longitudinal (λ_1) directions is 4:3. 130

Figure A.3 Change of a $\cos\alpha + \cos\alpha_0$ and b $\cos\alpha$-$\cos(180°\text{-}\alpha_0)$ with varying θ (the angle between the longitudinal direction of the aortic sample X_1 and collagen fiber direction E_1) and α_0 (the angle between collagen fiber direction E_1 and crosslink direction L_1^+) when the biaxial stretch ratio between the circumferential (λ_2) and longitudinal (λ_1) directions is 1:1. 131

Figure A.4 Change of a $\cos\alpha + \cos\alpha_0$ and b $\cos\alpha$-$\cos(180°\text{-}\alpha_0)$ with varying θ (the angle between the longitudinal direction of the aortic sample X_1 and collagen fiber direction E_1) and α_0 (the angle between collagen fiber direction E_1 and crosslink direction L_1^+) when the biaxial stretch ratio between the circumferential (λ_2) and longitudinal (λ_1) directions is 3:4. 131

Figure A.5 Change of a $\cos\alpha + \cos\alpha_0$ and b $\cos\alpha$-$\cos(180°\text{-}\alpha_0)$ with varying θ (the angle between the longitudinal direction of the aortic sample X_1 and collagen fiber direction E_1) and α_0 (the angle between collagen fiber direction E_1 and crosslink direction L_1^+) when the biaxial stretch ratio between the circumferential (λ_2) and longitudinal (λ_1) directions is 1:2. 132

CHAPTER 1 INTRODUCTION

1.1 Objectives

The aorta is the main artery in human body that delivers the blood from the left ventricle of the heart to the branch arteries and further to the rest of the body. The proper function of aorta, which is of critical importance to our health, depends on the structural organization of its extracellular matrix (ECM) components. An aorta is primarily composed of collagen and elastin, two major structural proteins that form a complex three-dimensional (3D) network and endow the tissue its load-bearing and damage-resisting capacities. Cardiovascular diseases are the leading cause of death in most countries of the world (Bonow et al. 2002; Everson-Rose and Lewis 2005), and are associated with disrupted microstructural organization and integrity as well as altered mechanical and failure properties of the aortic wall (Humphrey 2002; Pasta et al. 2012). Using a combination of mechanical testing, computational modeling and imaging methods, this dissertation aims to advance the current understanding of the mechanical and failure properties of the aorta and provide insights for aortic remodeling in aging and diseases.

1.2 Microstructure of the aorta

The aortic wall is a laminated structure with three distinct layers: the adventitia, media and intima (Figure 1.1). The adventitia is the outermost layer which is in contact with loose connective tissues and protects the aortic wall from overstretch and rupture. It is consisted of fibroblasts and fibrocytes, helically arranged wavy type I collagen fibers,

and ground substances (Holzapfel et al. 2000). The intima is the innermost layer that is composed of a single layer of endothelial cells and an underlying basal membrane. It has important biological functions most of which are correlated with blood-flow induced shear stresses, but has little contribution to the mechanical properties of a healthy aorta (Holzapfel et al. 2000; Humphrey and Na 2002). From a mechanical perspective, aortic media plays a crucial role in a healthy aorta (Holzapfel et al. 2000). It is consisted of collagen (types I, III and V), elastic fibers, GAGs and smooth muscle cells (SMCs). Aortic media can be further divided into a number of concentric layers each defined by a fenestrated elastic lamella (Wolinsky and Glagov 1964, 1967). Together with collagen fibers and radially-running elastic fibers in the interlamellar space, a 3D network is formed for SMCs to reside in (O'Connell et al. 2008; Wagenseil and Mecham 2009), as shown in Figure 1.2.

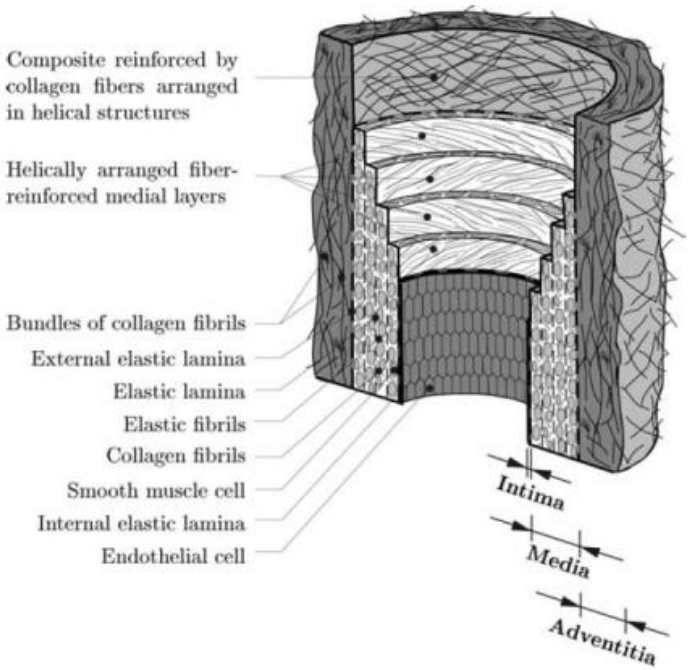

Figure 1.1. Microstructure of the aortic wall (Holzapfel et al. 2000).

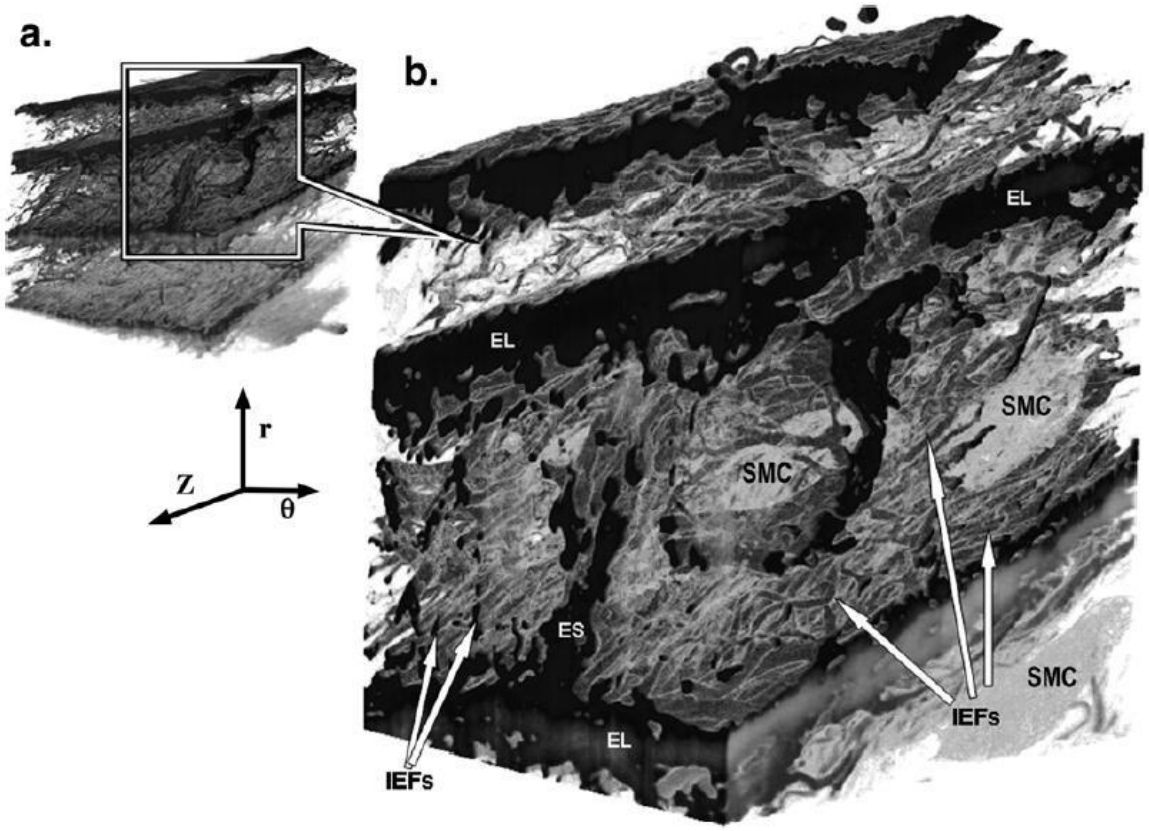

Figure 1.2. Three-dimensional scanning electron microscopy images showing the architecture of arterial elastin (O'Connell et al. 2008).

1.3 Aortic remodeling in cardiovascular diseases

Aortic remodeling is a commonly observed pathological process in the progression of cardiovascular diseases. Diabetes is known to accelerate aging induced stiffening of the aorta by nonenzymatic glycation (Vlassara et al. 1986; Cameron et al. 2003). Glucose molecules react with the residual group of proteins to form advanced glycation end-products (AGEs) which induce intermolecular crosslinking of structural proteins (Brownlee et al. 1988), ultimately causing ECM fiber stiffening and aggregation (Silverstein et al. 2015; De et al. 2020). Aortic aneurysms are local dilatations of the aortic wall initiated by loss of elastic fibers and SMCs (Humphrey and Holzapfel 2012).

An enlarging aortic aneurysm is accompanied by increased wall stress and decreased wall strength (Vorp 2007). One of the most lethal complications of an aneurysm is aortic dissection. It begins with a tear in the intima, which permits blood flow to enter the media and separate the elastic lamellae (Sherifova and Holzapfel 2019); rupture of the arterial wall occurs when damage propagates radially across lamellae (Sommer et al. 2008). Propagation of aortic dissection leads to local buildup of strain energy followed by avalanches of elastin and collagen fibers (Yu et al. 2020). In addition, aging is a prominent predisposing factor of cardiovascular diseases (Dernellis and Panaretou, 2005; Riambau et al., 2017). The aorta stiffens with age (Jadidi et al., 2020) and undergoes profound compositional and structural alterations including but not limited to elastin fragmentation, increase of collagen concentration and crosslinking, SMC stiffening and ECM fiber reorientation and straightening (Spina and Garbin, 1976; Schlatmann and Becker, 1977; Toda et al., 1980; Brüel and Oxlund 1996; Haskett et al. 2010; Qiu et al., 2010; Wheeler et al., 2015; Amabili et al., 2021; Cavinato et al., 2021; Franchini et al., 2021). As shown by these examples, a more in-depth understanding of the biomechanics and mechanobiology of the aortic wall in healthy and diseased conditions will greatly benefit the prevention, diagnosis and treatment of cardiovascular diseases.

1.4 Outline of research

This dissertation combines mechanical testing, imaging and computational modeling to investigate the mechanical and structural properties of the descending thoracic aorta in health and disease. In Chapter 2, the experimental methods utilized in

this research are introduced, including biaxial tensile test, peeling test, direct tension test and multiphoton imaging.

In Chapter 3, changes of the biaxial mechanical behavior of human descending thoracic aorta with aging were investigated. Planar biaxial tensile tests were performed to assess the stiffness and anisotropy of the descending thoracic aortic wall of different age groups. A novel constitutive model incorporating collagen crosslinking into the two-fiber family model was developed to describe the biaxial mechanical response. The role of collagen crosslinking in aging-induced aortic stiffening was analyzed based on its contribution to the stress-stretch behavior and strain energy density of the aorta under biaxial tension.

In Chapter 4, the mechanical and structural contributions of arterial elastin and collagen fibers to interlamellar bonding were studied through peeling test, multiphoton imaging and finite element modeling. The interfacial energy release rate was obtained from peeling tests. Cohesive zone model based simulations of peeling test provided a comprehensive description of the interlamellar bonding behavior of aortic media and elastin. Multiphoton imaging was used to demonstrate the recruitment pattern of both elastin and collagen fibers within the interlamellar space during dissection.

In Chapter 5, effects of glycation on the interlamellar bonding properties of arterial elastin were examined. Peeling and direct tension tests were performed to provide complimentary information on understanding the interlamellar layer separation properties of elastin network with glycation effect. Peeling tests were simulated using a cohesive zone model to extract more detailed properties of elastin interlamellar bonding.

Multiphoton imaging was used to visualize the interlamellar elastin fibers in samples subjected to peeling and direct tension.

In Chapter 6, effects of aging on the interlamellar dissection properties of the medial layer of human descending thoracic aorta were studied. Peeling tests were conducted to evaluate the force and energy release rate as well as the avalanche and power-law behavior in dissection propagation. A finite element model considering failure of discrete interlamellar collagen fibers was employed to simulate interfacial fracture. Mechanical and structural alterations of the interlamellar collagen fibers with aging were elucidated by fitting the simulated power-law exponent to that measured from experiments.

In Chapter 7, conclusions and potential directions for future work are presented.

CHAPTER 2 EXPERIMENTAL METHODS

2.1 Overview

This chapter gives an introduction to the experimental methods used in this dissertation, including biaxial tensile test, peeling test, direct tension test and multiphoton microscopy.

2.2 Biaxial tensile test

Samples were cut into approximately 2 cm × 2 cm square patches. Four carbon dots were glued to the center of the sample surface. Four hooks were placed on each edge of a sample and were connected to actuators of a custom-built tester with sutures. Stretches of the sample in both the circumferential and longitudinal directions were obtained by tracking the displacement of the carbon dots with a CCD camera. The thickness and effective edge length (hook-to-hook distance) in both the circumferential and longitudinal directions of each sample were measured using a caliper. The sample was submerged in phosphate buffered saline (PBS) solution during testing. A preload of 5 N/m was applied to both the circumferential and longitudinal directions to straighten the sample so that the initial configuration of the sample was defined. 8 cycles of 40 N/m equibiaxial tensile loads were applied to the sample as preconditioning to achieve repeatable mechanical response. Then, the sample was subjected to 8 cycles of 300 N/m equibiaxial tensile loads with a half cycle time of 10 seconds. Data from the last cycle was used for analysis. Assuming tissue incompressibility, Cauchy stresses can be calculated as (Zou and Zhang 2009)

$$\sigma_1 = \frac{F_1\lambda_1}{L_{02}t}, \quad \sigma_2 = \frac{F_2\lambda_2}{L_{01}t} \tag{2.1}$$

where σ is the Cauchy stress, F is the applied force, λ is the stretch, L_0 is the initial effective edge length, and t is the initial sample thickness. The subscripts 1 and 2 denote the longitudinal and circumferential directions.

2.3 Peeling test

Samples were cut into approximately 40 mm × 10 mm rectangular strips. The long axis of each sample was oriented in either the circumferential direction or the longitudinal direction. Damage was initiated in each sample by making an incision of about 10 mm into the middle of the thickness and creating two "tongues" with approximately equal thickness. To make the initial incision, a surgical scalpel was held parallel to the surface of a sample and was carefully cut into the middle of the thickness of the sample. Next, the delamination forefront and the two separated "tongues" were visually inspected. In the case that any in-plane damage of the lamellae adjacent to the incision was inspected, the sample was rejected. The thickness, width and bonded length of the sample was measured using a digital caliper. Sandpaper tabs were glued to the two "tongues" and clamped by grips attached to a uniaxial tensile tester (Instron, Norwood, MA, USA). Steady-state mode-I peeling test was carried out by fixing one "tongue" of the sample and pulling away the other "tongue" with an extension rate of 0.2 mm/s. The test terminated when the sample completely delaminated. The peeling force as well as the displacement of the moving grip were recorded at a frequency of 5 Hz. The energy release rate (with an alternative interpretation as interlamellar toughness, i.e., the energy

required to split a unit area of the interface) can be calculated as (Sommer et al. 2008)

$$G_c = (W_{ext} - W_{elastic})/L \quad (2.2)$$

where G_c is the energy release rate. $W_{ext} = 2Fl$ is the total external work done by the peeling force, and $W_{elastic} = F(l - L)$ is the elastic energy stored within the stretched tissue. F is the mean peeling force per unit width of the sample. L and l are length of the sample strip in the initial and stretched states, respectively.

2.4 Direct tension test

Samples were first cut into approximately 2 cm × 2 cm square patches. Cylindrical samples with a diameter of 6.35 mm were cut from the square patches using a punching tool. Damage was initiated in the samples by making an incision of about 1 mm depth into the middle of the thickness around its circumference. Consequently, the diameter of the effective bonding area reduced to 4.35 mm. Direct tension tests were performed by mounting the two end surfaces of the sample on a uniaxial tensile tester (Instron, Norwood, MA, USA) and stretching the sample along its radial direction until complete separation (Sommer et al. 2008). Two rigid rods gripped by the tester were glued with sandpaper using cyanoacrylate glue. The end surfaces of the sample were then glued to the sandpaper by first attaching one side of the sample to the fixed rod and then bringing the other rod to the sample. A compressive force of 0.01 N was applied to the sample for about 5 minutes for the adhesion to set. To minimize the influence of glue on the measurement of mechanical failure properties, each sample was checked to ensure that there was no extra glue on the circumference or within the initial incision of the

sample, otherwise the sample was discarded. Before the testing started, the sample was moisturized with PBS spray at room temperature. The moving rod was then pulled away at an extension rate of 0.02 mm/s. The displacement of the moving rod as well as the reaction force was recorded at a frequency of 5 Hz. The deformation process of a sample was monitored carefully. The testing was rejected if damage did not propagate from the location where the initial incision was made, or separation occurred at the glued interface between the sandpaper and the tissue. The interlamellar strength was obtained by dividing the maximum reaction force prior to the damage onset point, which was marked by a rapid drop in the slope of the force-displacement curve after the initial increase of the reaction force, by the initial effective bonding area as

$$t_{DT} = \frac{F_0}{A} \tag{2.3}$$

where t_{DT} is the interlamellar strength measured from direct tension tests. F_0 is the maximum reaction force prior to the damage onset point. $A = 4d^2/\pi$ is the effective bonding area of the sample. $d = 4.35\ mm$ is the diameter of the effective bonding area.

2.5 Multiphoton microscopy

An inverted multiphoton microscopy system (Carl Zeiss LSM 710 NLO) was used to generate two-photon excited fluorescence (2PEF) from elastin (525/45 nm) and second harmonic generation from collagen (417/80 nm) (Chow et al. 2014; Yu et al. 2018a, b). The excitation wavelength of the femtosecond IR pulse laser was set to be 810 nm. The laser scanning system was coupled with a 20× water immersion objective lens. Samples were prepared following the same protocols for mechanical testing as described

in Sections 2.2, 2.3 and 2.4. Samples were then mounted on a custom-built device for multiphoton imaging. For imaging of peeling samples, the two “tongues” of the sample were gripped and stretched apart so that the dissection forefront was exposed under the lens. For imaging of direct tension samples, a stretch of about 2 mm was applied on the sample to expand the initial incision and straighten the interlamellar fibers; the lens was then placed above the incision. Z-Stack images of about 50 μm in depth with 1 μm distance in between the adjacent images were acquired. Each image has a field of view of 425 μm × 425 μm with a pixel size of 0.83 μm × 0.83 μm.

CHAPTER 3 EFFECT OF AGING ON THE BIAXIAL MECHANICAL BEHAVIOR OF HUMAN DESCENDING THORACIC AORTA: EXPERIMENTS AND CONSTITUTIVE MODELING CONSIDERING COLLAGEN CROSSLINKING

3.1 Overview

Collagen crosslinking, an important contributor to the stiffness of soft tissues, was found to increase with aging in the aortic wall. Here we investigated the mechanical properties of human descending thoracic aorta with aging and the role of collagen crosslinking through a combined experimental and modeling approach. A total of 32 samples from 17 donors were collected and divided into three age groups: <40, 40–60 and >60 years. Planar biaxial tensile tests were performed to characterize the anisotropic mechanical behavior of the aortic samples. A recently developed constitutive model incorporating collagen crosslinking into the two-fiber family model (Holzapfel and Ogden, 2020) was modified to accommodate biaxial deformation of the aorta, in which the extension and rotation kinematics of bonded fibers and crosslinks were decoupled. The mechanical testing results show that the aorta stiffens with aging with a more drastic change in the longitudinal direction, which results in altered aortic anisotropy. Our results demonstrate a good fitting capability of the constitutive model considering crosslinking for the biaxial aortic mechanics of all age groups. Furthermore, constitutive modeling results suggest an increased contribution of crosslinking and strain energy density to the biaxial stress-stretch behaviors with aging and point to excessive crosslinking as a prominent contributor to aortic stiffening.

3.2 Introduction

The aortic wall stiffens with age (Cecelja and Chowienczyk, 2012), which gives rise to an augmented systolic blood pressure with increased risks for the development of multiple co-morbid diseases such as hypertension, stroke and chronic kidney disease (Wang et al., 2005; North and Sinclair, 2012). The microstructural mechanisms that contribute to aging-induced aortic stiffening are diverse. Within the aortic extracellular matrix (ECM), crosslinking plays an important role in determining arterial stiffness. Two types of crosslinks were identified in aortic collagen: enzyme driven crosslinking (Fujimoto, 1982; Eyre et al., 1984; Reiser et al., 1992; Carmo et al., 2002), as well as nonenzymatic advanced glycation end-products (AGEs) (Wolff et al., 1991; Hoshino et al., 1995). The density of enzymatic crosslinking increases rapidly before maturation (Brüel and Oxlund 1996; Watanabe et al., 1996). However, controversial information exists regarding the post-maturation change of enzymatic crosslinking density, as a slightly increasing trend was found in some studies (Fujimoto, 1982; Watanabe et al., 1996), whereas other researchers reported a constant (Brüel and Oxlund 1996) or decreasing trend (Hoshino et al., 1995). Nevertheless, the density of nonenzymatic crosslinking increases with age throughout the lifespan (Hoshino et al., 1995; Sims et al., 1996; Snedeker and Gautieri, 2014), and was found to have a positive correlation with aortic stiffness (Brüel and Oxlund, 1996).

Crosslinks stiffen the collagen network primarily by restraining sliding between fibers and engaging more fibers to load-bearing (Depalle et al., 2015; Žagar et al., 2015). The network stiffness is dictated by the density rather than stiffness of crosslinks as

revealed by molecular and fiber level computational studies (Depalle et al., 2015; Lin and Gu, 2015; Chen et al., 2017). Besides aging, increased collagen crosslinking density has been found to accelerate with the progression of other diseases such as diabetes (Sims et al., 1996) and aneurysm (Carmo et al., 2002). Although excessive crosslinking is detrimental, it should be noted that a proper amount of enzymatic crosslinking in the ECM is necessary for a normal mechanical function of soft tissues by providing stiffness and strength necessary for maintaining the stability of the ECM (Brüel et al., 1998), facilitating stress transfer among neighboring fibers to make the tissue behave as a coherent network (Lindeman et al., 2010), as well as reducing energy loss during cyclic loading (Kim et al., 2017). In addition to collagen, crosslinks can form among other aortic ECM components including elastin and glycoproteins. Specifically, AGEs in aortic elastin increase with aging (Konova et al., 2004) while the two major enzymatic elastin crosslinks desmosine and isodesmosine decrease slightly (John and Thomas, 1972). Histidinoalanine, a crosslink between glycoproteins, and between glycoproteins and collagen and elastin, increases drastically with aging (Fujimoto, 1982).

While experimental characterization of the contribution of collagen crosslinks to arterial wall mechanics remains a challenge, in several efforts, modeling approaches have been used to incorporate collagen crosslinking at multiple length scales. Molecular dynamics models (Buehler, 2008; Depalle et al., 2015; Kwansa et al., 2016) and discrete fiber network models (Lin and Gu, 2015; Žagar et al., 2015; Chen et al., 2017; Yu and Zhang, 2022) were employed to elucidate the effect of crosslinking density, type and mechanical properties on the deformation and failure behavior of fibers and networks. At

the tissue level, statistical mechanics-based model was used to describe arterial mechanics where the crosslinking density is inversely related to chain length (Zhang et al., 2005, 2007; Tian et al., 2016). Several recent continuum mechanics-based models were developed in which the contribution of collagen crosslinking to tissue behavior was decoupled from the rest of the ECM. In a study by Sacks et al. (Sacks et al., 2016), the interaction between collagen fiber families induced by crosslinking was modeled by decoupling extensional and rotational effects. In Sáez et al. (Sáez et al., 2014), the strain energy density function was extended with an additional isotropic term to incorporate the mechanical contribution of crosslinking. Recently, a constitutive model considering the stretch of crosslinks and crosslink-fiber interaction was incorporated into a two-fiber family model (Holzapfel and Ogden, 2020). These studies reported better fitting and predicting capabilities of constitutive models considering the contribution of crosslinking.

Invariant I_8 was introduced by Spencer (1984) to model the coupling interactions between two families of fibers under finite deformation, and then adopted in several studies to model fiber-fiber and crosslink-fiber interactions (Merodio and Ogden, 2006; Holzapfel and Ogden, 2020). While most biomechanical investigations of human thoracic aorta were performed with uniaxial tensile tests (Manopoulos et al., 2018; Amabili et al., 2019; Amabili et al., 2021), for anisotropic soft tissues such as the aortic wall, biaxial tensile testing allows for adjusting the biaxial loading ratio in uniquely determining the parameters for three-dimensional constitutive models (Sacks, 2000). However, under biaxial deformation, extension and rotation kinematics could have opposite mathematical effects on the change of the magnitude of I_8 and thus diminish the contribution of

crosslink-fiber interaction to the strain energy density.

In this study, motivated by Holzapfel and Ogden (2020), collagen crosslinking was incorporated into a two-fiber family model to describe the biaxial mechanical behavior of the aorta. The extension and rotation kinematics of crosslinking was decoupled so that both mechanisms can independently contribute to biaxial deformation. Exponential functions were used in describing the crosslinking-associated strain energy density in nonlinear aortic stiffening. Also, changes of the mechanical properties of human descending thoracic aorta with aging was studied to provide new insights into the microstructural mechanisms of aortic stiffening through constitutive modeling. Biaxial tensile tests were performed on human descending thoracic aortas from 24 to 90 years old donors. The effect of aging on aortic stiffness and anisotropy as well as the mechanical role of crosslinking in the aging aorta was examined through a combined experimental and modeling approach.

3.2 Material and methods

3.2.1 Sample preparation

Human descending thoracic aortas were obtained from the National Disease Research Interchange (NDRI) and transported to laboratory on dry ice and stored at -80°C before experiment. The age, gender and selected medical information of aorta donors is summarized in Table 3.1. The use of human tissue was reviewed and approved by the Institutional Biosafety Committee at Boston University. Before experiments, aortas were defrosted at -20°C for 5 hours followed by 3 hours at 4°C and then 1 hour at

room temperature. Square samples free of visible atherosclerotic plaques with a dimension of approximately 2.5 × 2.5 cm were cut with the edges of the samples aligned with the longitudinal and circumferential directions of the aorta. Loose connective tissue was removed from the adventitial surface. Two samples were obtained from each aorta except for aortas N8 and N16 due to limited tissue size. All samples were obtained from the proximal region of the descending thoracic aorta to reduce longitudinal variation of the mechanical properties of aortic tissues (Purslow, 1983; Zou and Zhang, 2009; Rouleau et al., 2012; Kim et al., 2013; Zeinali-Davarani et al., 2015). Donors were divided into three age groups: <40 (n=8), 40-60 (n=11), and >60 (n=13) years.

3.2.2 Planar biaxial tensile testing

Refer to Section 2.2 for a detailed description of biaxial tensile testing. Samples were then subjected to the following five biaxial loading protocols: T_L: T_C=200:200, 200:150, 200:100, 100:200, and 150:200 N/m. Tangent modulus was obtained by taking the derivative of a fifth order polynomial fit to the Cauchy stress-stretch data. The peak stretch under 200:200 N/m equibiaxial tension were obtained in both circumferential and longitudinal directions and used to assess the degree of anisotropy (DA) as (Jadidi et al., 2020):

$$DA = \frac{\lambda_L - \lambda_C}{0.5(\lambda_C + \lambda_L)} \tag{3.1}$$

Table 3.1 Age, gender and selected medical information of human descending thoracic aorta donors used in this study. HTN - hypertension; HLP - hyperlipidemia; BMI - body mass index; F - female; M - male; Y - yes; N - no; * - during pregnancy; SIGSW - self-inflicted gunshot wound; MVA - motor vehicle accident; CPA - cardiopulmonary arrest; CVA - cerebrovascular accident; ABI - anoxic brain injury; HD - heart disease; COPD - chronic obstructive pulmonary disease.

Age group	Donor	Age (years)	Gender	HTN	HLP	BMI	Cause of death
<40 years	N1	24	F	Y*	N	30.27	SIGSW
	N2	26	M	N	N	26.5	MVA
	N3	32	M	N	N	64.83	CPA
	N4	39	F	N	N	24.69	CVA
40–60 years	N5	42	M	Y	N	44.3	CPA
	N6	44	F	Y	N	38.23	ABI
	N7	47	M	Y	N	47.47	CPA
	N8	49	M	Y	N	24.06	CVA
	N9	57	F	N	N	18.5	ABI
	N10	59	M	N	N	29.18	HD
>60 years	N11	62	F	Y	N	25.81	CVA
	N12	64	F	N	Y	38.6	CPA
	N13	70	M	Y	N	Unknown	CVA
	N14	72	F	N	N	72.45	CPA
	N15	74	F	N	N	14.98	COPD
	N16	87	M	Y	Y	29.53	CPA
	N17	90	F	Y	N	16.14	CPA

3.2.3 Constitutive model development

Two-fiber family model was chosen upon which the crosslinking mechanisms are based to represent the two prominent collagen fiber families found in the intima, media and adventitia in human thoracic aortas (Schriefl et al., 2012). In the newly developed constitutive model, deformation of collagen crosslinks and crosslink-fiber interaction

were incorporated into the two-fiber family model considering the kinematics of bonded fiber and crosslink under biaxial deformation. A schematic of the model, shown in Figure 3.1, contains two collagen fiber families with the angle between each collagen fiber family and the longitudinal direction denoted by θ. $\boldsymbol{E_1} = \{cos\theta, sin\theta, 0\}^T$ and $\boldsymbol{E_2} = \{cos\theta, -sin\theta, 0\}^T$ are unit vectors along the direction of the two collagen fibers. The crosslinks are symmetrically distributed within each collagen fiber family. As shown in Figure 3.1, the angle between the orientation of crosslinks and their associated collagen fibers is denoted by α_0. $\boldsymbol{L_{1,2}^+}$ and $\boldsymbol{L_{1,2}^-}$ are unit vectors in the direction of crosslinks, where subscripts 1 and 2 denote the family of collagen fibers that the crosslinks are attached to, and superscripts + and – are used to distinguish between the two crosslink families, and can be written as:

$$\boldsymbol{L_1^{\pm}} = \pm cos\alpha_0 \boldsymbol{E_1} + sin\alpha_0 \boldsymbol{E_{1R}}, \text{ and } \boldsymbol{L_2^{\pm}} = \pm cos\alpha_0 \boldsymbol{E_2} + sin\alpha_0 \boldsymbol{E_{2R}} \quad (3.2)$$

where $\boldsymbol{E_{1R}} = \{-sin\theta, cos\theta, 0\}^T$ and $\boldsymbol{E_{2R}} = \{-sin\theta, -cos\theta, 0\}^T$ are unit vectors normal to collagen fiber orientations (Figure 3.1).

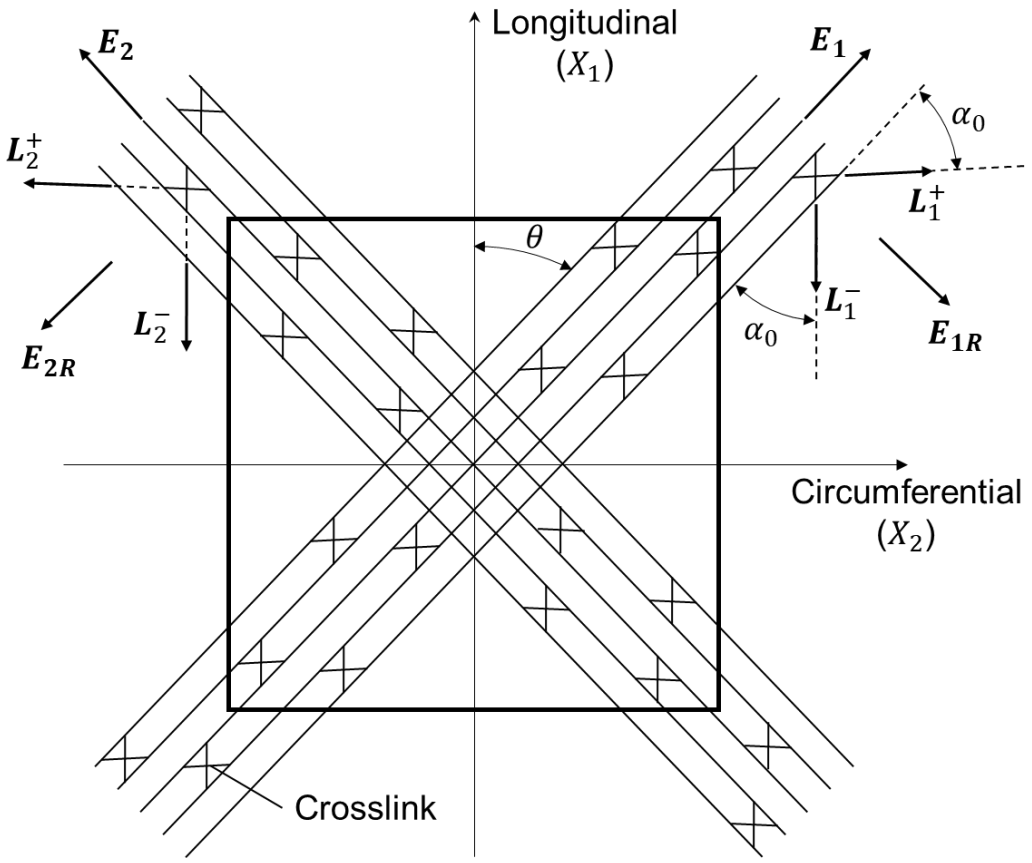

Figure 3.1 Schematic of a sample with two families of collagen fibers and crosslinks. $\boldsymbol{E_{1,2}}$ is the unit vector in the orientation of collagen fibers; $\boldsymbol{E_{1,2R}}$ is the unit vector normal to the orientation of collagen fibers; $\boldsymbol{L_{1,2}^{\pm}}$ is the unit vector in the orientation of crosslinks; $\boldsymbol{\theta}$ denotes the angle between the longitudinal direction of the aorta and the orientation of collagen fibers; and $\boldsymbol{\alpha_0}$ denotes the angle between the orientations of collagen fibers and their associated crosslinks.

With crosslinks bonded to collagen fibers, under mechanical loading, both collagen fibers and crosslinks are stretched, leading to relative rotation between the bonded fibers and crosslink. The bonded fiber and crosslink may mechanically interact by extension and relative rotation, both of which contribute to the increase of the strain energy density of the aortic wall under deformation (Sacks et al., 2016; Mansouri et al., 2021). Considering the kinematics of bonded fiber and crosslink under biaxial tension

(Appendix A), the extension and relative rotation of bonded fiber and crosslink was decoupled in this model. The strain energy density function of the aorta, W_{2FFC}, is thus given by:

$$W_{2FFC} = W_{2FF} + W_c + W_{cf} \tag{3.3}$$

where W_{2FF}, W_c and W_{cf} are strain energy density functions of the two-fiber family model (Holzapfel et al., 2000), deformation of collagen crosslinks, and crosslink-fiber interaction, respectively. The strain energy density function of the two-fiber family model is:

$$W_{2FF} = \frac{\mu}{2}(I_1 - 3) + \frac{k_1}{2k_2}\left\{exp\left[k_2\left(I_{4,1} - 1\right)^2\right] - 1\right\} + \frac{k_1}{2k_2}\left\{exp\left[k_2\left(I_{4,2} - 1\right)^2\right] - 1\right\} \tag{3.4}$$

where the first term represents the contribution of ground substance, smooth muscle cells, and elastin with μ being the shear modulus, and I_1 is the first invariant of the right Cauchy-Green deformation tensor $\boldsymbol{C}$. For the two collagen fiber families represented by the second and the third terms, k_1 is a stress-like parameter, and k_2 is a dimensionless parameter. $I_{4,1}$ and $I_{4,2}$ are square of collagen fiber stretch and can be obtained as $\boldsymbol{E_1} \cdot \boldsymbol{CE_1}$ and $\boldsymbol{E_2} \cdot \boldsymbol{CE_2}$, respectively.

The strain energy density function of crosslinking extension, W_c, is assumed to follow the same exponential form as that of collagen fibers to accommodate the reported increased nonlinearity of aortic stress-stretch behavior with aging (Geest et al., 2004; Jadidi et al., 2020):

$$W_c = \frac{\nu_1}{2\nu_2}\{exp[\nu_2(I_1^+ - 1)^2] - 1\} + \frac{\nu_1}{2\nu_2}\{exp[\nu_2(I_1^- - 1)^2] - 1\} + \frac{\nu_1}{2\nu_2}\{exp[\nu_2(I_2^+ - 1)^2] - 1\} + \frac{\nu_1}{2\nu_2}\{exp[\nu_2(I_2^- - 1)^2] - 1\} \tag{3.5}$$

where ν_1 is a stress-like parameter, and ν_2 is a dimensionless parameter. $I_{1,2}^{\pm} = \boldsymbol{L}_{\mathbf{1,2}}^{\pm} \cdot \boldsymbol{CL}_{\mathbf{1,2}}^{\pm}$ is the square of crosslink stretch.

To model the relative rotation between the bonded fiber and crosslink, a modified invariant, $I_{8*}^{1,2\pm}$, which decouples the extensional effects of bonded fiber and crosslink from its unmodified counterpart, and only incorporates the relative rotation between bonded fiber and crosslink in considering the crosslink-fiber interaction, is introduced as:

$$I_{8*}^{1,2\pm} = \frac{I_8^{1,2\pm}}{\sqrt{I_{4,1,2} I_{1,2}^{\pm}}} = cos\alpha^{\pm} \tag{3.6}$$

As shown in Equation 3.6, $I_{8*}^{1,2\pm}$ is equal to the cosine of the angle between bonded fiber and crosslink in the deformed configuration. α^{+} and α^{-} are the angles between collagen fiber orientated in $\boldsymbol{E}_{\mathbf{1,2}}$ and associated crosslinks oriented in $\boldsymbol{L}_{\mathbf{1,2}}^{+}$ and $\boldsymbol{L}_{\mathbf{1,2}}^{-}$ directions in the deformed configuration**,** respectively. The invariant $I_8^{1,2\pm}$ couples the extension and relative rotation of bonded fiber and crosslink under deformation and is defined as (Merodio and Ogden, 2006; Holzapfel and Ogden, 2020):

$$I_8^{1,2\pm} = \boldsymbol{L}_{\mathbf{1,2}}^{\pm} \cdot \boldsymbol{CE}_{\mathbf{1,2}} \tag{3.7}$$

The strain energy density function of the crosslink-fiber interaction, W_{cf}, captures the relative rotation between the bonded fiber and crosslink and follows the same exponential form as those of fiber and crosslink extension:

$$W_{cf} = \frac{\kappa_1}{2\kappa_2}\{exp[\kappa_2(I_{8*}^{1+} - cos\alpha_0)^2] - 1\} + \frac{\kappa_1}{2\kappa_2}\{exp[\kappa_2(I_{8*}^{1-} + cos\alpha_0)^2] - 1\} +$$

$$\frac{\kappa_1}{2\kappa_2}\{exp[\kappa_2(I_{8*}^{2+} - cos\alpha_0)^2] - 1\} + \frac{\kappa_1}{2\kappa_2}\{exp[\kappa_2(I_{8*}^{2-} + cos\alpha_0)^2] - 1\} \tag{3.8}$$

where κ_1 is a stress-like parameter, and κ_2 is a dimensionless parameter.

For comparison purpose, the two-fiber family model without the consideration of collagen crosslinking is also adopted to describe the aortic biaxial mechanical response. The Cauchy stress tensor, $\boldsymbol{\sigma}$, can be calculated as:

$$\boldsymbol{\sigma}_{2FFC,2FF} = -p\boldsymbol{I} + 2\boldsymbol{F}\frac{\partial W_{2FFC,2FF}}{\partial \boldsymbol{C}}\boldsymbol{F}^T \tag{3.9}$$

where $\boldsymbol{I}$ is the identity tensor and $p = \mu/\left(\lambda_L{}^2\lambda_C{}^2\right)$ is the Lagrange multiplier.

3.2.4 Parameter estimation

The constitutive models were implemented in MATLAB (Version R2019a, The MathWorks, Inc., Natick, MA) and fit to the experimental Cauchy stress-stretch data considering all five loading protocols simultaneously for each sample. Model parameters μ, k_1, k_2, ν_1, ν_2, κ_1 and κ_2 were set to be greater than zero, θ and α_0 varied between 0 and 90°. Parameters were estimated by minimizing the following objective function:

$$\psi = \sum_{i=1}^{m/2}\left[(\sigma_L^c - \sigma_L^e)_i{}^2 + (\sigma_C^c - \sigma_C^e)_i{}^2\right] \tag{3.10}$$

where m is the total number of data points. Superscripts c and e denote Cauchy stresses from the model and experiment, respectively. The *fminsearch* function with embedded Nelder-Mead direct search method was used to minimize the objective function with a tolerance of 1×10^{-8}. To ensure that the global minimum of the objective function is reached, and to enhance the reliability and robustness of the estimated parameters, the model was fit to five biaxial tensile loading protocols (T_L: T_C=200:200, 200:150, 200:100, 100:200, and 150:200 N/m) simultaneously. Also, the nonlinear regression with *fminsearch* was carried out with multiple random initial guesses. The estimation was

accepted only when different initial guesses converge to the same set of parameters. The goodness of fit was measured by the coefficient of determination (R^2) as well as the root mean square error (RMSE) defined as (Holzapfel et al., 2005):

$$\mathrm{RMSE} = \frac{\sqrt{\frac{\psi}{m-q}}}{\sigma_{ref}} \tag{3.11}$$

where q is the number of parameters of the constitutive model, and σ_{ref} is the sum of Cauchy stresses of each data point divided by the number of data points m. Additionally, to account for the different numbers of parameters in the two constitutive models, the corrected Akaike information criterion ($\mathrm{AIC_C}$) which penalizes the goodness of fit for increasing number of model parameters was also used and is defined as (Zeinali-Davarani et al., 2009; Ferruzzi et al., 2011):

$$\mathrm{AIC_C} = m\ln\left(\frac{\psi}{m}\right) + 2(q+1) + \frac{2(q+1)(q+2)}{m-q-2} \tag{3.12}$$

A better fit corresponds to a lower $\mathrm{AIC_C}$. Further, contributions of the strain energy density due to crosslink deformation (W_c) and crosslink-fiber interaction (W_{cf}) to the total strain energy density (W) of all samples under 200 N/m equibiaxial tension were obtained as W_c/W and W_{cf}/W, respectively, which were then compared across age groups to provide a better understanding of the contribution of collagen crosslinking to the mechanical behavior of human descending thoracic aorta with aging.

3.2.5 Statistical analysis

Data are summarized using box plots and are also presented as mean ± standard error of the mean (SEM). Data normality of the peak stretch, tangent modulus, degree of anisotropy, R^2, RMSE, AIC_C, W_c/W and W_{cf}/W was examined with the Kolmogorov-Smirnov and the Shapiro-Wilk tests. Within each age group, paired t-test was used to compare the peak stretch and tangent modulus between the circumferential and longitudinal directions, and R^2, RMSE and AIC_C of the stress-stretch fittings with constitutive models with and without crosslinking. Across the three age groups, one-way analysis of variance (ANOVA) was used with Bonferroni correction for the peak stretch, tangent modulus, degree of anisotropy, R^2, RMSE, W_c/W and W_{cf}/W. AIC_C was used to compare the goodness of fit of a constitutive model for samples of matching age groups. Correlation analysis of age relevant to W_c/W and W_{cf}/W, as well as mechanically or structurally meaningful model parameters μ, θ and α_0, is performed. For statistical analysis involving data that are not normally distributed, the Wilcoxon signed-rank test and the Kruskal-Wallis H test were used as nonparametric counterparts of the paired t-test and one-way ANOVA. All statistical analysis was performed in SPSS (Version 27, IBM Corp., Armonk, NY). $p<0.05$ was considered statistically significant.

3.3 Results

The Cauchy stress-stretch curves of all samples under 200 N/m equibiaxial tension are shown in Figure 3.2. With aging, the stiffness in both longitudinal and circumferential directions increases as the Cauchy stress-stretch curves become steeper

and gradually shift towards left. The increase of stiffness with aging is also supported by the decreasing peak stretch (Figure 3.3a) and increasing tangent modulus (Figure 3.3b) in both directions. The longitudinal and circumferential peak stretches decrease from 1.31 ± 0.03 and 1.29 ± 0.02 for the <40 age group to 1.21 ± 0.01 and 1.26 ± 0.01 for the 40-60 age group and then to 1.10 ± 0.01 and 1.16 ± 0.02 for the >60 age group, respectively. The longitudinal tangent modulus increases from 2.08 ± 0.17 MPa to 3.31 ± 0.48 MPa and then to 5.48 ± 0.49 MPa for the <40, 40-60 and >60 age groups, respectively; while the circumferential tangent modulus was found to be 1.80 ± 0.19 MPa and 1.80 ± 0.20 MPa for the <40 and 40-60 years groups, respectively, and increases to 3.11 ± 0.30 MPa for the >60 age group. A more prominent stiffening effect was found in the >60 age group for both circumferential and longitudinal directions ($p<0.05$), as no significant difference of the peak stretch and tangent modulus was found between the <40 and 40-60 years age groups. However, aortic stiffening with aging is more drastic in the longitudinal than in the circumferential direction (Figure 3.3), as from the <40 to 40-60 age groups the mean longitudinal peak stretch decreases by 7.63% while the mean circumferential peak stretch decreases by only 2.33%, and from 40–60 to >60 age groups the mean longitudinal peak stretch decreases by 9.09% ($p<0.05$) while the mean circumferential peak stretch decreases by 7.94% ($p<0.05$). Similarly, from the <40 age group to the >60 age group, the mean longitudinal tangent modulus increases by 163.46% ($p<0.05$) while the mean circumferential tangent modulus increases by 72.78% ($p<0.05$). Aging also alters the degree of anisotropy as the in-plane stiffness is higher in the circumferential direction than the longitudinal direction in the <40 years age group; while as the age

further increases, the longitudinal direction exhibits a significantly higher stiffness than the circumferential direction for both 40-60 and >60 age groups ($p<0.05$), as shown in Figure 3.3. The change of the degree of anisotropy with aging is given in Figure 3.4, where a positive value of DA corresponds to a higher circumferential stiffness and a negative value of DA corresponds to a higher longitudinal stiffness. The degree of anisotropy decreases from 0.019 ± 0.026 to -0.042 ± 0.013 and then to -0.052 ± 0.018 for the <40, 40-60 and >60 age groups, respectively, with significant difference between the <40 and >60 age groups ($p<0.05$).

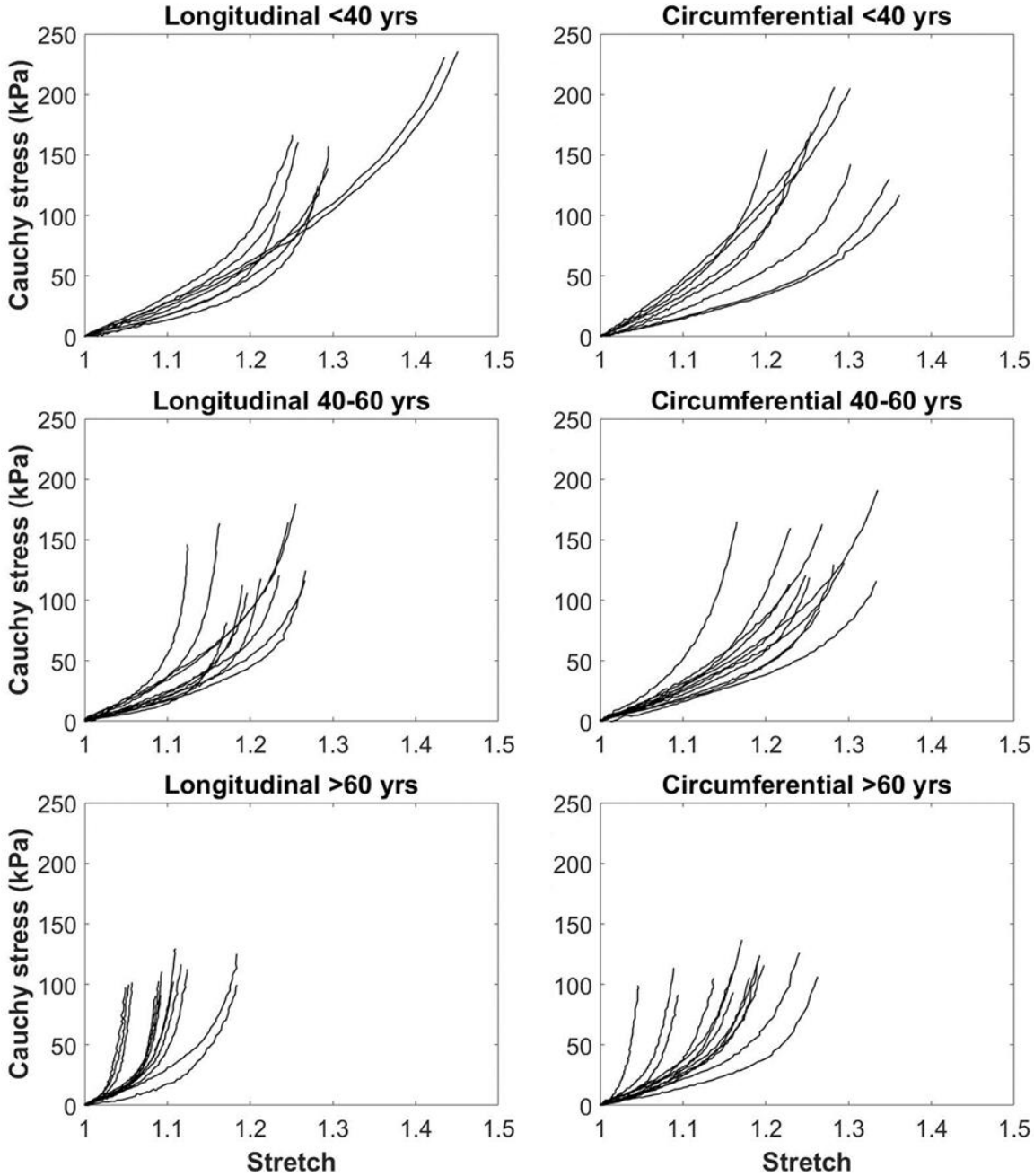

Figure 3.2 Cauchy stress-stretch curves in the circumferential and longitudinal directions of human descending thoracic aortas under 200 N/m equibiaxial tension test from the <40 yrs (years), 40-60 yrs, and >60 yrs age groups.

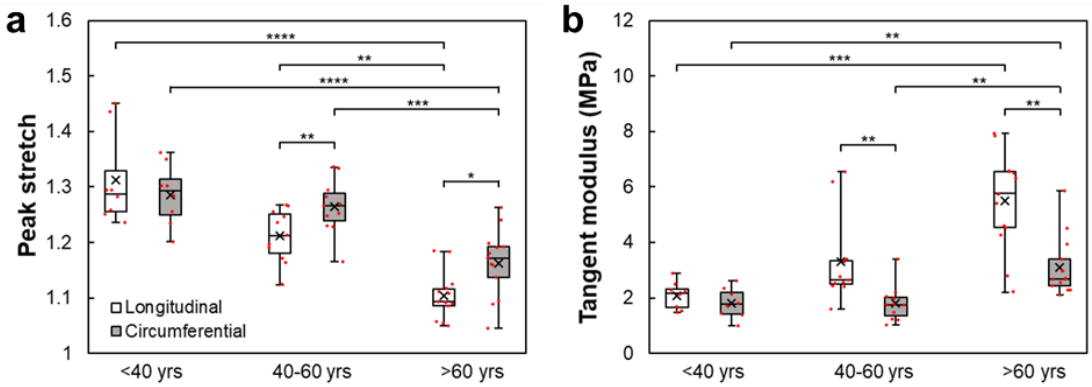

Figure 3.3 Effect of aging on a peak stretch and b tangent modulus of human descending thoracic aortas under 200 N/m equibiaxial tensile test. Boxes in the plots represent the middle 50% (from the first quartile to the third quartile) of the data set; the horizontal line inside the box represents the median; the cross symbol represents the mean; and the dotted symbols represent individual data points. (*p<0.05, **p<0.01, ***p<0.001, ****p<0.0001)

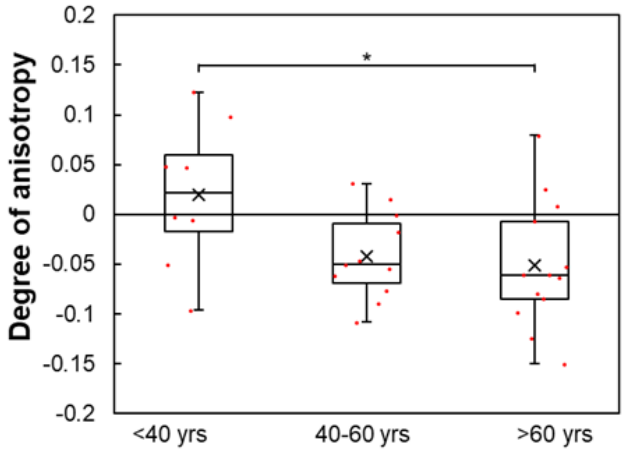

Figure 3.4 Effect of aging on the degree of anisotropy (DA) of human descending thoracic aortas under 200 N/m equibiaxial tensile test. The absolute value of DA increases suggesting a more anisotropic behavior of the sample. A positive DA corresponds to a higher circumferential stiffness while a negative DA corresponds to a higher longitudinal stiffness. Boxes in the plot represent the middle 50% (from the first quartile to the third quartile) of the data set; the horizontal line inside the box represents the median; the cross symbol represents the mean; and the dotted symbols represent individual data points. (*p<0.05)

Representative model fitting results of the experimental Cauchy stress-stretch curves with the two constitutive models with and without the consideration of collagen crosslinking are shown in Figures 3.5 and 3.6. Parameters as well as the associated R^2, RMSE and AIC_C of each sample are listed in Tables 3.2 and 3.3. The correlation coefficients and p-values of the correlation analysis of μ, θ, α_0 with age are shown in Table 3.4. Collagen orientation, θ, shows a strong negative correlation with age while the other two parameters do not. Compared to the model with crosslinking, the model without crosslinking is less capable of capturing the mechanical response at high stretch and exhibits relatively large fitting error for protocols with highly unequal biaxial tensile loads, i.e., when T_L: T_C=200:100 and 100:200 N/m, as shown in Figure 3.5. The fitting capacity of the constitutive model without crosslinking decreases with aging, as the RMSE increases from 0.18 ± 0.01 to 0.20 ± 0.01 and then to 0.27 ± 0.01 for the <40, 40-60 and >60 years age groups, respectively; and R^2 decreases from 0.96 ± 0.002 to 0.95 ± 0.005 and then to 0.92 ± 0.005 for the <40, 40–60 and >60 years age groups, respectively. Significant difference was found between the <40 and >60 as well as between the 40-60 and >60 years age groups for both R^2 and RMSE ($p<0.05$). On the contrary, the model with crosslinking shows improved goodness of fit (Figure 3.6), and the improved fitting capacity leads to significantly lower RMSE ($p<0.05$) and AIC_C ($p<0.05$) as well as higher R^2 ($p<0.05$) for all age groups than the model without crosslinking (Figure 3.7). The RMSE considering crosslinking was found to be 0.07 ± 0.01, 0.06 ± 0.01 and 0.09 ± 0.01 for the <40, 40-60 and >60 years age groups, respectively; and R^2 considering crosslinking was found to be 0.99 ± 0.002, 0.99 ± 0.001

and 0.99 ± 0.002 for the <40, 40-60 and >60 years age groups, respectively. In addition, without crosslinking, the AIC_C was found to be 3087.1 ± 131.6, 3002.0 ± 114.4 and 3126.8 ± 72.8 for the <40, 40-60 and >60 years age groups, respectively, which was reduced to 1446.3 ± 229.4, 1086.5 ± 192.0 and 1361.5 ± 186.7 after the effects of collagen crosslinking are incorporated into the constitutive model. The goodness of fit of the model with crosslinking is not affected by aging as no significant difference was found in either RMSE (p=0.07) or R^2 (p=0.21) across the three age groups (Figure 3.7). Compared with the <40 and 40-60 years groups, contributions of crosslinking-related strain energy density to the total strain energy density of samples under 200 N/m equibiaxial tension increased significantly in the >60 years age group ($p<0.05$). The ratio of the strain energy density due to crosslink deformation to the total strain energy density, W_c/W, was found to be 34.90% ± 6.32%, 30.06% ± 2.94% and 58.98% ± 6.12% for the <40, 40-60 and >60 years age groups, respectively. The ratio of the strain energy density due to crosslink-fiber interaction to the total strain energy density, W_{cf}/W, was found to be 0.10% ± 0.05% for the <40 years group, which increased slightly to 0.17% ± 0.07% and drastically to 2.34% ± 0.72% for the 40-60 and >60 years groups, respectively, as shown in Figure 3.8. Correlation analysis also demonstrates that both W_c/W and W_{cf}/W are positively correlated with age ($p<0.05$), as shown in Table 3.4.

Table 3.2 Model parameters of the two-fiber family model without considering the effect of crosslinking, and the associated root mean square error (RMSE), coefficient of determination ($\boldsymbol{R^2}$), and corrected Akaike information criterion (AIC_C) as measures of the goodness of fit. Two samples were obtained from each aorta except for N8 and N16. In the column of "Sample", numbers 1 and 2 in the parentheses denote the first and second sample obtained from the corresponding aorta.

	Constitutive model parameters				Goodness of fit		
Sample	μ (kPa)	k_1 (kPa)	k_2	θ (°)	RMSE	R^2	AIC_C
N1(1)	40.98	31.83	0.67	49.53	0.173	0.967	3590.0
N1(2)	38.77	32.96	0.56	48.47	0.166	0.969	3524.5
N2(1)	57.96	8.78	5.32	46.70	0.154	0.971	3020.3
N2(2)	34.31	12.72	2.58	45.29	0.192	0.956	3116.7
N3(1)	54.20	8.42	7.08	51.72	0.188	0.958	3158.7
N3(2)	39.26	11.41	4.23	48.49	0.191	0.957	3103.7
N4(1)	24.17	6.83	3.17	44.44	0.180	0.964	2482.6
N4(2)	21.53	7.52	3.05	44.80	0.199	0.959	2700.2
N5(1)	39.70	9.15	4.91	46.91	0.161	0.968	2482.9
N5(2)	38.04	5.12	5.62	41.80	0.167	0.965	2630.7
N6(1)	46.24	19.84	2.57	46.46	0.194	0.959	3229.1
N6(2)	48.21	14.61	2.92	43.60	0.158	0.975	3038.0
N7(1)	26.93	15.63	2.96	46.94	0.235	0.931	3144.0
N7(2)	40.63	10.41	3.84	43.86	0.175	0.964	2872.6
N8	26.19	6.51	7.88	42.56	0.253	0.926	2756.6
N9(1)	59.08	19.24	15.23	46.95	0.242	0.940	3656.1
N9(2)	45.78	28.95	10.34	41.86	0.262	0.937	3611.8
N10(1)	30.57	8.94	7.61	44.10	0.210	0.950	2822.6
N10(2)	34.01	4.04	8.16	43.23	0.196	0.959	2778.0
N11(1)	56.18	6.23	42.27	39.20	0.251	0.930	2801.9
N11(2)	32.17	6.93	22.32	37.55	0.256	0.933	2873.1
N12(1)	49.64	4.64	55.94	35.90	0.323	0.904	3246.3
N12(2)	28.26	10.15	28.76	48.80	0.249	0.939	2795.4
N13(1)	64.94	4.92	40.19	36.75	0.268	0.928	3224.7
N13(2)	43.51	5.93	18.52	39.43	0.215	0.953	2876.3
N14(1)	63.02	14.01	50.08	42.01	0.309	0.893	3377.4
N14(2)	35.93	10.29	11.53	44.05	0.216	0.949	2892.4
N15(1)	67.47	6.75	32.87	40.06	0.295	0.910	3579.4
N15(2)	65.29	8.64	57.27	34.48	0.307	0.909	3333.1
N16	40.99	10.75	25.32	40.68	0.265	0.928	3000.0
N17(1)	74.73	7.66	112.84	35.08	0.319	0.901	3309.7
N17(2)	109.32	31.39	237.41	48.16	0.298	0.908	3338.5

Table 3.3 Model parameters of the two-fiber family model considering the effect of crosslinking, and the associated root mean square error (RMSE), coefficient of determination ($\boldsymbol{R^2}$), and corrected Akaike information criterion (AIC_C) as measures of the goodness of fit. Two samples were obtained from each aorta except for N8 and N16. In the column of "Sample", numbers 1 and 2 in the parentheses denote the first and second sample obtained from the corresponding aorta.

	Constitutive model parameters						
Sample	μ (kPa)	k_1 (kPa)	k_2	θ (°)	ν_1 (kPa)	ν_2	κ_1 (kPa)
N1(1)	18.97	22.95	2.50E-11	54.78	12.95	0.44	9.36E-09
N1(2)	23.93	33.59	4.87E-11	61.18	5.32	0.77	8.66
N2(1)	41.73	3.32	2.62E-12	43.20	8.19	3.59	11.64
N2(2)	29.48	5.19E-06	26.18	44.53	6.94	2.40	6473.79
N3(1)	34.20	23.28	3.80	51.38	2.10E-04	15.23	39.83
N3(2)	30.66	12.17	3.31	59.38	2.03	3.43	6.87
N4(1)	13.84	4.15	3.81	39.26	5.19	0.48	2.03E-04
N4(2)	13.73	1.70	5.37	36.02	5.69	0.81	5.34E-13
N5(1)	31.43	12.80	2.33	56.65	1.22	5.94	4.91
N5(2)	35.25	0.44	11.18	33.96	2.83	4.23	1598.61
N6(1)	29.85	12.52	0.37	85.57	8.77	2.81	0.23
N6(2)	34.91	3.81	0.32	77.93	9.00	2.56	21.88
N7(1)	16.79	24.82	2.60E-13	54.82	0.52	9.50	8.92
N7(2)	29.07	11.07	7.81E-10	54.07	3.48	4.72	8.95
N8	12.19	10.61	0.02	70.31	2.57	11.05	9.87
N9(1)	4.19E-11	68.21	0.88	46.57	3.64	20.72	56998.71
N9(2)	33.98	15.35	12.91	37.01	5.73	10.06	7.78E-09
N10(1)	28.31	5.62	4.64	60.72	1.22	13.21	6.67
N10(2)	24.36	9.47	0.28	54.07	0.96	10.75	6.56
N11(1)	45.17	1.03	74.96	7.45	4.03	33.20	84.37
N11(2)	27.20	3.65	44.92	19.05	2.69	17.31	60.51
N12(1)	17.76	0.39	98.67	6.79E-08	10.73	28.16	252.29
N12(2)	1.14E-09	2.93	2.94	10.30	14.63	18.84	71.70
N13(1)	49.59	1.19	71.46	24.59	4.60	20.95	504.41
N13(2)	30.14	0.65	27.59	6.83	5.85	13.34	96.93
N14(1)	3.90E-14	0.98	51.46	10.97	33.77	20.53	4.74E-06
N14(2)	32.79	2.84	8.00	11.41	3.51	12.67	43.07
N15(1)	9.83	4.75	46.48	22.53	23.94	3.89	1.60E-12
N15(2)	31.18	6.96	121.88	18.00	12.38	17.44	256.07
N16	13.73	1.95	48.38	8.20	13.96	12.96	105.05
N17(1)	15.44	16.36	110.84	24.93	22.46	26.81	1509.29
N17(2)	9.02E-09	15.00	68.95	10.86	48.04	144.34	51.08

	Constitutive model parameters		Goodness of fit		
Sample	κ_2	α_0 (°)	RMSE	R^2	AIC_C
N1(1)	7025.75	28.12	0.032	0.999	1061.3
N1(2)	5.13E-14	90.00	0.026	0.999	715.5
N2(1)	21.15	82.16	0.073	0.993	1895.7
N2(2)	3.07E-09	17.98	0.049	0.997	1036.5
N3(1)	15.35	58.24	0.130	0.979	2599.2
N3(2)	7.52E-08	78.47	0.085	0.991	1879.2
N4(1)	1221.35	44.42	0.096	0.989	1543.2
N4(2)	6.33E-03	57.87	0.057	0.997	839.7
N5(1)	21.42	90.00	0.043	0.998	511.5
N5(2)	2117.17	18.87	0.057	0.996	995.7
N6(1)	1133.84	54.97	0.080	0.993	1885.7
N6(2)	103.98	51.36	0.029	0.999	471.0
N7(1)	5.23E-10	72.48	0.069	0.994	1286.9
N7(2)	6.03E-06	73.55	0.038	0.998	539.3
N8	133.33	69.87	0.088	0.991	1164.2
N9(1)	81231.28	15.27	0.089	0.992	2135.5
N9(2)	0.27	21.41	0.083	0.993	1866.3
N10(1)	5.01E-07	84.31	0.053	0.997	724.5
N10(2)	52.09	78.59	0.041	0.998	371.3
N11(1)	313.89	41.70	0.068	0.995	819.2
N11(2)	404.88	28.82	0.042	0.998	85.5
N12(1)	337.07	39.69	0.167	0.972	2244.5
N12(2)	168.76	54.88	0.077	0.994	1006.3
N13(1)	2.96E-09	27.17	0.070	0.995	1173.1
N13(2)	162.75	38.94	0.055	0.997	801.4
N14(1)	0.13	48.58	0.155	0.972	2348.1
N14(2)	1.42E-10	48.90	0.058	0.996	916.0
N15(1)	0.83	54.12	0.103	0.988	1988.2
N15(2)	3.06E-12	33.30	0.092	0.991	1506.0
N16	182.50	43.01	0.074	0.994	1065.7
N17(1)	3.72E-11	26.07	0.138	0.979	2053.2
N17(2)	5.62E-09	51.18	0.101	0.988	1692.2

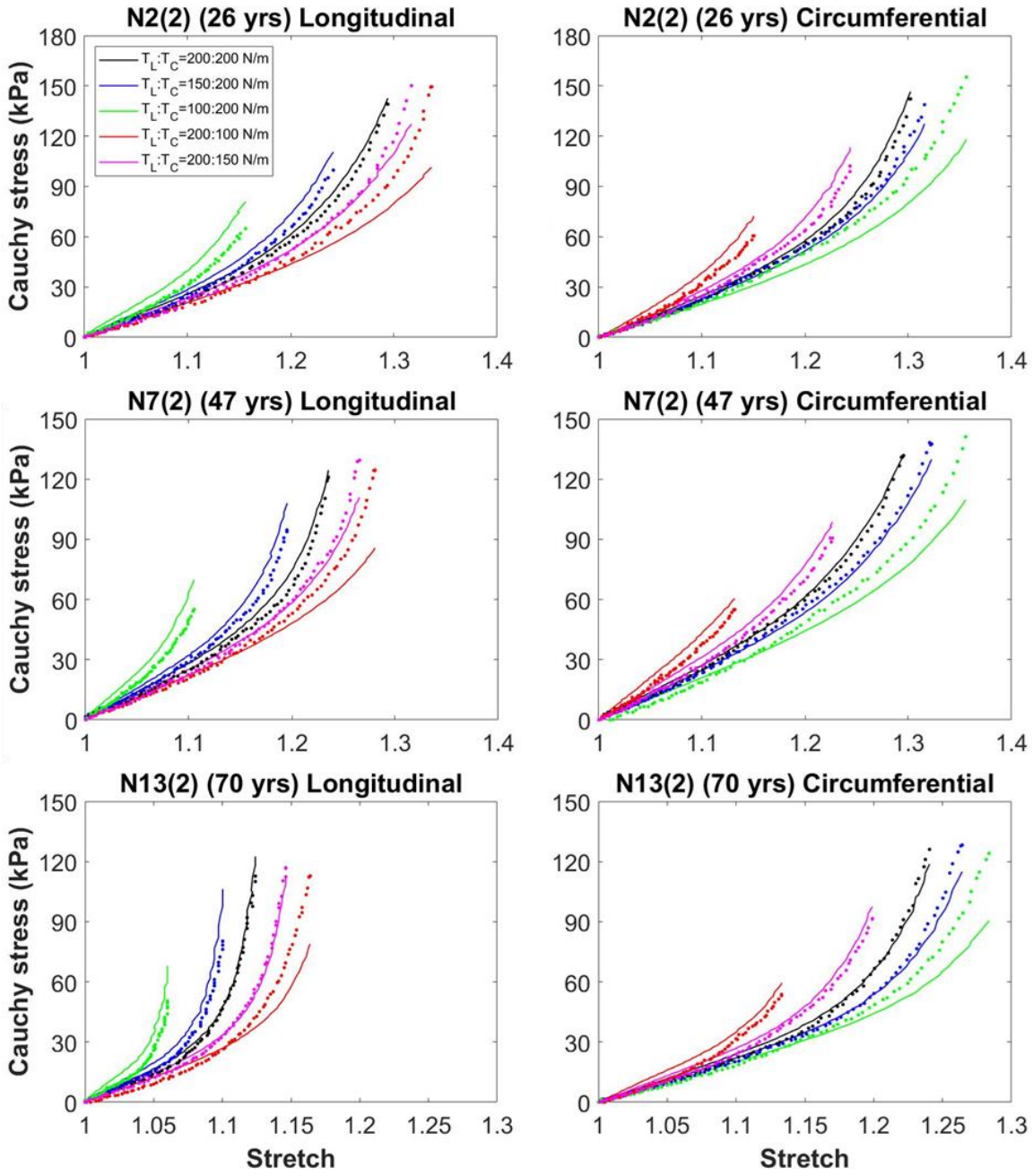

Figure 3.5 Representative curve fitting results of the two-fiber family model without considering the effect of crosslinking. Symbols represent experimental data and curves represent constitutive model fitting.

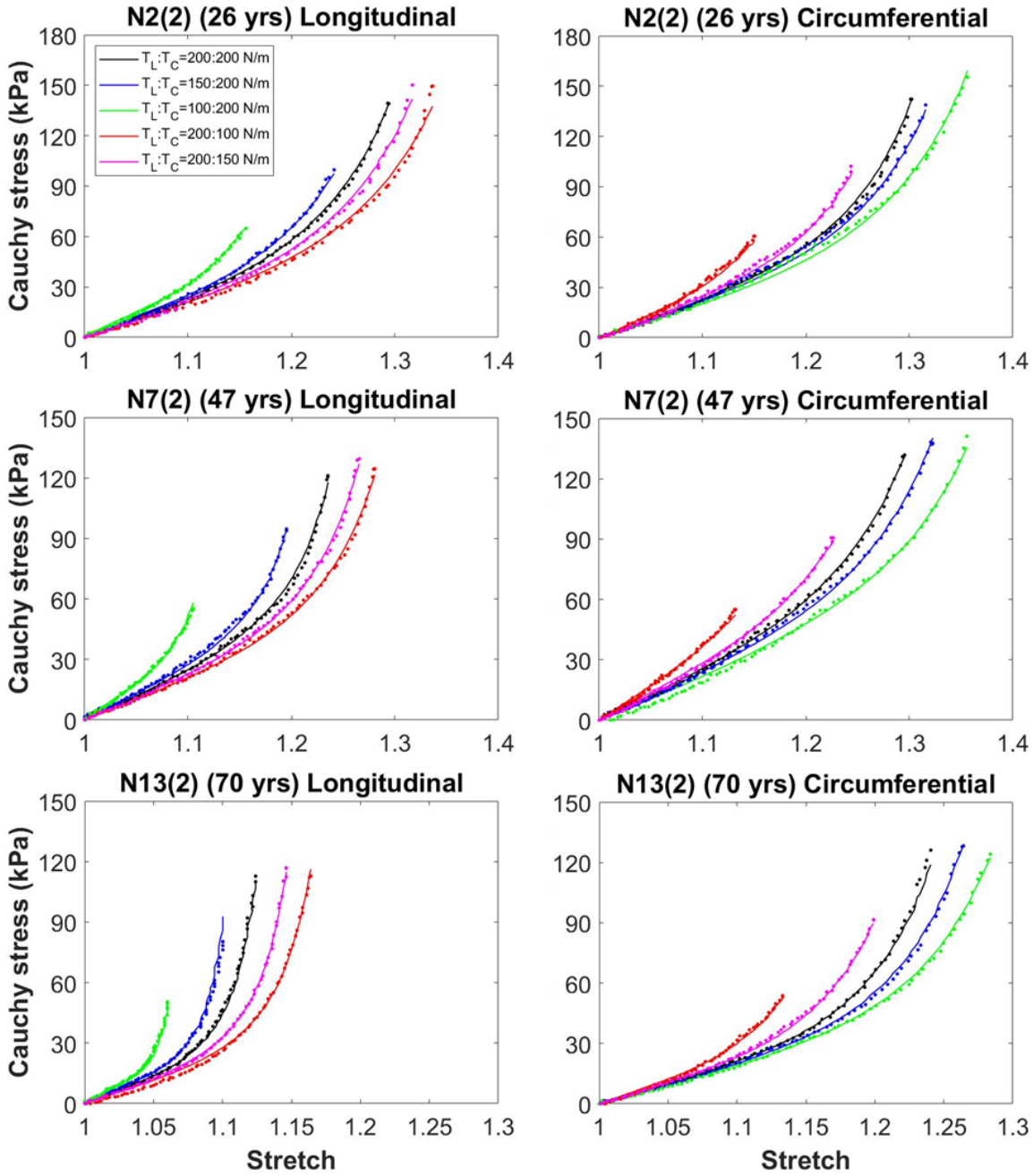

Figure 3.6 Representative curve fitting results of the two-fiber family model considering the effect of crosslinking. Symbols represent experimental data and curves represent constitutive model fitting.

3.4 Discussion

Aortic stiffening is a significant contributor and predictor of the progression of various diseases (Dernellis and Panaretou, 2005; O'Rourke and Safar, 2005; Wang et al., 2005; Riambau et al., 2017). Computational modeling of aging effects on aortic stiffening coupled with microstructural characteristics will greatly benefit our understanding of the mechanisms underlying aortic aging and pathologies, and lead to more reliable metrics for aortic function assessment and prediction. This study shows that human descending thoracic aorta stiffens with aging with a faster increase of stiffness in the longitudinal direction than the circumferential direction along with a reversed degree of anisotropy. Constitutive model considering the deformation of collagen crosslinks and crosslink-fiber interaction provides improved fitting capacity to the biaxial tensile behavior as compared to the two-fiber family model. It is found that collagen crosslinking has an increasing contribution to the stress-stretch behavior and strain energy density in human aorta senescence.

Table 3.4 Correlation coefficients and p-values of the correlation between age and model parameters as well as crosslinking-related strain energy contributions. $\boldsymbol{\mu}$ - shear modulus of the non-collagenous components, $\boldsymbol{\theta}$ - the angle between collagen fiber orientation and the longitudinal direction of the aorta, $\boldsymbol{\alpha_0}$ - angle between orientations of bonded crosslink and fiber, $\boldsymbol{W_c}$ - strain energy density of crosslink stretch, $\boldsymbol{W_{cf}}$ - strain energy density of crosslink-fiber interaction, $\boldsymbol{W}$ - total strain energy density.

	μ	θ	α_0	W_c/W	W_{cf}/W
Correlation coefficient	-0.308	-0.678	-0.305	0.523	0.512
p-value	0.086	2.0E-5	0.089	0.002	0.003

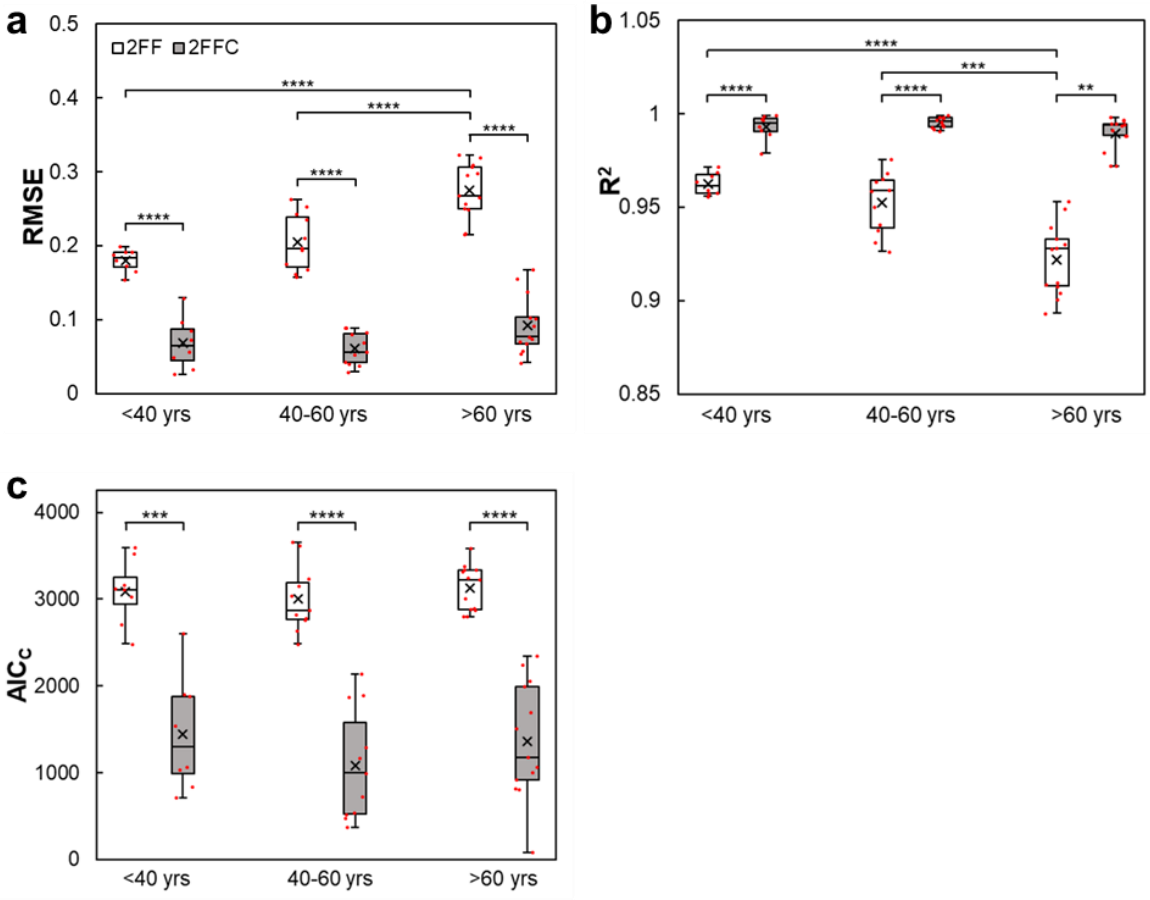

Figure 3.7 Comparison of a root mean square error (RMSE), b coefficient of determination ($\boldsymbol{R^2}$) and c corrected Akaike information criterion (AIC_C) as measurements of the goodness of fit for the two-fiber family model (2FF) and the two-fiber family with crosslinking model (2FFC). Boxes in the plots represent the middle 50% (from the first quartile to the third quartile) of the data set; the horizontal line inside the box represents the median; the cross symbol represents the mean; and the dotted symbols represent individual data points. (**p<0.01, ***p<0.001, ****p<0.0001)

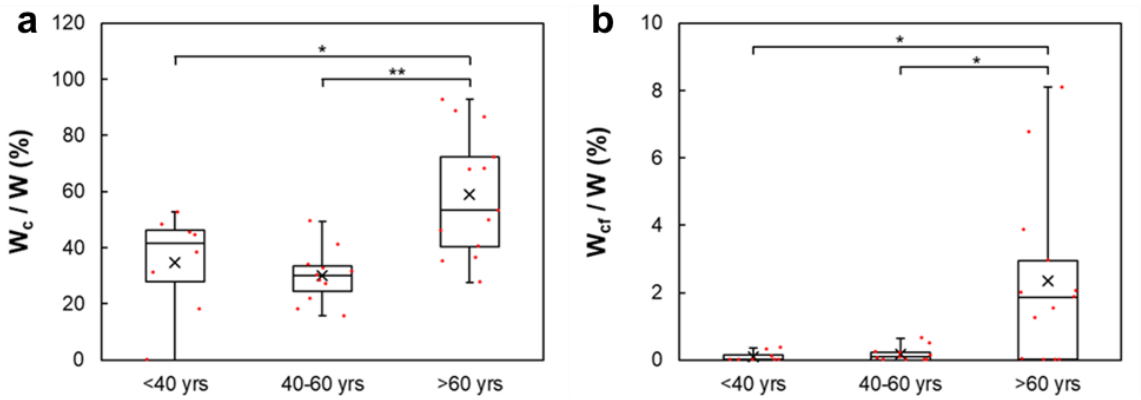

Figure 3.8 Contributions of the strain energy density due to a crosslink deformation ($\boldsymbol{W_c}$) and b crosslink-fiber interaction ($\boldsymbol{W_{cf}}$) to the total strain energy density ($\boldsymbol{W}$) of human descending thoracic aorta samples under 200 N/m equibiaxial tensile test. Boxes in the plots represent the middle 50% (from the first quartile to the third quartile) of the data set; the horizontal line inside the box represents the median; the cross symbol represents the mean; and the dotted symbols represent individual data points. (*p<0.05, **p<0.01)

Our results demonstrate an increasing stiffness of aging human descending thoracic aorta (Figures 3.2 and 3.3), which is consistent with earlier biomechanics studies (Langewouters et al., 1984; Sherebrin et al., 1989; Haskett et al., 2010; García-Herrera et al., 2012; Weisbecker et al., 2012; Amabili et al., 2019; Jadidi et al., 2020; Amabili et al., 2021; Franchini et al., 2021). The compromised mechanical functionality with aging dovetails with the reported increase in collagen concentration (Spina et al., 1983; Cattell et al., 1996; Wheeler et al., 2015; Cavinato et al., 2021), while the concentration of elastin decreases (Spina et al., 1983; Andreotti et al., 1985; Seyedsalehi et al., 2015). Meanwhile, similar as previously reported (Haskett et al., 2010; García-Herrera et al., 2012; Jadidi et al., 2020), our study shows faster longitudinal stiffening and reversed anisotropy (Figure 3.4). Interestingly, correlation analysis shows θ decreases significantly with age (Table 3.4), suggesting a shift of collagen fibers towards the

longitudinal direction, which explains the faster longitudinal stiffening. Furthermore, the prominent decrease of elastin mass fraction reported by Seyedsalehi et al. (Seyedsalehi et al., 2015) could largely change its interaction with collagen and the overall wall behavior. Also, elastin degradation may be direction-dependent and may play a role in preferentially promoting collagen recruitment in the descending thoracic aortic media. A recent study found that matrix metalloproteinase-12 (MMP12) preferentially stiffens the longitudinal direction of aging artery in mouse (Brankovic et al., 2019). As two closely interwoven ECM components (Wolinsky and Glagov, 1964; Chow et al., 2014), future investigations of the remodeling of collagen and elastin as well as their interactions are necessary to better understand the elevated longitudinal stiffening of human descending thoracic aorta.

Constitutive modeling results suggest a significant contribution of collagen crosslinking to aortic biaxial mechanical behavior regardless of age, as significant improvements of the goodness of fit are achieved by considering crosslinking as measured by R^2, RMSE and AIC_C in all age groups (Figure 3.7). The strain energy density contributed by crosslink deformation is considerable in all age groups (Figure 3.8a). This is corroborated by the fact that the amount of collagen crosslinks, pyridinoline and AGEs per collagen molecule, is already substantial in the thoracic aorta of young rats and the amount of AGEs keeps increasing with age after maturation (Brüel and Oxlund 1996). Even for the thoracic aorta of young rats (11 weeks old), eliminating pyridinoline significantly reduces the stiffness of the tissue (Brüel et al., 1998). On the other hand, considering collagen crosslinking is even more important in the aged group. Compared

with the reduced fitting capacity of the model without crosslinking in the aged group, the model considering crosslinking showed sustained fitting capability for all age groups (Figure 3.7). The positive correlation of W_c/W and W_{cf}/W with age (Table 3.4) along with the increase of W_c/W and W_{cf}/W in the >60 years group (Figure 3.8) further confirms the essential role of collagen crosslinking in regulating aortic biaxial stress-stretch behavior as well as the capacity of the new model in describing aging induced aortic stiffening.

Exponential functions were adopted for the strain energy density of crosslink deformation and crosslink-fiber interaction (Equations 3.5 and 3.8), as compared to quadratic functions proposed by Holzapfel and Ogden (2020). Molecular dynamics simulations have found that the force-displacement curves of enzymatic collagen crosslinks under tension are highly nonlinear with distinct toe and knee regions (Depalle et al., 2015). In this study, increasing nonlinearity was observed in the Cauchy stress-stretch curves of human aorta with aging (Figure 3.2), which calls for exponential functions with a more nonlinear nature and better fitting capability for describing the crosslinking-related mechanical responses. Although not reported here, with quadratic strain energy density functions, we found that crosslink deformation and crosslink-fiber interaction would dominate the biaxial mechanical response of samples in the <40 years age group where less nonlinear stress-stretch behaviors are exhibited.

In this study, extensions of fibers and crosslinks are decoupled from the constitutive relation of crosslink-fiber interaction (Equations 3.6 and 3.8), to avoid the opposite mathematical effects of the extension and rotation kinematics on I_8 in biaxial

deformation configuration while maintaining the simplicity of the constitutive model with minimal parameters (Equation 3.8). This is because that both fibers and crosslinks will be elongated under biaxial stretch (Equations. A.4 and A.5) and lead to an increase of the magnitude of I_8, while the relative rotation between bonded fiber and crosslink might either increase or decrease the magnitude of I_8 depending on multiple factors such as the initial angle between the longitudinal direction of the aorta sample and fiber orientation (θ), the initial angle between fiber and crosslink (α_0), and the ratio of stretches between the circumferential and longitudinal directions, as shown in Equation A.7. The relative rotation between bonded fiber and crosslink leads to an increase of the magnitude of I_8 only when $cos\alpha^+/cos\alpha_0$ and $cos\alpha^-/cos(180° - \alpha_0)$ are greater than 1, which is not guaranteed under biaxial stretch as shown in Figures A.1-A.5 of Appendix A.

Although our study focuses on the descending thoracic aorta, difference in the stiffening behavior between the longitudinal and circumferential directions was found along the entire length of the aorta (Haskett et al., 2010). However, the degree of aging-induced stiffening was found to increase from proximal to the distal regions along the aortic tree from both clinical reports and animal model studies (Hickson et al., 2010; Ferruzzi et al., 2018). With an increasing collagen to elastin ratio (Sokolis, 2007; Concannon et al., 2020), a decreasing undulation and alignment of collagen fibers (Haskett et al. 2010; Zeinali-Davarani et al. 2015) and a decreasing density of pyridinoline crosslinks (Whittle et al., 1987) from the proximal to the distal regions along the aortic tree, remodeling of individual ECM components and their interaction with aging is likely to be regional dependent. Structural-based constitutive modeling will be a

powerful tool in understanding the regional-dependency in aging and pathophysiology of the aorta.

3.5 Limitations

Several limitations regarding the experimental and modeling approaches of this study need to be pointed out. For mechanical testing, due to the required size of the aortic tissue samples for planar biaxial tensile testing, the circumferential variation in stiffness and thickness of the descending thoracic aorta, as previously reported (Kim and Baek, 2011; Rouleau et al., 2012; Kim et al., 2013), was not taken into consideration. Two-fiber family model is adopted to consider collagen crosslinking. However, the modeling framework can be extended to constitutive models in which fiber dispersion and/or additional fiber families are considered (Gasser et al., 2006; Zeinali-Davarani et al., 2009; Jadidi et al., 2020; Holzapfel et al., 2015). Description of the crosslink-fiber interaction is rather phenomenological due to the lack of information on the interaction mechanisms between crosslinks and fibers. Future models with a refined structural representation of collagen crosslinks would lead to a more robust constitutive descriptor of aortic mechanics. In addition, the affine deformation assumption of the constitutive modeling approach adopted in this study could underestimate the reorientation underwent by the fiber and crosslink segments of the interconnected network (Chandran and Barocas, 2006).

Although this study focuses on collagen crosslinking, aortic stiffening results from combined effects of ECM remodeling and interactions of the constituents. The

deposition, crosslinking and decreased undulation of collagen could have a combined effect on the biaxial stiffness of the aorta. As a laminated fibrous soft tissue, each aortic layer undergoes unique microstructural alterations with aging (Amabili et al., 2021; Franchini et al., 2021). Layer-specific changes in ECM constituents may play important roles in the stiffening behavior of the aorta. Elastin fragmentation, which was observed with aging (Spina and Garbin, 1976; Schlatmann and Becker, 1977; Toda et al., 1980), may release the compressive stress exerted on collagen fibers and thus promote early collagen recruitment (Chow et al., 2014). The stiffness of vascular smooth muscle cells also increases with aging in the aorta (Qiu et al., 2010). While aging is the focus of this study, future studies are needed in understanding the role of crosslinking in aortic function considering the complex interplay among multiple physiological and pathological factors, such as aging, sex, and cardiovascular diseases.

3.6 Conclusions

Despite the reported increasing crosslinking density with aging, the mechanistic role of collagen crosslinking in aortic stiffening is yet to be delineated. In this study, the mechanical behavior of human descending thoracic aorta with aging was studied through constitutive modeling coupled with biaxial tensile testing. Our study revealed anisotropic stiffening of the arterial wall with the longitudinal direction stiffens more rapidly than the circumferential direction with aging. A constitutive model incorporating collagen crosslinking and deformation as well as crosslink-fiber interaction was developed to study the contribution of collagen crosslinking in regulating aortic stress-stretch behavior.

The modeling results demonstrated an increased contribution of collagen crosslinking to aortic mechanical properties with aging. Results from this study are important for elucidating the mechanistic mechanism of aortic stiffening with aging and the establishment of biomechanical-based metrics for vascular health assessment.

CHAPTER 4 MECHANICAL AND STRUCTURAL CONTRIBUTIONS OF ELASTIN AND COLLAGEN FIBERS TO INTERLAMELLAR BONDING IN THE ARTERIAL WALL

4.1 Overview

The artery relies on interlamellar structural components, mainly elastin and collagen fibers, for maintaining its integrity and resisting dissection propagation. In this study, the contribution of arterial elastin and collagen fibers to interlamellar bonding was studied through mechanical testing, multiphoton imaging and finite element modeling. Steady-state peeling experiments were performed on porcine aortic media and the purified elastin network in the circumferential (Circ) and longitudinal (Long) directions. The peeling force and energy release rate associated with mode-I failure are much higher for aortic media than for the elastin network. Also, longitudinal peeling exhibits a higher energy release rate and strength than circumferential peeling for both the aortic media and elastin. Multiphoton imaging shows the recruitment of both elastin and collagen fibers within the interlamellar space, and points to in-plane anisotropy of fiber distributions as a potential mechanism for the direction-dependent phenomena of peeling tests. Three-dimensional finite element models based on cohesive zone model (CZM) of fracture were created to simulate the peeling tests with the interlamellar energy release rate and separation distance at damage initiation obtained directly from peeling test. Our experimental results show the separation distance at damage initiation is 80 "μm" for aortic media and 40 "μm" for elastin. The damage initiation stress was estimated from the model for aortic media (Circ: 60 kPa; Long: 95 kPa) and elastin (Circ: 9 kPa; Long:

14 kPa). The interlamellar separation distance at complete failure was estimated to be 3 - 4 mm for both media and elastin. Furthermore, elastin and collagen fibers both play an important role in bonding of the arterial wall, while collagen has a higher contribution than elastin to interlamellar stiffness, strength and toughness. These results on microstructural interlamellar failure shed light on the pathological development and progression of aortic dissection.

4.2 Introduction

Aortic dissection is a serious cardiovascular disease that is often missed in antemortem diagnosis (Spittell et al. 1993) and is associated with a high rate of mortality (Hagan et al. 2000; Khan and Nair 2002). In general, three distinct stages are involved in the development of arterial dissection. It usually begins with a tear cutting in the intima (Thubrikar et al. 1999), which allows blood flow to enter the newly created interlamellar lumen in the arterial wall and spread both circumferentially and longitudinally in the media (Tam et al. 1998); damage of the media can further propagate radially across the lamellae, either back into the intima, or outwards to the adventitia causing devastating rupture of the arterial wall (Sommer et al. 2008). Microscopically, the dissection process involves failure of interlamellar elastin and collagen fibers, the two primary load bearing extracellular matrix (ECM) constituents in the artery (Pal et al. 2014). For a better understanding of the etiology and improved diagnosis of this disease, it is important to quantitatively examine the contribution of elastin and collagen to interlamellar bonding within the arterial wall.

The aortic media is composed of thick concentric elastic lamellae with a closely interwoven complex of collagen and elastin fibers in the narrow interlamellar space (Wolinsky and Glagov 1964, 1967). Using scanning electron microscopy, interlamellar elastin fibers were found to stem from an elastic lamella, protrude obliquely and terminate in the neighboring interlamellar space and account for 27% of the total elastin volume, and about 2% of elastic fibers are thick struts that provide direct connection between adjacent lamellae (O'Connell et al. 2008). More recently, radially-running elastin and collagen fibers were observed in human ascending thoracic aortic media using multiphoton imaging (Tsamis et al. 2013). Multiple studies have suggested that the propagation path of aortic dissection happens in the aortic medial layer (Erbel et al. 2001; Khan and Nair 2002; Nienaber and Clough 2015; Nienaber et al. 2016; Manopoulos et al. 2018). Histological investigations of dissected human ascending thoracic aorta reported that the plane of dissection was in the outer media, and about 1/5 to 1/10 of the media was attached to the adventitia in the outer half of the dissected aortic wall (Manopoulos et al. 2018). In addition, in most cases an underlying chronic and generalized disease of the aortic media, such as aortic aneurysm (Erbel et al. 2001; Pasta et al. 2012) and Marfan's syndrome (Nienaber and Clough 2015), alters the interlamellar fiber micro-architectural (Tsamis et al. 2013) and predisposes the aorta to dissection (Khan and Nair 2002). Therefore, knowing the relationship between the integrity and interlamellar bonding properties of the aortic media is important to understand the mechanisms of aortic dissection.

Experimental methods used to measure the interlamellar dissection properties of

arterial tissues include pressurization (Carson and Roach 1990; Roach and Song 1994; Tam et al. 1998), direct tension in the radial direction (MacLean et al. 1999; Sommer et al. 2008; Tong et al. 2011), and peeling tests (Sommer et al. 2008; Tong et al. 2011, 2014; Pasta et al. 2012; Wang et al. 2011, 2014; Noble et al. 2016; Leng et al. 2018). More comprehensive review on the experimental assessment of arterial dissection can be found in previous work by Tong et al. (Tong et al. 2016) and Sherifova and Holzapfel (Sherifova and Holzapfel 2019). The pressurization test measures the interlamellar strength and energy release rate at a specific location, however the elastic energy stored within the deformed tissue cannot be separated from the total external applied work and thus compromises the accuracy of the measured energy release rate. The direct tension test provides local interlamellar stiffness and strength, but data for energy release rate is missing in this method due to complex damage modes towards the end of a test. The peeling test, however, has the advantage of ensuring a distinct separation of neighboring layers within the media as well as continuously characterizing the energy release rate of the tissue over a large interfacial area, and is used in this study.

Several computational models have been employed to investigate the development of arterial dissection. For example, discrete fiber network model was used to assess the effects of structural features of collagen fibers and elastic lamellae on the in-plane strength of the intimal layer, which governs the occurrence of a tear in the intima (Thunes et al. 2018). Constitutive modeling with image-based microstructural parameters points to alterations in collagen fiber architecture and corresponding wall stress distribution in aortic aneurysm (Pasta et al. 2016). Computational fluid dynamics models

were used to study the effects of flow pattern and pressure distribution on the tearing force (Chitsaz et al. 2012; Zhang et al. 2014), the correlation between entry tear size and flow rate in the patent false lumen (Rinaudo et al. 2014), as well as the alteration of hemodynamics in dissected aorta (Dillon-Murphy et al. 2016). It has been found that a greater entry tear adversely leads to a greater flow in the false lumen, and the pressure imbalance between the true and false lumen is the driving force for propagation of the crack tip in the false lumen. The cohesive zone model (CZM) has been widely used to simulate the propagation of arterial dissection (Gasser and Holzapfel 2006; Ferrara and Pandolfi 2010; Pal et al. 2014; Wang et al. 2017; Leng et al. 2018), as well as atherosclerotic plaque delamination (Ferrara and Pandolfi 2008; Leng et al. 2015, 2016; Merei et al. 2017). Reviews on the modeling studies of arterial dissection can be found from previous work by Doyle and Norman (Doyle and Norman 2016), Tong et al. (Tong et al. 2016) and Gültekin and Holzapfel (Gültekin and Holzapfel 2018). However, many of the previous CZM-based studies focused on setting up of the model, and the associated model parameters were often phenomenological.

This study aims to understand the contribution of elastin and collagen fibers to interlamellar bonding in the arterial wall. Steady-state mode-I peeling tests were carried out on porcine aortic media as well as purified elastin network. The peeling force as well as the energy release rate were obtained for each sample. Multiphoton imaging was performed to gain insights into the structural roles of elastin and collagen fibers in resisting delamination during peeling tests. Peeling of the media and elastin was simulated using three-dimensional (3D) finite element models that were based on CZM

of fracture (Dugdale 1960; Barenblatt 1962). Material parameters of the CZM were directly related to the structural and mechanical parameters obtained from experiments. The mechanical and structural roles of elastin and collagen fibers in interlamellar bonding were then discussed.

4.3 Material and methods

4.3.1 Sample preparation

Fresh proximal descending porcine thoracic aortas (12–24 months old) were harvested from a local abattoir and transported on ice to our laboratory. Aortas were cut into approximately 40 mm × 10 mm rectangular samples (Figure 4.1a) with the long edge oriented either in the circumferential or longitudinal directions. Aortic media was obtained by carefully removing the adventitia, thus similar mechanical properties can be expected on both sides of the tear during peeling test (Noble et al. 2016). The boundary between the adventitia and the media was easy to identify because the media is laminated and more structured than the adventitia (Holzapfel et al. 2005, 2007; Sommer et al. 2008). When preparing the aortic media samples, we peeled the adventitia from the outer surface of the aortic wall until a smooth and laminated organization was seen, indicating that the adventitial layer has been removed. A total of 8 aortic samples of 2 cm × 2 cm squares with one edge parallel to the circumferential direction and the other parallel to the longitudinal direction were also prepared for biaxial tensile tests.

Purified elastin was isolated using a cyanogen bromide (CNBr) treatment method to remove cells, collagen and other ECM components (Lu et al. 2004, Zou and Zhang

2009) from the media. Previous studies have shown that this purification method maintains the structure and function of the elastin network (Rasmussen et al. 1975; Lu et al. 2004; Zou and Zhang 2009). Briefly, aortic media samples were kept in 50 mg/ml CNBr in 70% formic acid at room temperature for 19 h, then at 60 °C for 1 h with gentle stirring, followed by boiling for 5 min to inactivate CNBr. A total of 24 rectangular samples were prepared, of which half were aortic media and the other half were purified elastin. Both aortic media and purified elastin network include 6 circumferentially oriented and 6 longitudinally oriented strips. All samples were rinsed several times and then stored in 1× phosphate buffered saline (PBS) for further mechanical testing and imaging.

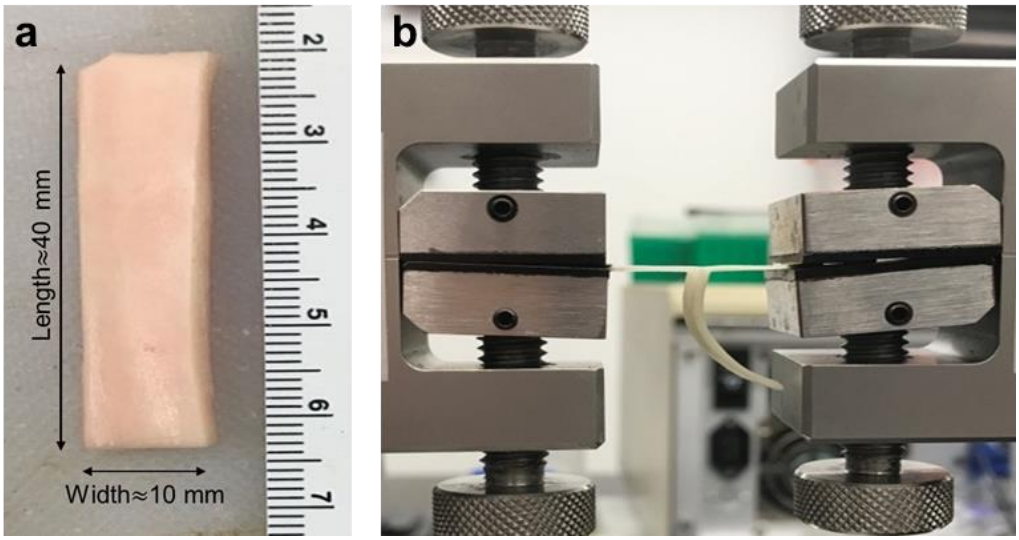

Figure 4.1 a A rectangular porcine aorta sample; and b mode-I peeling test of the aortic media.

4.3.2 Peeling test

Refer to Section 2.3 for a detailed description of the experimental protocol. Briefly, dissection of the media was initiated in each sample by introducing a 10 mm incision at one end of the sample and creating two "tongues" of about equal thickness. The thickness, width and bonded length of each rectangular tissue strip were measured using a digital caliper. The two tongues were glued to the sandpaper and clamped by grips attached to a uniaxial tensile tester (Instron, Norwood, MA), as shown in Figure 4.1b. A 10 N static load cell with a tolerance of ±0.25% of reading was used. Steady-state peeling tests were conducted by fixing one tongue of the sample and pulling away the other tongue at a rate of 0.2 mm/s to complete delamination. The displacement of the moving grip and the reaction peeling force during the delamination process were recorded at a frequency of 5 Hz, which provides a sampling interval of 0.04 mm. The energy release rate (G_c, with an alternative interpretation as interlamellar toughness, i.e., the energy required to split a unit area of the interface) can be calculated by Equation 2.2.

4.3.3 Planar biaxial tensile test

Planar biaxial tensile tests were performed to characterize the in-plane mechanical properties of the aortic media. Refer to Section 2.2 for more details of the testing method. Tension control was used in the experiment. A preload of 5 N/m was applied to straighten the sutures before testing. For preconditioning, 8 cycles of 40 N/m equibiaxial load were applied to the tissue to obtain repeatable mechanical response. Then, samples were subjected to 8 cycles of 300 N/m equibiaxial load. Assuming plane stress and

incompressibility, force-displacement data from the last cycle was used to calculate Cauchy stress and stretch using Equation 2.1 (Zou and Zhang 2009).

4.3.4 Statistical analysis

Peeling force/width and energy release rate data were presented as mean ± standard deviation. Two-tailed unpaired t-tests were used for statistical comparison with $p < 0.05$ considered as statistically significant.

4.3.5 Finite element model setup

To gain insights into the interlamellar bonding in arterial tissues, 3D finite element models that capture the anisotropic mechanical behavior of the tissue were created in ABAQUS (version 6.14, Simulia, Providence, RI). The model consists of two initially separated tongues at the top and a single layer of cohesive elements sandwiched between the lamellar layers of the media (Figures. 3.2a, 3.2c and 3.2d). The thickness for aortic media and purified elastin was obtained by averaging experimental measurements, which was found to be 1.83 ± 0.17 mm for aortic media and 1.08 ± 0.13 mm for purified elastin. 3D 8-node brick elements (C3D8) were used for the media tissue and 8-node cohesive elements (COH3D8) were used for the cohesive zone. A mesh size dependency study was performed by varying the size of cohesive elements along the direction of dissection propagation (Y-direction in Figure 4.2). The peeling processes were simulated using a mesh size of 0.28 mm, 0.2 mm and 0.16 mm. As shown in previous studies

(Turon et al. 2007; Ferrara and Pandolfi 2010), coarser mesh gives a greater amplitude of the force oscillation but increases the mean value of the plateau regime on the force/width-displacement curve slightly. To improve the accuracy of the simulation and also consider the computational efficiency, the mesh size 0.2 mm was chosen for this study. The simulated peeling force/width was found to converge without spurious oscillations (Turon et al. 2007) using this mesh size. In addition, to further ensure the accuracy of the simulation, there were of 9 rows of cohesive elements within the damaged zone, i.e., the region from the delamination tip (where traction is zero) to the cohesion zone tip (where traction just reaches the critical point of damage initiation), as shown in Figure 4.2e.

To minimize the effect of boundary clamping on the simulated reaction forces, equal and opposite X-displacement were prescribed on the two end surfaces to induce delamination. The Y-displacement of the bottom surface of the specimen in Figure 4.2a was constrained. Also, the node on the center of the bottom surface was pinned to keep the whole model from moving in the Z direction. The reaction force as well as displacement in the X direction of the right end surface was extracted at each incremental step and compared to the averaged experimental peeling force/width-displacement data for all sample groups.

Simulation of the biaxial tension test was performed to determine the material parameters associated with the in-plane mechanical properties of aortic media and purified elastin network. Due to symmetric geometry and loading conditions, a quarter of the square sample was created in ABAQUS. The model was meshed using general-

purpose shell elements (S4R) with inherent plane stress assumption. Symmetric boundary conditions were prescribed on two corresponding edges, while equibiaxial tensile loads were applied on the other two edges. Cauchy stress and stretch in the circumferential and longitudinal directions were obtained from the model and compared with experimental results.

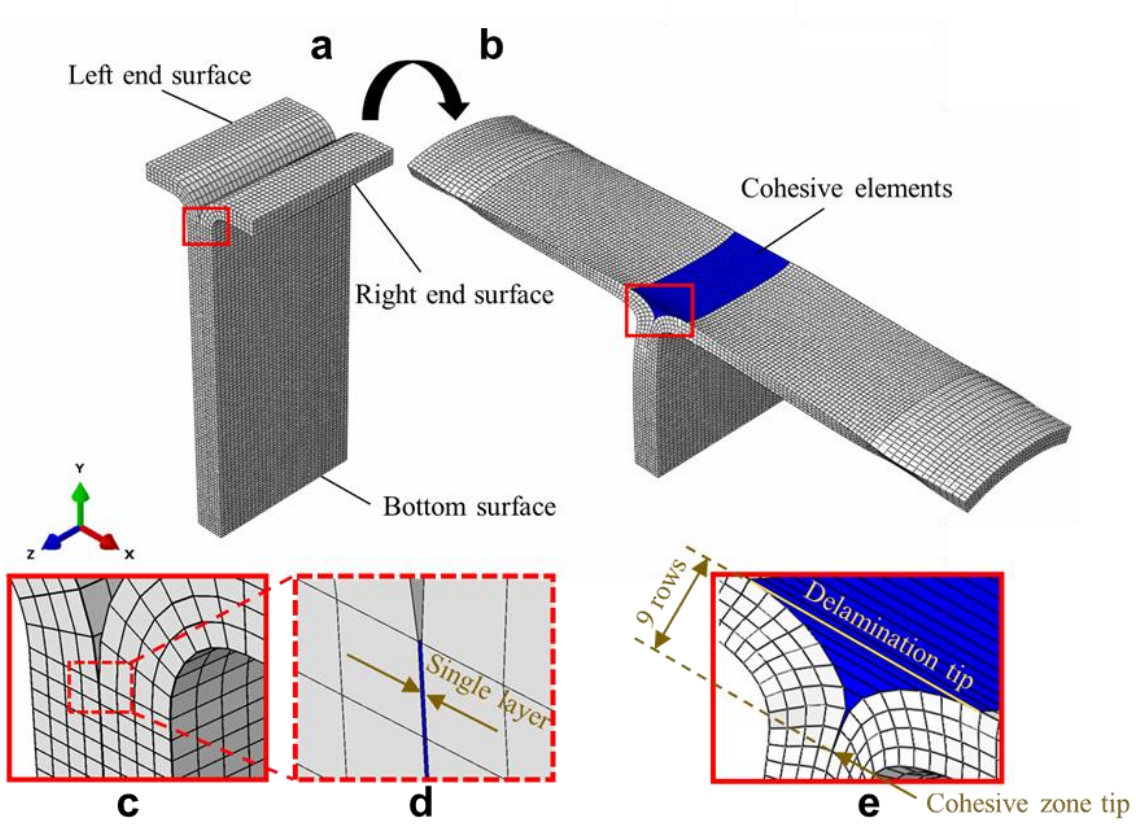

Figure 4.2 Three-dimensional finite element model of mode-I peeling of the arterial media. a Undeformed configuration; b deformed configuration; c and d detailed views of the cohesive elements (blue) sandwiched between the brick elements (gray) in the undeformed configuration; and e detailed view of the damaged zone containing 9 rows of cohesive elements in the simulation of damage propagation in the deformed configuration.

4.3.6 Constitutive modeling

CZM with bilinear traction-separation relation shown in Figure 4.3 was employed to simulate the interfacial delamination during peeling tests. Since the testing method adopted is an opening-mode dominated failure process (Leng et al. 2018), only mode-I failure was considered in our simulation. The bilinear traction-separation law is fully characterized by three independent parameters: traction at damage initiation (t_0, with an alternative interpretation as interlamellar strength - the maximum elastic stress the interlamellar bonding can sustain before failure occurs), separation distance at damage initiation (δ_0), and energy release rate (G_c) which is equal to the area under the curve (Figure 4.3).

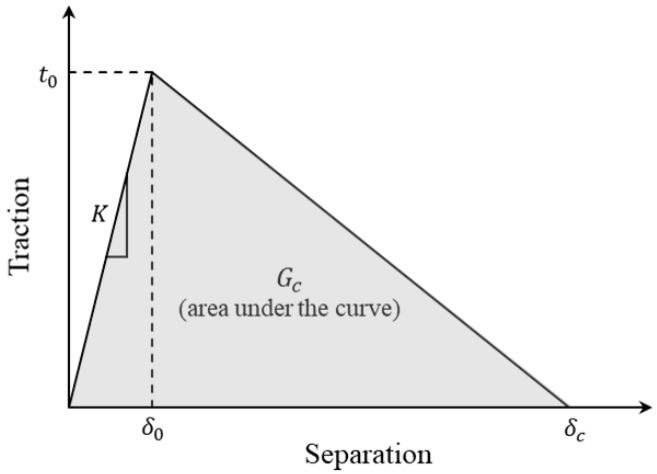

Figure 4.3 Bilinear traction-separation law for the cohesive elements.

Both aortic media and purified elastin network were modeled as a nearly incompressible anisotropic hyperelastic material with strain energy density function defined as (Holzapfel et al. 2000; Gasser et al. 2006):

$$W = C_{10}(\bar{I}_1 - 3) + \frac{k_1}{2k_2}\sum_{i=1,2}\{exp[k_2\langle\bar{E}_i\rangle^2] - 1\} + \frac{1}{D}\left(\frac{J^2-1}{2} - \ln J\right) \quad (4.1)$$

where the first term originates from the isotropic amorphous ground matrix, and the second term represents the mechanical response of two families of dispersed fibers embedded in the matrix. $\bar{I}_1$ is the first deviatoric strain invariant. C_{10} is related to the stiffness of the ground substance and has the unit of stress. k_1 is another stress like parameter for fibers and k_2 is a dimensionless parameter governing the nonlinearity of fibers at large strain. The strain-like quantity $\bar{E}_i = \kappa(\bar{I}_1 - 3) + ((1 - 3\kappa)\bar{I}_{4i} - 1)$ characterizes the deformation of each family of fibers, in which κ is the dispersion parameter ($0 \leq \kappa \leq 1/3$), and $\bar{I}_{4i}$ is the square of stretch along the mean direction of fibers. θ denotes the angle between the mean fiber direction and the longitudinal direction of the aorta. The third term in Equation 4.1 accounts for volume change of the sample. D is analogous to the inverse of the bulk modulus, and J is the volume ratio.

4.3.7 Identification of model parameters

The CZM has three parameters, G_c, δ_0 and t_0. The average energy release rate within each sample group, obtained using Equation 2.2, was used as G_c. Parameter δ_0 was also obtained from the experimental data. As shown in Figure 4.4a, the displacement increments (Δd) associated with each ramp up of the peeling force were collected from all curves within each sample group, of which the median value was taken as the separation distance at damage initiation (δ_0) for the CZM. The force ramp ups were filtered by eliminating force oscillations under the tolerance of the load cell. Finally,

parameter t_0, traction at damage initiation, was adjusted to fit the simulated peeling force to averaged experimental measurements. The mean absolute percentage error (MAPE) between the simulated results and experimental data is defined as

$$MAPE = \frac{1}{n}\sum_{i=1}^{n}\left|\frac{f_{sim,i}-f_{exp}}{f_{exp}}\right| \quad (4.2)$$

where $f_{sim,i}$ is the ith peeling force/width data point from simulation and f_{exp} is the averaged value of peeling force/width from experiments. n is the total number of data points to be compared. Because of the built-in numerical oscillations of the simulated reaction peeling force (Schellekens and De Borst 1993), the fitting was considered acceptable when MAPE was smaller than 5%. Once t_0 was identified, the initial interlamellar stiffness (K), as well as the separation distance at complete delamination (δ_c), can be calculated as $K = t_0/\delta_0$ and $\delta_c = 2G_c/t_0$.

To determine the anisotropic hyperelastic material properties of aortic media and purified elastin network, the simulated Cauchy stress-stretch of equibiaxial tension was fitted to the averaged experimental data, which was from the planar biaxial tensile tests in this study for the media (Figure 4.5). For purified elastin network, the average Cauchy stress-stretch data based on 6 samples from a previous study was used (Wang et al. 2015). Material parameters for modeling the anisotropic hyperelastic behavior of arterial media and purified elastin network are summarized in Table 4.1.

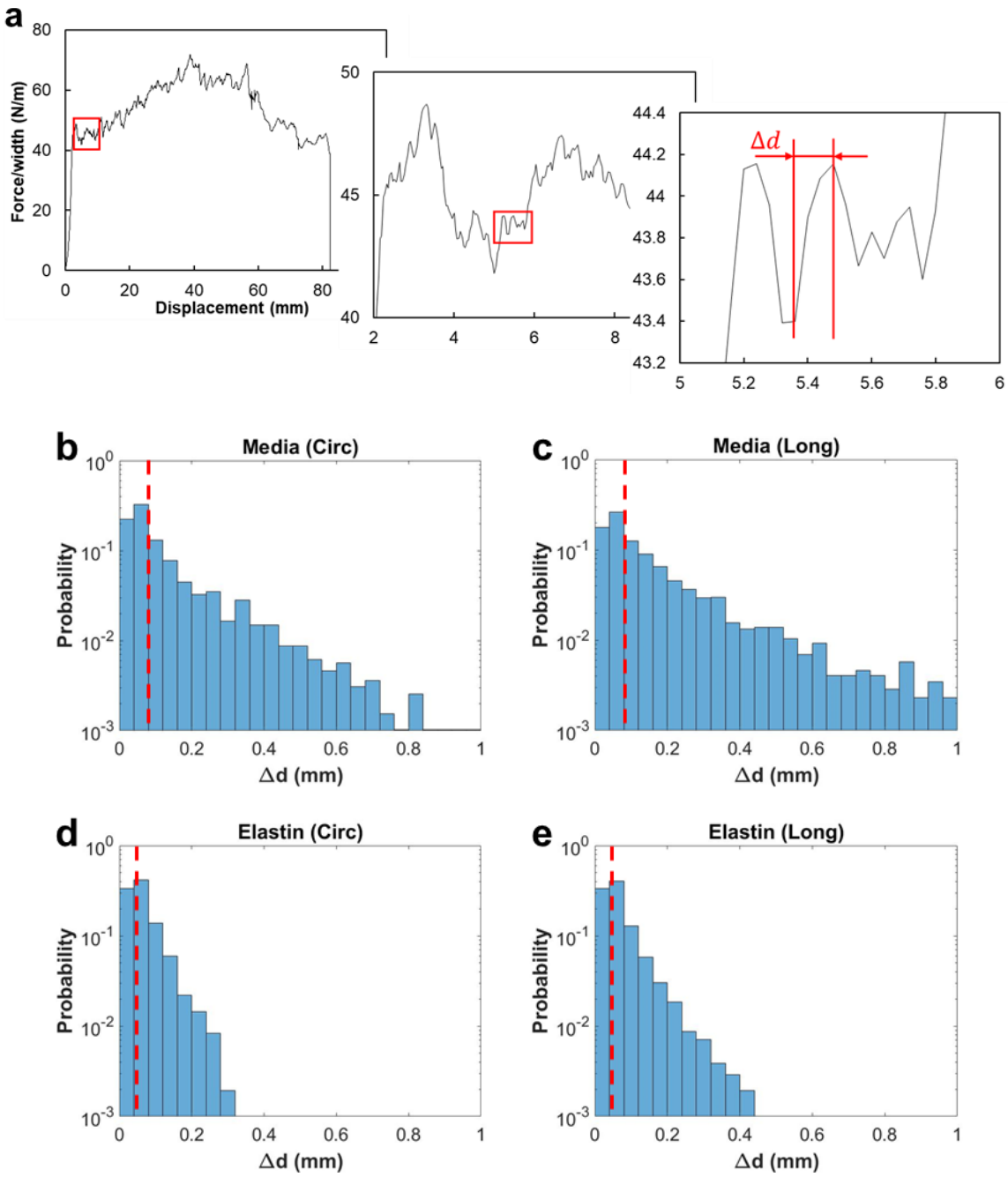

Figure 4.4 a A representative peeling force/width-displacement curve and its zoom-in graphs showing the high frequency oscillation of the peeling force; and b-e distribution of $\Delta \boldsymbol{d}$ from peeling tests of aortic media and elastin in the circumferential (Circ) and longitudinal (Long) directions. Dashed lines in b-e indicate the location of the median. Note that the vertical axis in b-e are in the logarithmic scale.

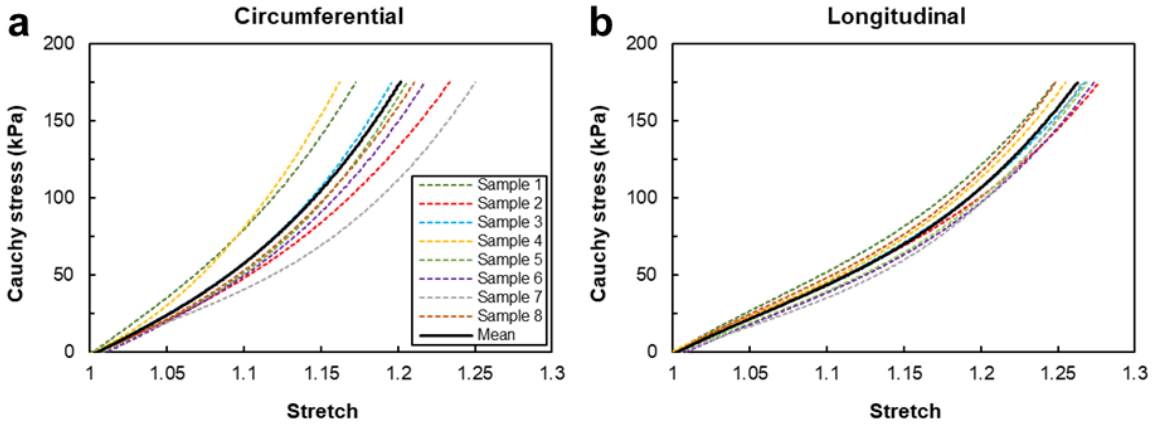

Figure 4.5 Experimental Cauchy stress-stretch curves of biaxial tensile tests of porcine aortic media in the a circumferential and b longitudinal directions. The thick black curves represent the arithmetic means.

Table 4.1 Material parameters for the anisotropic hyperelastic behavior of arterial media and elastin network.

	$C_{10}\ (kPa)$	$k_1\ (kPa)$	k_2	κ	θ
Media	16.3	250	0.8	0.226	42.2
Elastin	18.3	331	0.01	0.228	43.5

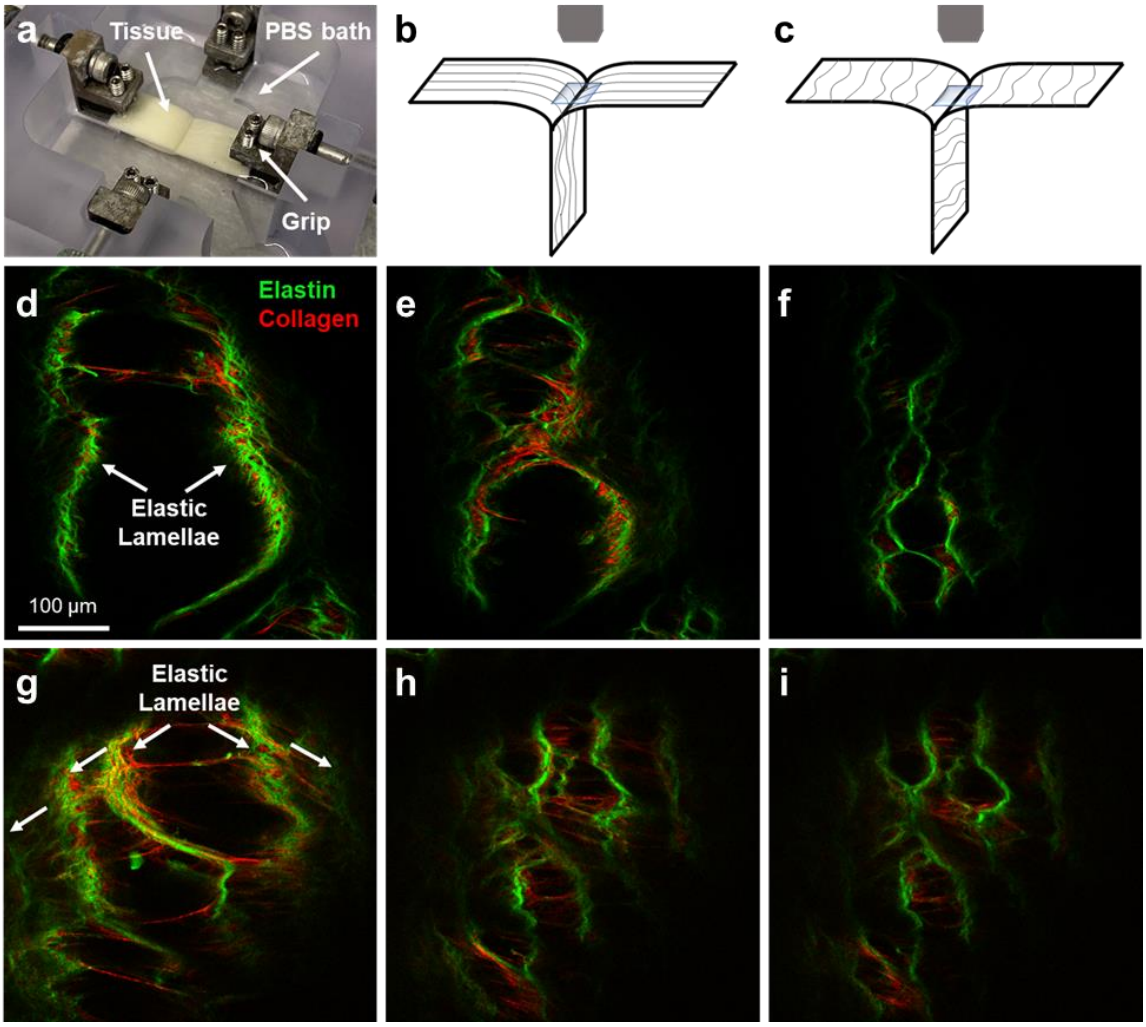

Figure 4.6 a The custom-built device for multiphoton imaging of the peeling forefront; b experimental setup of multiphoton imaging of peeling of aortic tissues in the circumferential direction and c longitudinal direction with preferred orientation of in-plane fiber distribution; d-f multiphoton image of different depth of the peeling site of porcine aortic media obtained from a circumferential tissue strip and g-i a longitudinal tissue strip. Imaging depth increases from d to f and from g to i.

4.3.8 Multiphoton imaging

Multiphoton imaging was performed using an inverted multiphoton microscopy system (Carl Zeiss LSM 710 NLO) with a 20× water immersion objective lens with

0.83 μm × 0.83 μm pixel size. The femtosecond IR pulse laser was set to 810 nm to generate two-photon excited fluorescence (2PEF) from elastin (525/45 nm) and second harmonic generation from collagen (417/80 nm) (Chow et al. 2014; Yu et al. 2018a, b). Additional samples (one in circumferential and one in longitudinal direction) were mounted on a custom-built device (Figure 4.6a) that allows imaging at the forefront of the peeling site. A z-stack image of about 50 μm in depth with 1 μm distance in between the adjacent images and a field of view of 425 μm × 425 μm was acquired at the delamination tip (Figures 4.6b and 4.6c).

4.3 Results

Figure 4.7 shows the experimental force/width-displacement data from mode-I peeling of porcine aortic media and purified elastin network in both the circumferential and longitudinal directions. The initial increase of the peeling force arises from uniaxial stretch of the two separated "tongues". The peeling force plateaus as delamination starts to propagate along the interlamellar bonding of the sample. Averaged peeling force/width (F/W) and energy release rate (G_c) for all four sample groups were extracted from the delamination phase of the experimental curves in Figure 4.7 and reported in Figures 4.8a and 4.8b. The F/W in the aortic media (Cir: 46.00 ± 11.86 N/m; Long: 72.27 ± 22.28 N/m) was found to be significantly higher (p=0.0001) than elastin (Circ: 6.97 ± 1.15 N/m; Long: 9.71 ± 1.76 N/m). Similarly, significantly higher (p=0.0001) dissection energy G_c was found in the aortic media (Circ: 106.42 ± 25.82 J/m^2; Long: 183.78 ± 58.08 J/m^2) than in elastin (Circ: 14.89 ± 2.41 J/m^2; Long: 21.35 ± 3.81 J/m^2).

Peeling direction has a strong effect on the peeling force/width and energy release rate. For both aortic media and purified elastin network, longitudinal strips exhibit higher peeling force/width and energy release rate with larger variations (Figures 4.8a and 4.8b). Compared with circumferential samples, the mean peeling force/width in longitudinal samples are 57% and 39% higher for aortic media and purified elastin network, respectively; the mean energy release rate in longitudinal samples are 73% and 43% higher for aortic media and purified elastin network, respectively.

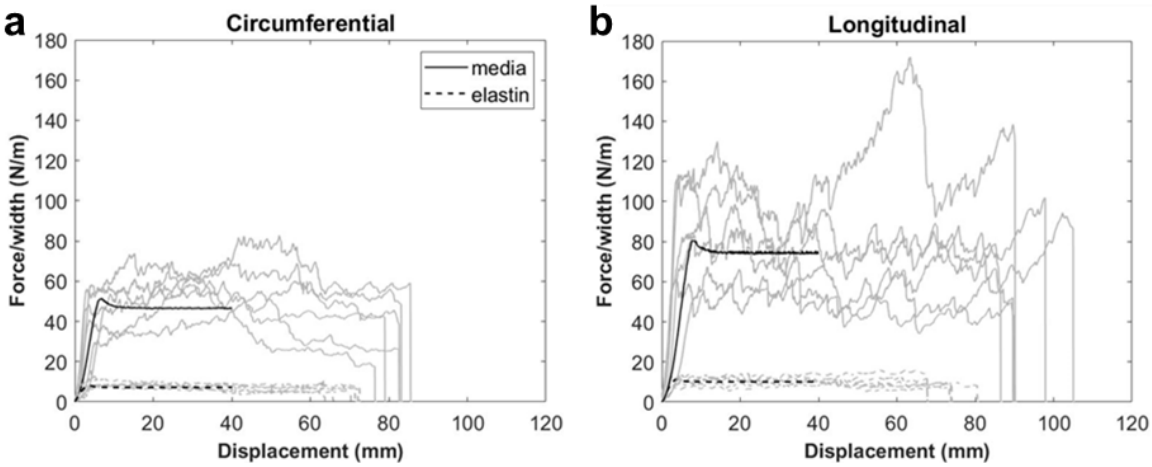

Figure 4.7 Experimental (gray) and simulated (black) curves of peeling force/width-displacement for aortic media and purified elastin network in the a circumferential and b longitudinal directions.

All experimental peeling force profiles exhibit high frequency oscillation (Figure 4.4a). Figures 4.4b-e show the distribution of Δd and its median obtained from peeling tests of aortic media and elastin in both the circumferential and longitudinal directions. It can be observed that in aortic media, Δd spreads over a range of 0.04 - 1 mm (Figures 4.4b and 4.4c); while in elastin, Δd is distributed within a narrower range in which the

maximum value is approximately 0.3 - 0.4 mm (Figures 4.4d and 4.4e). Figure 4.8c reports the separation distance at damage initiation (δ_0) for interlamellar bonding identified from the distribution of Δd. In purified elastin network, removal of collagen fibers and other ECM and cell components reduces δ_0 by half. The direction of delamination propagation seems to have little effect on δ_0.

Table 4.2 Material parameters for the cohesive zones of arterial media and elastin network. (Circ: circumferential; Long: longitudinal; $\boldsymbol{G_c}$: energy release rate; $\boldsymbol{\delta_0}$: separation distance at damage initiation; $\boldsymbol{t_0}$: traction at damage initiation; $\boldsymbol{K}$: initial interlamellar stiffness; $\boldsymbol{\delta_c}$: separation distance at complete delamination; MAPE: mean absolute percentage error).

	Parameters obtained from experiments		Parameters obtained from the model			
	G_c (J/m^2)	δ_0 (mm)	t_0 (kPa)	K (kPa/mm)	δ_c (mm)	MAPE
Media (Circ)	106.42	0.08	60	750	3.55	1.2%
Media (Long)	183.78	0.08	95	1187.5	3.87	2.9%
Elastin (Circ)	14.89	0.04	9	225	3.31	3.2%
Elastin (Long)	21.35	0.04	14	350	3.05	4.0%

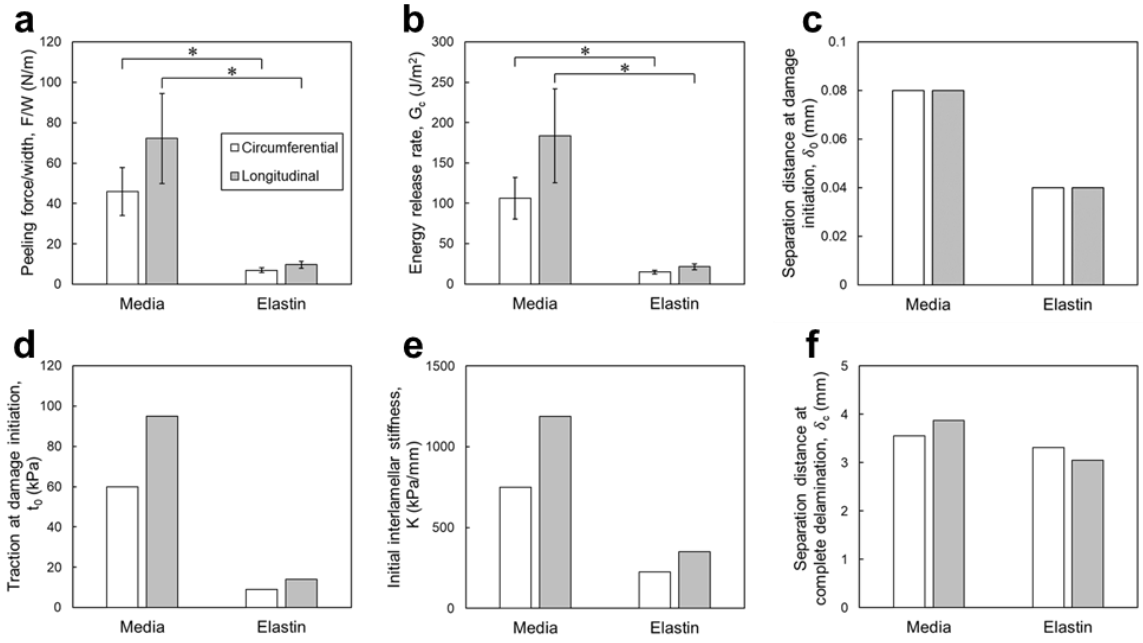

Figure 4.8 a–c Experimental and d–f simulation results from peeling of aortic media and purified elastin network in the circumferential and longitudinal directions. ($^{*}p<0.05$).

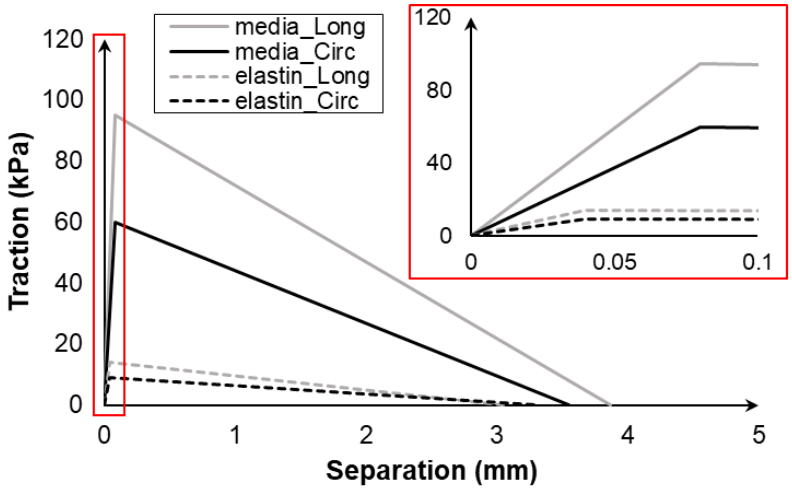

Figure 4.9 Traction-separation relations for the cohesive zone of aortic media and purified elastin network determined from peeling tests in the circumferential and longitudinal directions. Inset figure shows the initial regime of the cohesive zone. (Circ=circumferential, Long=longitudinal).

CZM parameters identified from peeling tests and simulations are listed in Table 4.2. Besides G_c and δ_0 which were determined directly from experimental measurements, simulation results provide further information about the interlamellar bonding strength (t_0) and stiffness (K), as well as separation distance at complete delamination (δ_c) in the arterial wall. Simulation results revealed that interfacial stiffness and strength also decrease significantly in purified elastin network compared with aortic media. In both circumferential and longitudinal elastin samples, K and t_0 were found to reduce by approximately 70% and 85% from aortic media samples with the same orientation (Figures 4.8d and 4.8e). Peeling direction also has a strong effect on the bonding strength and stiffness. In both aortic media and purified elastin network, both the interlamellar stiffness and strength estimated from longitudinal peeling are more than 50% higher than those from circumferential peeling (Figures 4.8d and 4.8e). At complete delamination, δ_c was estimated to vary between 3 - 4 mm for all sample groups, while in aortic media δ_c is slightly higher than that in purified elastin network (Figure 4.8f) (p=0.12). Traction-separation relations of the CZM for describing the mechanical response of arterial interlamellar bonding are reported in Figure 4.9.

Multiphoton images of the dissection site in the circumferential and longitudinal aortic media samples during peeling are shown in Figures 4.6d-f and 4.6g-i, respectively. Interlamellar elastin and collagen fibers can be observed between the distinct elastic lamellae. In circumferential peeling, failure appears to happen between two adjacent lamellae (Figures 4.6d-f); whereas in longitudinal peeling, radially-running fibers that are under tension can be seen within multiple interlamellar spaces, indicating multiple

lamellae are involved in the dissection process (Figures 4.6g–i).

4.4 Discussions

The purpose of this study is to understand the mechanical contribution of elastin and collagen fibers to interlamellar bonding in the arterial wall. These understandings are important for the assessment and repair of aortic dissection. The quantitative knowledge of contributions of collagen and elastin to interlamellar bonding is also beneficial to cardiovascular tissue engineering. The arterial wall contains abundant out-of-plane elastin and collagen fibers that play an important role in maintaining its integrity (Wolinsky and Glagov 1964, 1967; O'Connell et al. 2008; Tsamis et al. 2013). Low local collagen density was found at the crack initiation sites in the aorta (Sugita and Matsumoto 2018). The stiffness and failure stress of collagen fibers are 3 to 4 orders of magnitude higher than elastin fibers (Lillie and Gosline 2002; Gentleman et al. 2003; Wenger et al. 2007; Shen et al. 2008; Valiaev et al. 2008; Tang et al. 2010). Consistently, in this study, higher peeling force and energy release rate was found in the intact aortic media than in the purified elastin network (Figures 4.8a and 4.8b). Finite element simulations also pointed to higher initial stiffness (Figure 4.8e) and strength (Figure 4.8d) in the media due to the existence of interlamellar collagen fibers (Figure 4.9).

The measured energy release rate, G_c, for aortic media (106.42 ± 25.82 J/m^2 in the circumferential direction, 183.78 ± 58.08 J/m^2 in the longitudinal direction) fall within the range of 10 to 250 J/m^2 reported by other researchers (Carson and Roach 1990; Roach and Song 1994; Sommer et al. 2008; Tong et al. 2011; Pasta et al. 2012; Wang et

al. 2014; Noble et al. 2016; Leng et al. 2018) obtained from human and porcine arterial tissues. Multiphoton images (Figures. 3.5d-f and 3.5g-i) provide a potential explanation for the direction-dependent phenomena obtained from peeling tests. Since elastin and collagen fibers are more aligned toward the circumferential direction in the arterial wall (Zou and Zhang 2009; Yu et al. 2018b), it is suspected that the direction-dependent phenomena are related to the preferred in-plane fiber distribution. Due to boundary clamping, more in-plane fibers are stretched in the loading direction and constrained from reorientation during circumferential peeling (Figure 4.6b). However, the same effect could be greatly weakened in longitudinal peeling when majority of fibers are perpendicular to the loading direction (Figure 4.6c). In such a case, more obliquely-oriented interlamellar fibers and intralamellar fibers with a radially-oriented segment might be recruited in protecting the tissue from delamination. This is in accordance with the histological studies by Sommer et al. (2008), who found that longitudinal peeling creates a remarkably "rougher" dissection surface compared to that generated by circumferential peeling. In aortic rupture, cracks tend to propagate along the direction of collagen fibers (Sugita and Matsumoto 2018). Consistently, our study also found that lower G_c is required when dissection propagates along the preferred direction of in-plane fiber distribution (circumferential peeling), as shown in Figure 4.6b. Detailed mechanical and imaging analysis is necessary in future studies to assess change of fiber architecture under transmural layer separation.

The CZM approach provides a good fit of the experimentally measured peeling force. Based on our parameter identification methodology, two model parameters, G_c and

δ_0, were obtained directly from experiment. As discussed earlier, G_c is the measured energy release rate from the peeling test. In the bilinear CZM adopted in this study, damage initiation is defined as the point beyond which irreversible mechanical failure occurs. Figure 4.4a shows how δ_0 was determined. The oscillation of the peeling force/width-displacement curve can be attributed to discrete microstructural failure events. The ramp up the peeling force is resulted from recruitment of fibers into the interlamellar direction and thus increasing of local interlamellar stiffness. Meanwhile, the displacement increments (Δd) associated with each force ramp up are due to recruitment of new interlamellar elastin and collagen fibers, while the subsequent force drop indicates failure of microstructural constituents (Yu et al. 2020). Therefore, fiber-level failure can be related to dissection propagation at the tissue-level, and the median value from the distribution of Δd was taken as the separation distance at damage initiation (δ_0) for the CZM. The only free parameter to be estimated from the simulation is t_0, traction at damage initiation. This increases the robustness and accuracy of the CZM as the delamination simulation depends largely on appropriate selection of material parameters and mesh size. To determine t_0 (Table 4.2), it is worth mentioning that t_0 should be large enough to maintain the effective stiffness of the whole laminated structure in the thickness direction, but also small enough to avoid spurious oscillations of the traction in an element (Schellekens and De Borst 1993; Turon et al. 2007). Also, appropriate application of the CZM requires a minimum number of layers of cohesive elements (3-5) in the damaged zone (Turon et al. 2007), i.e., the region from the delamination tip (where traction is zero) to the cohesion zone tip (where traction reaches t_0). In our model, there

were approximately 9 layers of cohesive elements spanning the damaged zone (Figure 4.2e). Thus the accuracy and fidelity of the entire CZM is ensured.

It is important to note that t_0 and δ_0 are not independent in the triangular traction-separation law. Based on the estimated δ_0, t_0 determined from our study agrees with previous experimental findings, which suggest our estimation of δ_0 is reasonable. From our study, the interlamellar strength of aortic media, t_0, were estimated to be 60 kPa in circumferentially peeled samples and 95 kPa in longitudinally peeled samples, respectively (Figure 4.8d). These values agree well with experimental data in the literature obtained using pressurization (Carson and Roach 1990; Tiessen and Roach 1993; Tam et al. 1998) and direct tension (Sommer et al. 2008; Tong et al. 2011) methods, which ranges from 25 to 150 kPa. The much higher value of t_0 (440 kPa) reported in the study by Leng et al. (Leng et al. 2018) is mostly associated with the skewed nonlinear CZM model adopted in their study. Based on t_0, the calculated separation distances at complete delamination (δ_c) of the CZM in Figure 4.8f are also comparable to the displacement of the primary dissection phase (~3 mm) obtained from direct tension tests (Sommer et al. 2008), which provides additional support for the estimation of δ_0 in this study. Since δ_c is actually smaller than the false lumen diameter observed clinically (Blount and Hagspiel 2009), complete failure of structural components in the interlamellar bonding along the dissection path can be expected for *in vivo* circumstances.

Among modeling studies of arterial tissue failure using various forms of the CZM (Gasser and Holzapfel 2006; Ferrara and Pandolfi 2008, 2010; Pal et al. 2014; Leng et al.

2015, 2016, 2018; Merei et al. 2017; Wang et al. 2017), the elastic properties of the CZM prior to damage initiation have received little attention. Because of the waviness of ECM fibers (Chow et al. 2014), an elastic regime may exist in the interlamellar space prior to damage initiation. From the high frequency oscillation of the experimental peeling force/width-displacement curves, the separation distance at damage initiation (δ_0) was determined to be 80 μm for aortic media (Figure 4.8c). Since average interlamellar distance in the arterial wall of adult mammals was found to be ~15 μm (Wolinsky and Glagov 1967), our research suggests that the medial interlamellar bonding has a failure strain of approximately 500 % when subjected to normal transmural pressure.

The separation distances at complete delamination (δ_c) of elastin are close to those of the intact aortic media (Figures. 4.8f and 4.9). Depleting collagen from the tissue did not induce a noticeable decrease in δ_c (Figure 4.8f), but reduced the distance at damage initiation (δ_0) by 50% (Figure 4.8c). This suggests that interlamellar elastin and collagen fibers sustain the transmural load in parallel. In fact, collagen fibers provide additional protection to the interlamellar bonding in general by prolonging the elastic regime. The presence of collagen fibers increases the separation distance at damage initiation, or the interlamellar failure strain. The tissue-level interlamellar strength (t_0 in the CZM) of arterial elastin was estimated to be 9 kPa from the circumferential peeling model and 14 kPa from the longitudinal peeling model. These values are within the range of physiological blood pressure. Furthermore, the pressure at the entry site of the false lumen is the same as that in the true lumen (Zhang et al. 2014). Taken together, this suggests that damage may first occur in elastin when blood flow enters the false lumen.

Although collagen plays a dominant role in contributing to the dissection behavior, the contribution of elastin to interlamellar bonding in the arterial wall should not be neglected. Gradual degradation of elastin results in tissue dilation and complex changes of tissue mechanical properties (Chow et al. 2013a, b). Significantly lower resistance to delamination was found in aneurysmal human ascending thoracic aortas compared with healthy tissues (Pasta et al. 2012). Because elastic fibers are prestretched and impart an intrinsic compressive stress on collagen (Chow et al. 2014), loss of interlamellar elastin not only leads to stress concentration among the remaining fibers, but also reduces the waviness of collagen (Zeinali-Davarani et al. 2013) and thus its load bearing capacity.

4.5 Limitations

The damage mechanisms in arterial tissue delamination are complex at the microscopic scale. In addition to elastin and collagen, previous studies suggested that excessive pooling of negatively charged glycosaminoglycans (GAGs) within the media leads to significant stress concentration and Donnan swelling pressure which may be an initiation factor for arterial dissection (Roccabianca et al. 2014a, b). Recent studies in our group also demonstrated the structural role of GAGs in regulating fiber recruitment when the arterial wall is subjected to in-plane biaxial tension (Mattson et al. 2017). Hence structural, electrochemical and biological analysis of various microscopic constituents and their interactions in relation to arterial dissection is necessary for a thorough knowledge of the disease.

The separation distance at damage initiation (δ_0) was obtained from peeling force oscillations. A small enough sampling interval is essential to such measurements. In this study a sampling interval of 0.04 mm was used. Future studies may consider an improved experimental setup allowing smaller sampling intervals. Additionally, the bilinear CZM is an idealized phenomenological model that may not depict the traction-separation relation during failure of fibrous biological tissues. However, the exact relationship of interlamellar traction-separation of the arterial wall is unknown. A recent study (Yu et al. 2020) showed that aortic dissection propagates in avalanches, which may suggest that the onset of strain softening follows closely the point of damage initiation.

Blood vessels are subjected to much more complicated loading *in vivo*. Pulsatile blood flow-induced wall shear stresses in the false lumen of dissected arteries can give rise to displacement in the direction of the flow. On the other hand, due to the anisotropic and inhomogeneous nature of the vessel wall (Yu et al. 2018a, b), torsion-induced shear stress can also be sufficiently large to overcome the adhesive bonding (Rajagopal et al. 2007). Given that propagation of dissection is principally driven by hemodynamic cyclic/pulsatile loading (Rajagopal et al. 2007), for a comprehensive understanding of dissection propagation in more realistic situations, further experimental testing using different loading rates and delamination modes is needed to construct mixed-mode CZM to characterize the interlamellar mechanical properties of the arterial wall.

4.6 Conclusions

We studied the contribution of elastin and collagen fibers to the interlamellar bonding properties in porcine arterial wall through peeling test coupled with 3D finite element modeling. An effort was made to relate the microscopic failure characteristics from the peeling force/width-displacement data to the model parameters in the CZM. Damage is initiated in the arterial wall at a small interlamellar separation distance of 80 μm for the media and 40 μm for elastin network, while complete delamination requires a relatively large separation distance up to 3 – 4 mm. Our study suggests that interlamellar elastin and collagen fibers sustain the transmural load in parallel, however damage may first occur in elastin when blood flow enters the false lumen. Therapeutic intervention is essential at this stage to prevent further propagation of the damage. Once an increase greater than 3 mm in the lamellar distance occurs, detection and repair of a local blood-filled cavity with complete failure of interlamellar fibers is required to avoid catastrophic rupture. Collagen was found to play a dominant role in providing the elastic regime, and in contributing to stiffness (K), strength (t_0) and toughness (G_c) of the interlamellar bonding of aorta. Multiphoton imaging reveals the structural role of elastin and collagen in resisting delamination, as well as indicates a possible mechanism of in-plane anisotropy of elastin and collagen in determining the direction-dependent phenomena noticed in peeling tests. Findings of this study can provide structural-based indicators for the risk assessment and prevention of aortic dissection. Future studies considering the effects of loading rates as well as mixed-mode delamination of arterial tissue failure are needed for further understanding of the relationship between the integrity of microscopic interlamellar constituents and the initiation and progression of arterial dissection.

CHAPTER 5 EFFECT OF GLYCATION ON INTERLAMELLAR BONDING OF ARTERIAL ELASTIN

5.1 Overview

Interlamellar bonding in the arterial wall is often compromised by cardiovascular diseases. However, several recent nationwide and hospital-based studies have uniformly reported reduced risk of thoracic aortic dissection in patients with diabetes. As one of the primary structural constituents in the arterial wall, elastin plays an important role in providing its interlamellar structural integrity. The purpose of this study is to examine the effects of glycation on the interlamellar bonding properties of arterial elastin. Purified elastin network was isolated from porcine descending thoracic aorta and incubated in 2 M glucose solution for 7, 14 or 21 days at 37 °C. Peeling and direct tension tests were performed to provide complimentary information on understanding the interlamellar layer separation properties of elastin network with glycation effect. Peeling tests were simulated using a cohesive zone model (CZM). Multiphoton imaging was used to visualize the interlamellar elastin fibers in samples subjected to peeling and direct tension. Peeling and direct tension tests show that interlamellar energy release rate and strength both increases with the duration of glucose treatment. The traction at damage initiation estimated for the CZM agrees well with the interlamellar strength measurements from direct tension tests. Glycation was also found to increase the interlamellar failure strain of arterial elastin. Multiphoton imaging confirmed the contribution of radially running elastin fibers to resisting dissection. It was found that nonenzymatic glycation reduces the propensity of arterial elastin to dissection. This study

also suggests that the CZM effectively describes the interlamellar bonding properties of arterial elastin.

5.2 Introduction

Elastin is one of the major load bearing extracellular matrix (ECM) constituents in the arterial wall that is subjected to billions of cycles of deformation over the lifetime of an individual (Kielty et al. 2002). It not only provides the tissue with in-plane elastic properties, but also plays a protective role in maintaining the structural integrity and resisting damage propagation in the aorta (Avolio et al. 1998; Pasta et al. 2012; Clark et al. 2015; Noble et al. 2016; Wang et al. 2020). Elastic fibers are composed of an amorphous elastin core making up 90% of the mature fiber, and peripherally located microfibrils (Rosenbloom et al. 1993). As an essential structural constituent in the medial layer of the arterial wall, elastic fibers form a three-dimensional (3D) network structure with concentric elastic lamellar layers and interlamellar radially running fibers (Wolinsky and Glagov 1964, 1967). Scanning electron microscopy imaging revealed that elastic lamellae comprised 71% of the total volume of elastic fibers, while 27% of elastic fibers are organized into chords or wisps that protrude obliquely from lamellar surfaces and terminate in the adjacent interlamellar space. The remaining 2% of elastic fibers form thick struts connecting adjacent lamellae (O'Connell et al. 2008). Researchers including us have quantitatively examined the contribution of medial elastin to interlamellar bonding in porcine aorta (Noble et al. 2016; Wang et al. 2020).

Aortic dissection is a devastating disease with a high mortality rate (Spittell et al.

1993; Hagan et al. 2000; Khan and Nair 2002). The mechanopathology of aortic dissection is a complex process which involves several distinct developmental stages including the formation of a intimal tear (Thubrikar et al. 1999); parallel propagation of delamination in the media (Carson and Roach 1990; Tam et al. 1998); and rupture of the arterial wall caused by radial propagation of damage across lamellae (Sommer et al. 2008). Previous biomechanical studies found compromised interlamellar bonding in human aorta under several cardiovascular maladies such as atherosclerosis and aneurysms (Tong et al. 2011, 2014; Pasta et al. 2012). On the contrary, multiple statistical investigations including nationwide studies in the US, Spain and Sweden (Prakash et al. 2012; Jiménez-Trujillo et al. 2016; Avdic et al. 2018), hospital-based studies in the UK and China (Theivacumar et al. 2014; He et al. 2015) as well as a meta-analysis of online databases (Takagi and Umemoto 2017) have uniformly reported lower risk of aortic dissection in patients with diabetes mellitus. In addition, a recent study found that Type 2 diabetes mellitus reduces mortality and clinical complications in aortic dissection patients after thoracic endovascular aortic repair (Liu et al. 2019).

Diabetes has been found to be closely associated with cardiovascular disease progression and vascular remodeling (Brownlee et al. 1988; Sowers et al. 2001). Nonenzymatic glycation, the reaction between glucose and the ECM proteins, is magnified in diabetic patients (Wolff et al. 1991). It is one of the main mechanisms of aging of the long-lived ECM protein, and has been shown to correlate with the severity of diabetic complications (Vishwanath et al.1986; Vlassara et al. 1986), and to accelerate the age associated stiffening of arteries in diabetic patients (Cameron et al. 2003). As a

structural protein with a long half-live, elastin is especially susceptible to the slow glycation process (Konova et al. 2004). Arterial elastin was shown to exhibit higher stiffness and become more viscous with glucose exposure (Winlove et al. 1996; Zou and Zhang 2012b; Wang et al. 2015, 2018b). The nonenzymatic glycation between glucose and amino groups on proteins results in the formation of advanced glycation end-products (AGEs) that accumulate on proteins. Earlier stiffening of the arterial wall among diabetic patients has been attributed to increased crosslinking in glycated proteins (Sims et al. 1996). Structural studies suggested glucose promotes structural rearrangement and aggregation of elastin molecule (De et al. 2020); and more rigid backbone structures and conformational changes were observed in glucose exposed elastin (Silverstein et al. 2015). However, the effect of glycation on the interlamellar bonding properties of arterial elastin is not well understood.

In this study, we investigated the change of interlamellar bonding properties of arterial elastin with *in vitro* glucose treatment. Peeling tests and direct tension tests were carried out on porcine elastin samples with varying duration of glucose exposure, and the interlamellar energy release rate and bonding strength were quantified and compared. Untreated samples and samples treated with 1× phosphate buffered saline (PBS) for 21 days at 37 °C were also tested for comparison. A finite element model based on cohesive zone theory of fracture (Dugdale 1960; Barenblatt 1962) was created to describe the delamination behavior during the peeling process. The dissection sites in peeling and direct tension tests were imaged using multiphoton microscopy to visualize interlamellar elastin fibers.

5.3 Material and Methods

5.3.1 Sample preparation

Porcine thoracic aortas were harvested from a local abattoir and delivered to laboratory on ice. For peeling tests, the aortas were cut into circumferential and longitudinal rectangular strips of about 40 mm × 10 mm. For direct tension tests, the aortas were cut into small patches for further preparation. Purified elastin network was obtained using a cyanogen bromide (CNBr) treatment method (Zou and Zhang 2009). Samples were then incubated in 2 M glucose solution and were allowed to equilibrate at 37 ℃ for 7, 14 or 21 days (Zou and Zhang 2012b; Wang et al. 2015). Elastin samples without any treatment were also tested and served as a control. Apart from the glucose-treated and untreated control samples, one group of elastin samples were incubated in 1× PBS solution at 37 ℃ for 21 days and served as an additional control group. 100 units/ml penicillin/streptomycin was added as an antibiotic and antifungal treatment to the group treated in PBS for 21 days (Smart et al. 1996). No antibiotic or antifungal treatment was used in the glucose solutions as the solution was found to be clear after 21 days of treatment time.

5.3.2 Peeling test

Refer to Section 2.3 for a more comprehensive description of the experimental protocol. A schematic of the experimental setup is shown in Figure 5.1a. The two tongues were glued to sandpaper tabs and gripped by the tester. One tongue of the sample was

fixed while the other tongue was pulled away at an extension rate of 0.2 mm/s. The displacement of the moving side as well as the peeling force were recorded at a frequency of 5 Hz until complete separation. Samples were submerged in glucose (glucose-treated groups) or PBS (PBS-treated and control groups) solution under room temperature during experiments. There were 6-9 successfully tested samples within each group. The energy release rate, G_c, can be calculated using Equation 2.2. G_c can also be interpreted as interlamellar toughness, i.e., the energy required to split a unit area of the interface (Kendall 1975; Parmigiani and Thouless 2006).

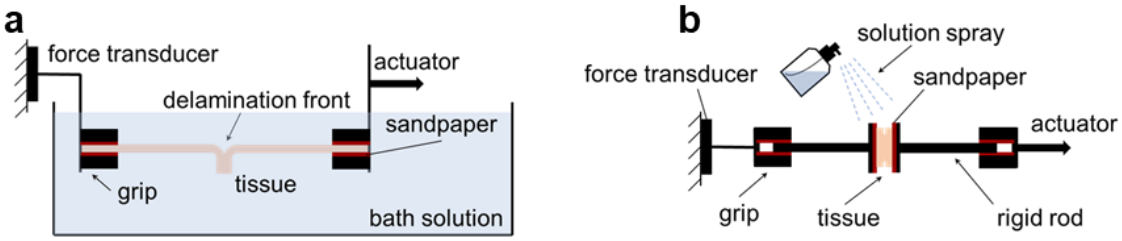

Figure 5.1 Schematic of the experimental setup for a peeling and b direct tension tests.

5.3.3 Direct tension test

Refer to Chapter 2.4 for a more detailed description of this experiment. Briefly, direct tension tests were performed by mounting the two end surfaces of the sample on a uniaxial tensile tester and stretching the sample along its radial direction until complete separation (Sommer et al., 2008). A schematic of the experimental setup is shown in Figure 5.1b. Before the testing started, the sample was moisturized with glucose (glucose-treated groups) or PBS (PBS-treated and control groups) spray at room

temperature. The moving rod was then pulled away at an extension rate of 0.02 mm/s. The displacement of the moving rod as well as the reaction force was recorded at a frequency of 5 Hz. There were 7-8 successfully tested samples within each group. The interlamellar strength, t_{DT}, was obtained by dividing the maximum reaction force prior to the damage onset point by the initial effective bonding area as demonstrated by Equation 2.3.

5.3.4 Statistical analysis

Peeling force (F), energy release rate (G_c) and interlamellar strength (t_{DT}) data were summarized as mean ± standard deviation. Two-tailed unpaired t-tests were performed on these data. Specifically, the untreated control group was compared to the glucose treated groups at 7, 14 and 21 days. The 21 days PBS treated additional control group was compared to the untreated control group as well as the 21 days glucose treated group. The t-tests were also performed to compare samples with different glucose treatment time. In addition, two-tailed unpaired t-tests were applied to compare the displacement increments, Δd, associated with each ramp up of the oscillated peeling force, of the untreated control group with glucose treated groups. $p < 0.05$ is considered as statistically significant.

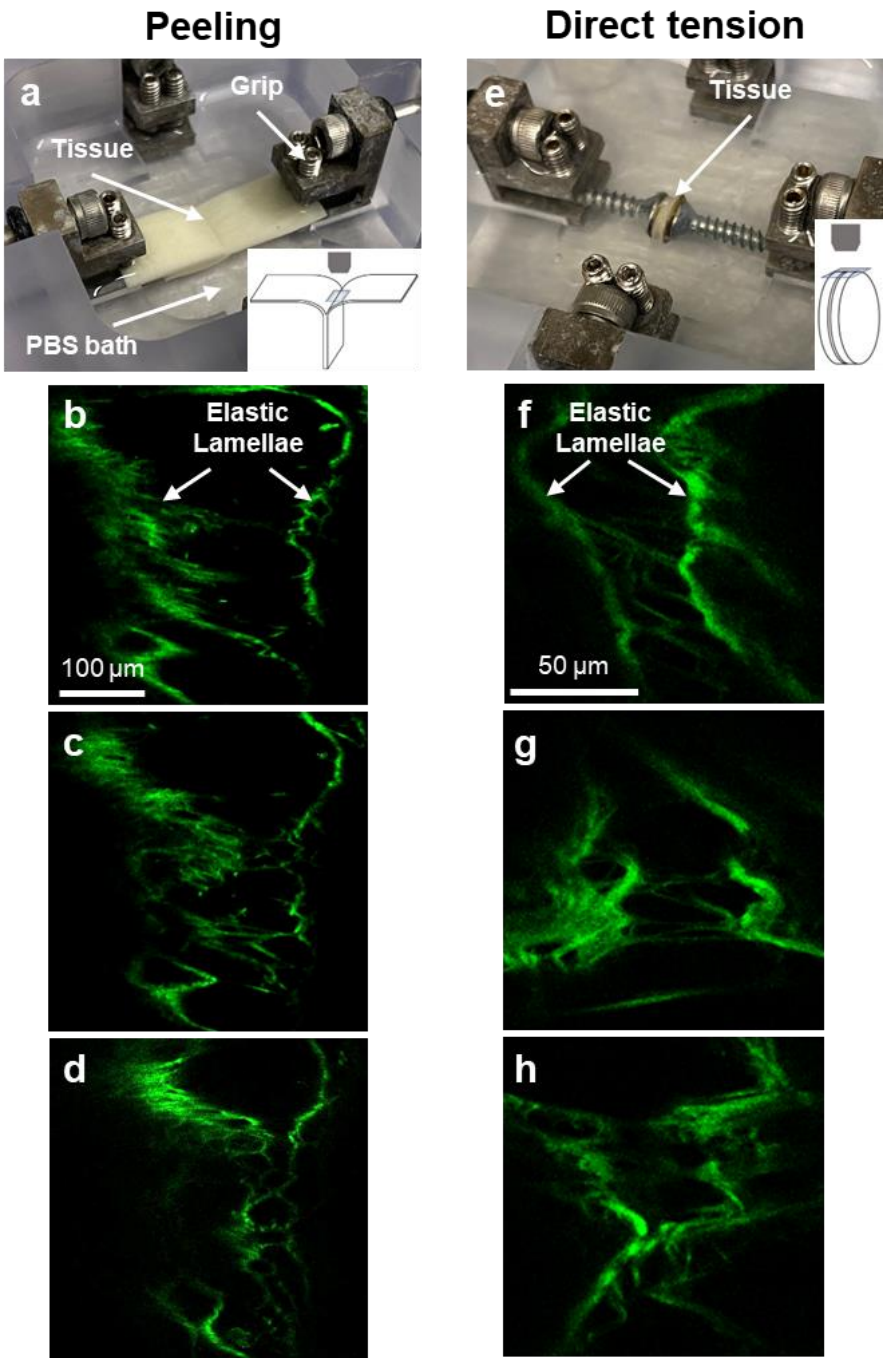

Figure 5.2 Custom-built device for multiphoton imaging of the separation site (inset pictures) of arterial elastin during a peeling and e direct tension tests; b-d multiphoton images of the dissection site in peeling of a circumferential porcine arterial elastin strip at different imaging depths (imaging depth increases from b to d); and f-h multiphoton images of different sub-locations of the separation site in direct tension of porcine arterial elastin.

5.3.5 Multiphoton imaging

Multiphoton imaging was performed to visualize the separation site of elastin network during peeling and direct tension tests. An inverted multiphoton microscopy system (Carl Zeiss LSM 710 NLO) was used to generate two-photon excited fluorescence (2PEF) from elastin (525/45 nm) (Chow et al. 2014; Yu et al. 2018a, b). The excitation wavelength of the femtosecond IR pulse laser was set to be 810 nm. The laser scanning system was coupled with a 20× water immersion objective lens. Samples were prepared following the same protocols for mechanical testing as described in Sections 2.2.1 and 2.2.2. Samples were then mounted on a custom-built device, stretched manually to expose the interlamellar fibers and imaged at the separation site (Figures 5.2a and 5.2e). For imaging of peeling samples, the two tongues of the sample were gripped and stretched apart so that the dissection forefront was exposed under the lens (Figure 5.2a). For imaging of direct tension samples, a stretch of about 2 mm was applied on the sample to expand the initial incision and straighten the interlamellar fibers; the lens was then placed above the incision (Figure 5.2e). Stack images of about 50 μm in depth with a field of view of 425 μm × 425 μm were acquired at the dissection site.

5.3.6 Finite element modeling of peeling test

To gain insights into the interlamellar bonding properties of arterial elastin with glycation effect, 3D finite element models of peeling tests were created in ABAQUS (version 6.14, Simulia, Providence, RI) following the modeling and parameters identification protocols described in our previous study (Wang et al. 2020). Briefly,

rectangular strips with two originally separated “tongues” were modeled and meshed with 8-node brick elements (C3D8). The thickness of the strips was obtained from averaged experimental measurements. Cohesive elements (COH3D8) were sandwiched between the two strips. The size of cohesive elements along the direction of dissection propagation was chosen to be 0.2 mm after a mesh size dependency study. During peeling, the reaction force as well as the displacement at the end of the “tongues” were extracted and compared with experimental data.

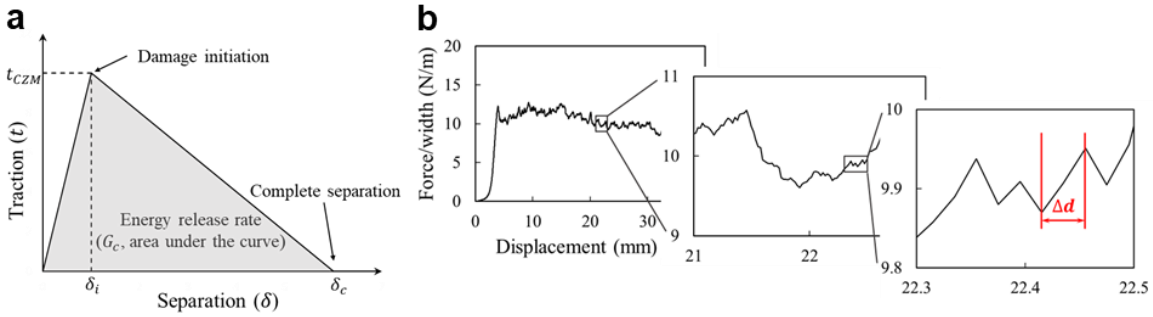

Figure 5.3 a Bilinear traction-separation law for the cohesive zone model; and b a representative peeling force/width-displacement curve and its zoom-in graphs showing the high frequency oscillation of the peeling force and the displacement increment ($\Delta \boldsymbol{d}$) associated with a ramp up of the peeling force.

A bilinear traction-separation relation shown in Figure 5.3a was used to describe the CZM for peeling tests. Detailed description of the approach can be found in our previous study (Wang et al. 2020). Briefly, to fully characterize the bilinear traction-separation relation of the CZM, three independent parameters need to be identified: traction at damage initiation t_{CZM}, separation distance at damage initiation δ_i, as well as energy release rate G_c, which equals the area under the curve (Figure 5.3a) and can be

determined directly from the experimental data within each sample group. Damage initiation is defined as the point beyond which irreversible damage occurs. Figure 5.3b shows a representative peeling force-displacement curve obtained from experiments. To determine the separation distance at damage initiation, the displacement increments, Δd, associated with each ramp up of the peeling force, were collected from all samples within each sample group (Figure 5.3b), of which the median value was taken as the separation distance at damage initiation δ_i in the CZM. Finally, the traction at damage initiation t_{CZM}, was adjusted to fit the simulated peeling force to averaged experimental measurements. t_{CZM} is the maximum elastic stress interlamellar bonding can sustain before failure occurs, or the interlamellar strength. Once G_c, δ_i and t_{CZM} were identified, the separation distance at complete delamination (δ_c) can be calculated as $\delta_c = 2G_c/t_{CZM}$.

The mean absolute percentage error (MAPE) between simulated results and experimental data is defined as

$$MAPE = \frac{1}{n}\sum_{i=1}^{n}\left|\frac{F_{sim,i}-F_{exp}}{F_{exp}}\right| \quad (5.1)$$

where $F_{sim,i}$ is the ith peeling force data obtained from simulation and F_{exp} is the averaged value of peeling force from experiments. n is the total number of data points. Because of the built-in numerical oscillations of the simulated reaction peeling force caused by Gaussian integration scheme (Schellekens and De Borst 1993), the fitting was considered acceptable when MAPE was smaller than 5%.

5.3.7 Constitutive modeling of elastin network

An anisotropic hyperelastic strain energy density function (Holzapfel et al. 2000; Gasser et al. 2006) was adopted to describe the in-plane behavior of arterial elastin:

$$W = \frac{C_{10}}{2}(\bar{I}_1 - 3) + \frac{k_1}{2k_2}\sum_{i=1,2}\{exp[k_2\langle\bar{E}_i\rangle^2] - 1\} + \frac{1}{D}\left(\frac{J^2-1}{2} - \ln J\right) \quad (5.2)$$

where $\bar{I}_1$ is the first deviatoric strain invariant. C_{10} and k_1 are stress like parameters for the ground substance and fibers. k_2 is a dimensionless parameter which governs the nonlinearity of fibers at large strain. $\bar{E}_i = \kappa(\bar{I}_1 - 3) + ((1 - 3\kappa)\bar{I}_{4i} - 1)$ characterizes the deformation of the ith fiber family, in which κ is the dispersion parameter ($0 \leq \kappa \leq 1/3$), and $\bar{I}_{4i}$ is the square of stretch along the mean direction of the ith fiber family. θ is the angle between the mean fiber direction and the longitudinal direction of the aorta. $1/D$ is bulk modulus and serves as a penalty parameter for preventing volumetric locking in the finite element simulations (Holzapfel et al. 2002). In this study $1/D$ was set to be 1000 kPa. J is the determinant of Jacobian matrix. For nearly incompressible materials, J is close to 1 (Chen et al. 1997). Other model parameters for untreated and treated arterial elastin were determined by fitting simulated Cauchy stress-stretch curves to the averaged experimental testing data published previously (Wang et al. 2015). The constitutive model was implemented in MATLAB (version R2019a, The MathWorks, Inc., Natick, MA). Parameters C_{10}, k_1 and k_2 were set to be greater than zero, and κ varied between 0 and 1/3. Parameters were estimated by minimizing the objective function:

$$\psi = \frac{1}{m}\sum_{j=1}^{m}\left[(\sigma_{11}^c - \sigma_{11}^e)_j^{\,2} + (\sigma_{22}^c - \sigma_{22}^e)_j^{\,2}\right] \quad (5.3)$$

where m is the number of data points. σ^c and σ^e are Cauchy stress from the constitutive model and averaged experimental data, respectively. The *fminsearch* function in MATLAB with embedded Nelder-Mead direct search method was used to minimize the objective function with a tolerances of 1×10^{-8}. Estimated parameters and the value of the objective function are listed in Table 5.1.

Table 5.1 Material parameters for the constitutive model of arterial elastin in Equation 5.2 for the untreated and glucose treated elastin, and the value of the objective function in Equation 5.3.

	C_{10} (kPa)	k_1 (kPa)	k_2	κ	θ	ψ (kPa^2)
Untreated	8.24	330.48	0.12	0.208	43.61	0.66
Day 7	10.55	386.66	0.10	0.168	44.41	0.50
Day 14	12.68	427.93	0.08	0.177	44.20	2.32
Day 21	14.56	490.31	0.06	0.174	44.39	6.40

5.4 Results

Figure 5.4 shows the experimental curves of peeling force versus displacement of elastin samples in the circumferential and longitudinal directions. The peeling force increases with stretching of the two tongues and plateaus as delamination starts to propagate in the bonded tissue. Table 5.2 reports the mean and standard deviation of F and G_c. Figure 5.5 shows the whisker plots of F and G_c together with individual sample data points. Compared with untreated samples, both F and G_c increase drastically after the first week of glucose exposure. The mean value of F increases by 38.02% in the

circumferential direction (p=0.00003) and 24.89% in the longitudinal direction (p=0.057); the mean value of G_c increases by 37.20% in the circumferential direction (p=0.00004) and 25.87% in the longitudinal direction (p=0.066), followed by a continuous and gradual rise up to 21 days in the glucose solution (Figure 5.5). Statistical analysis shows that significant difference of F and G_c appears after 7 days of glycation effects in the circumferential direction (Figures 5.5a and 5.5c); however, in the longitudinal direction, significant difference of F appears after 21 days (p=0.047) of glycation effects and no significant difference was found in G_c (p=0.066) (Figures 5.5b and 5.5d). No significant difference in F or G_c was found between different groups with different glucose treatment times. Also, glucose treatment has little effect on the direction-dependence of F and G_c, as it can be seen that peeling along the longitudinal direction always exhibits higher F and G_c as well as a larger variation than the circumferential direction (Figures 5.5a-d). No significant difference of F (Circ: p=0.15; Long: p=0.48) or G_c (Circ: p=0.11; Long: p=0.47) was found between the untreated and 21 days PBS treated groups (Figures 5.5a-d). On the other hand, significant difference in F (Circ: p=0.0.0004; Long: p=0.025) and G_c (Circ: p=0.0003; Long: p=0.034) was found between the 21 days glucose treated group and 21 days PBS treated group.

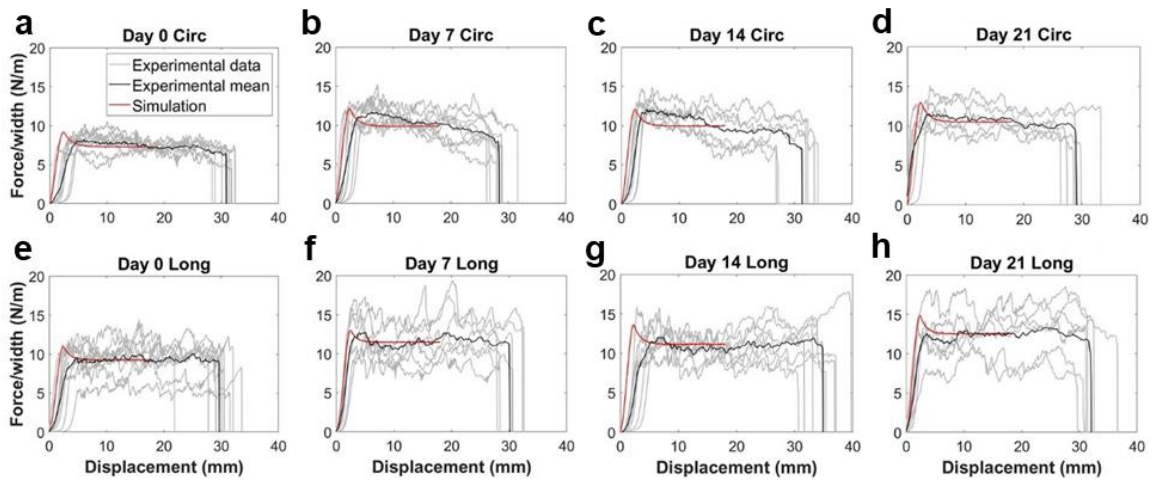

Figure 5.4 Experimental and simulated curves of peeling force/width vs. displacement from peeling of arterial elastin in the circumferential (Circ) and longitudinal (Long) directions before (a and e) and after (b-d and f-h) glucose treatment.

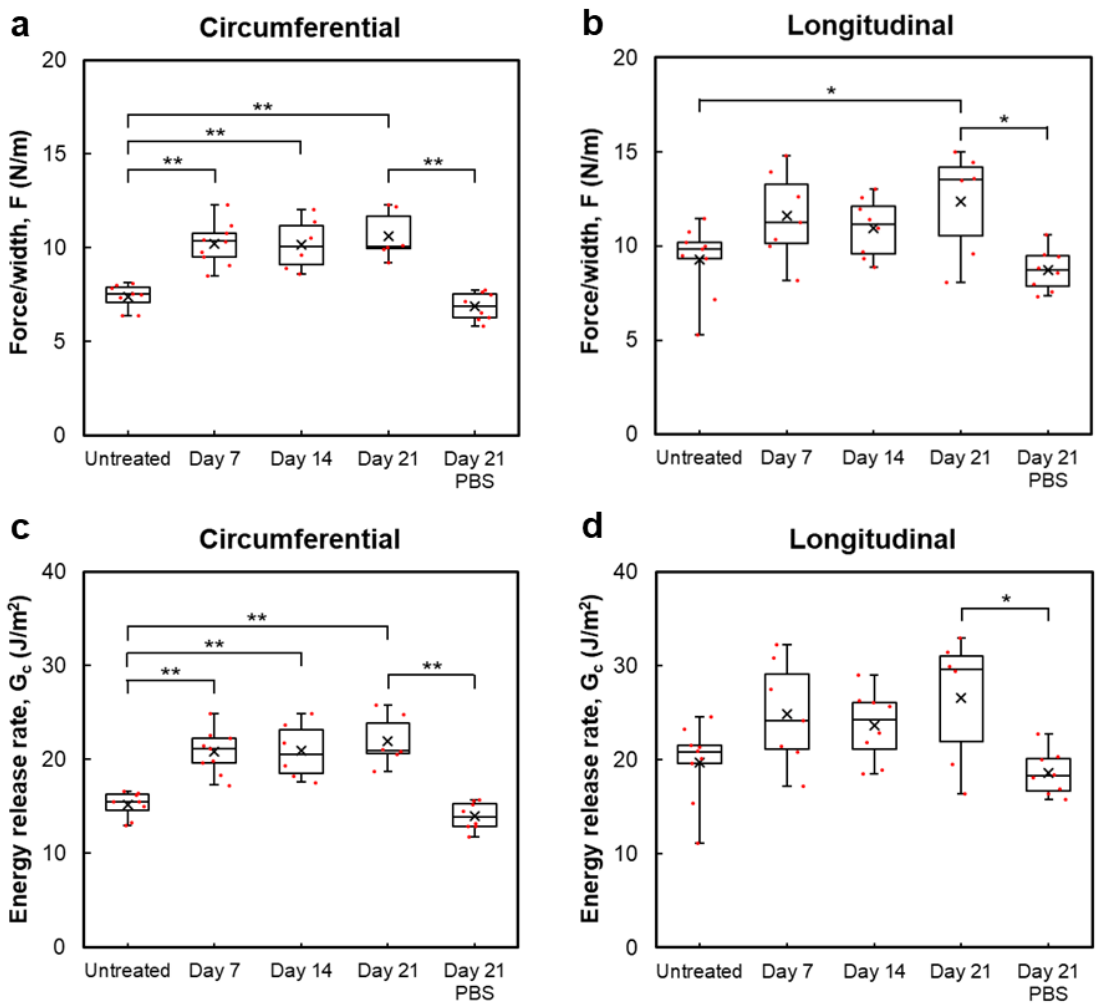

Figure 5.5 a and b peeling force per unit tissue width ($\boldsymbol{F}$); and c and d energy release rate ($\boldsymbol{G_c}$) of arterial elastin for untreated, glucose treated (7, 14, and 21 days), and PBS treated (21days) in the circumferential and longitudinal directions. The box represents the middle 50% (from the first quartile to the third quartile) of the data set; the horizontal line inside the box represents the median; the cross symbol represents the mean; the red dots represent individual data points. ($^{*}p<0.05$, $^{**}p<0.01$).

Table 5.2 Experimental results of peeling force ($\boldsymbol{F}$), energy release rate ($\boldsymbol{G_c}$) from peeling test; and interlamellar strength ($\boldsymbol{t_{DT}}$) from direct tension test (Circ: circumferential; Long: longitudinal).

	Untreated	Day 7	Day 14	Day 21	Day 21 PBS
			Force, F (N/m)		
Circ	7.39 ± 0.68	10.20 ± 1.14	10.18 ± 1.37	10.62 ± 1.29	6.85 ± 0.74
Long	9.28 ± 1.90	11.59 ± 2.34	10.98 ± 1.54	12.35 ± 2.82	8.73 ± 1.10
			Energy release rate, G_c (J/m^2)		
Circ	15.19 ± 1.38	20.84 ± 2.34	20.90 ± 3.00	21.98 ± 2.71	13.97 ± 1.49
Long	19.75 ± 4.13	24.86 ± 5.55	23.63 ± 3.75	26.56 ± 6.89	18.56 ± 2.34
			Interlamellar strength, t_{DT} (kPa)		
	11.28 ± 2.72	15.27 ± 4.45	15.53 ± 3.17	16.79 ± 2.30	10.56 ± 2.21

Table 5.3 Material parameters for the CZM of arterial elastin before and after glucose treatment. (Circ: circumferential; Long: longitudinal; $\boldsymbol{G_c}$: energy release rate; $\boldsymbol{\delta_i}$: separation distance at damage initiation; $\boldsymbol{t_{CZM}}$: traction at damage initiation; $\boldsymbol{\delta_c}$: separation distance at complete delamination; MAPE: mean absolute percentage error).

		Parameters obtained from experiments		Parameters obtained from the model		
		G_c (J/m^2)	δ_i (mm)	t_{CZM} (kPa)	δ_c (mm)	MAPE
Untreated	Circ	15.19	0.08	9	3.38	1.2%
	Long	19.75	0.08	13	3.04	0.4%
Day 7	Circ	20.84	0.08	13	3.21	2.8%
	Long	24.86	0.12	17	2.92	0.8%
Day 14	Circ	20.90	0.16	13	3.22	2.1%
	Long	23.63	0.24	17	2.78	1.6%
Day 21	Circ	21.98	0.16	14	3.14	1.1%
	Long	26.56	0.12	18	2.95	1.5%

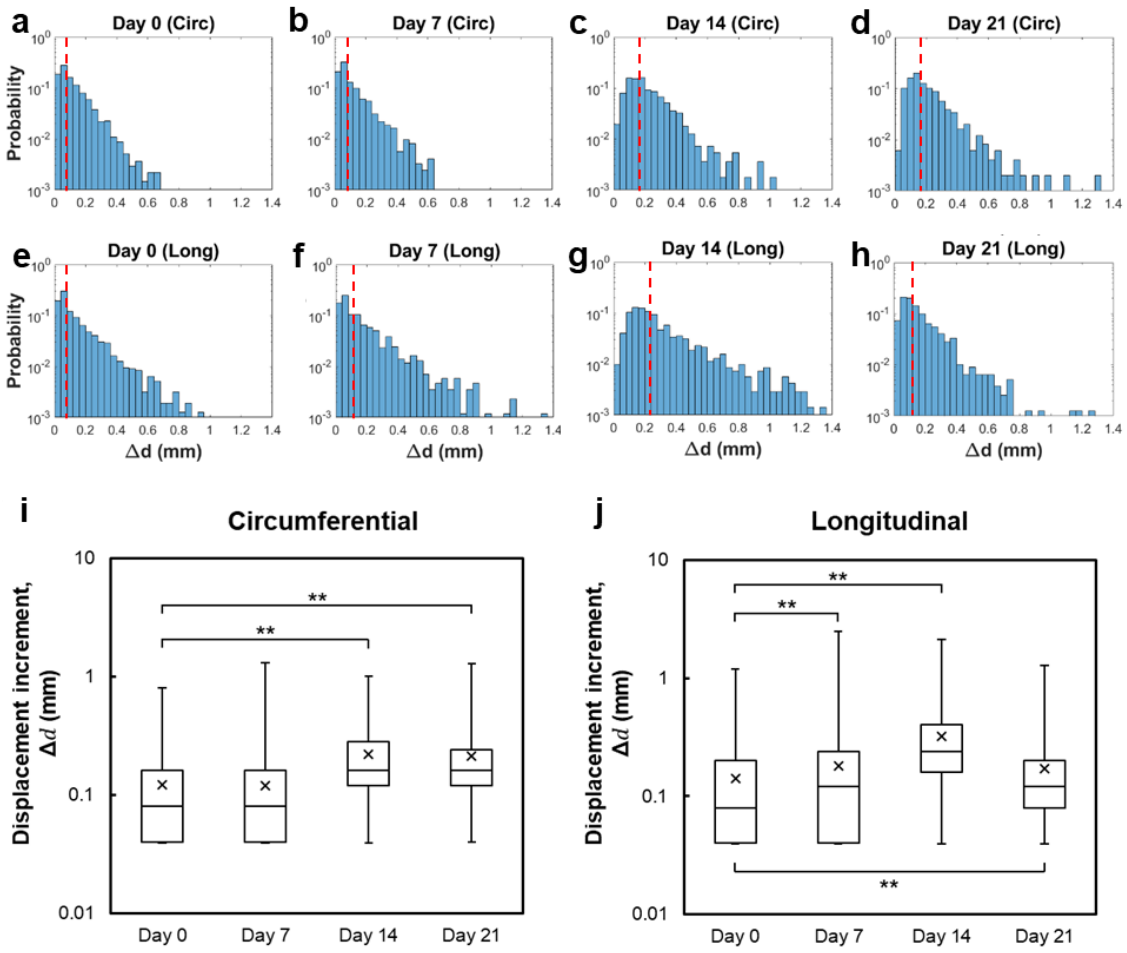

Figure 5.6 Probability distribution of the displacement increment ($\boldsymbol{\Delta d}$) associated with each ramp up of the peeling force from peeling tests of arterial elastin in the a-d circumferential (Circ) and e-h longitudinal (Long) directions before and after glucose treatment; and whisker plots of the distribution of $\boldsymbol{\Delta d}$ with varying durations of glucose treatment in the i circumferential and j longitudinal directions. The box in the whisker plots represents the middle 50% (from the first quartile to the third quartile) of the data set; the horizontal line inside the box represents the median; the cross represents the mean; individual data points are not shown in i and j because of the large size of the data set. Red lines in a-h indicate the location of the median; note that the vertical axis in a-j are in logarithmic scale. ($^{*}p<0.05$, $^{**}p<0.01$).

Multiphoton microscopy reveals interlamellar elastin fibers. Figures 5.2b-d present multiphoton images at different depths of the separation site during peeling test. Figures 5.2f-h present multiphoton images at different sub-locations of the separation site during direct tension test of untreated arterial elastin. In the interlamellar space, two distinct elastic lamellae can be visualized with elastin fibers connecting the adjacent lamellae. Interlamellar elastin appears to be recruited and provide resistance to delamination when the tissue is under transmural tensile stresses. During peeling tests, the plateau regime of the force-displacement curves exhibits a high frequency oscillation (Figure 5.4). The displacement increments, Δd, associated with a ramp up in the peeling force were collected and reported in Figure 5.6. We can see that the median value of Δd generally increases with glucose exposure duration, except for the longitudinal direction with 21 days of glucose treatment. Overall, the median of Δd increases by 100% in the circumferential direction from 0.08 mm to 0.16 mm and 50% in the longitudinal direction from 0.12 mm to 0.16 mm after 21 days of glucose treatment (Table 5.3). Results of statistical analysis of Δd are shown in Figures 5.6i and 5.6j. Significant difference ($p<0.001$) was found between the untreated and all glucose treated groups in both the circumferential and longitudinal directions except for the comparison between the untreated and 7 days glucose treated groups in the circumferential direction ($p=0.49$).

A representative force-displacement curve obtained from direct tension test is shown in Figure 5.7a. The deformation process is consisted of an elastic deformation phase followed by a damage phase, which is marked by a rapid drop in the slope of the force-displacement curve after the initial increase of the reaction force. A peeling-like

damage mode can be identified near the end of the damage phase (Figure 5.7b), which corresponds to the plateau part of the reaction force (Figure 5.7a). Force-displacement curves of all samples before and after glucose treatment are shown in Figures 5.7c-f. The interlamellar strength (t_{DT}) extracted using Equation 2.3 is summarized in Figure 5.8. The mean and standard deviation of t_{DT} are presented in Table 5.2. Similar to the results of peeling tests, glucose exposure greatly increases interlamellar strength in the direct tension test of arterial elastin, with the most drastic increase of 35.37% occurs at day 7 (p=0.066). It appears that glucose exposure continues to take effect on t_{DT} beyond day 7, as the difference between the untreated and glucose treated samples is not significant until the samples have been incubated for 14 days (p=0.012) or longer, see Figure 5.8. No significant difference in t_{DT} was found between groups with different glucose treatment times. In addition, no significant difference was identified between the untreated and 21 days PBS treated groups (p=0.59), whereas t_{DT} of 21 days glucose treated group is significantly different from that of 21 days PBS treated group (p=0.0001).

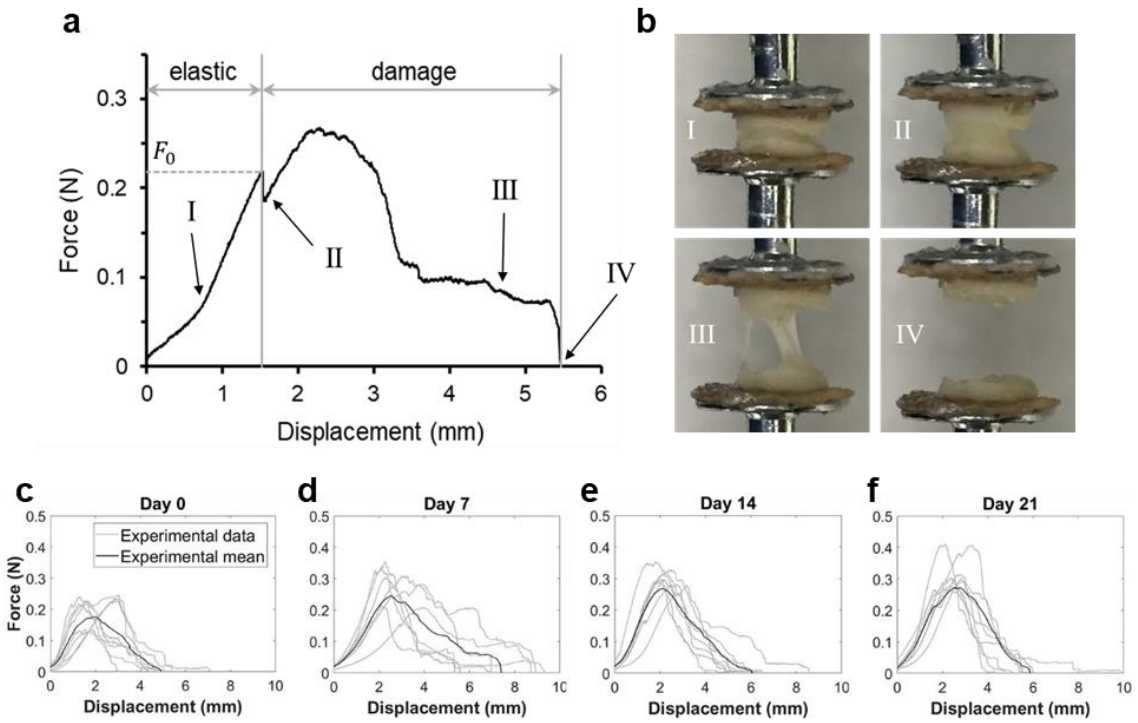

Figure 5.7 a A representative force-displacement curve obtained from the direct tension test of arterial elastin; and b pictures showing different stages of a sample during direct tension test: I elastic deformation, II damage onset, III peeling-like damage mode, and IV complete separation. c-f Force-displacement curves from direct tension tests of arterial elastin c before and d-f after glucose treatment.

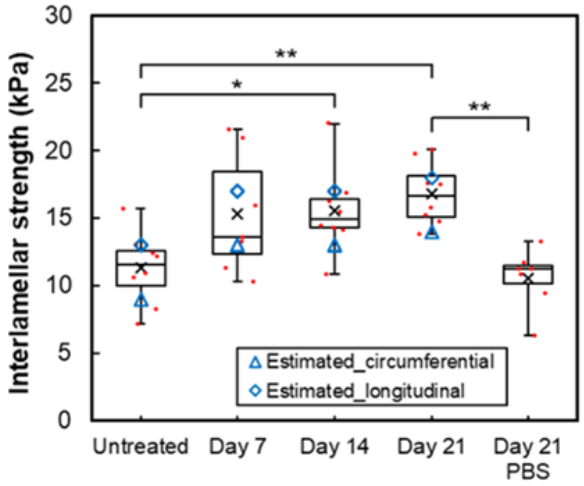

Figure 5.8 Interlamellar strength obtained from direct tension tests (t_{DT}) as well as estimated values from finite element simulations of peeling tests (t_{CZM}) for arterial elastin before and after glucose treatment. The box in the whisker plots represents the middle 50% (from the first quartile to the third quartile) of the data set; the horizontal line inside the box represents the median; the cross represents the mean; red dots represent individual data points. (*p<0.05, **p<0.01).

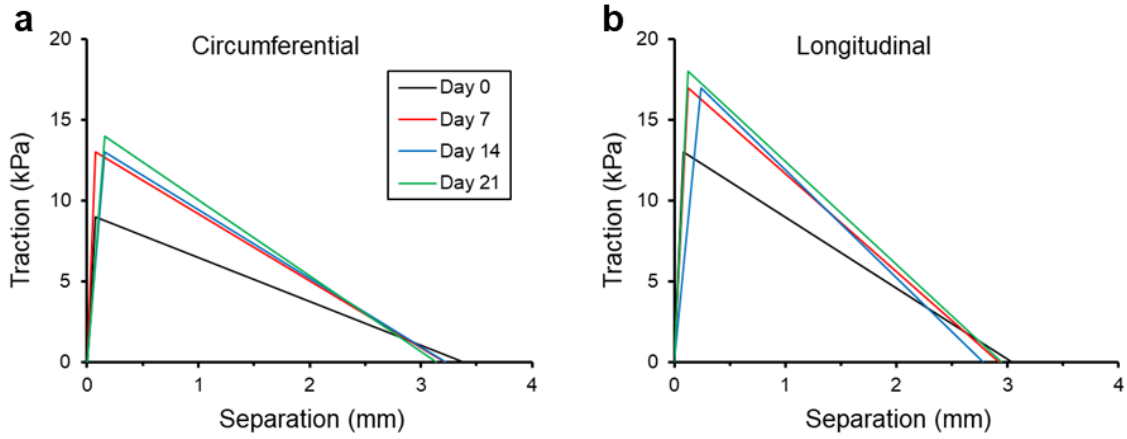

Figure 5.9 Traction-separation relations for the cohesive zone of untreated and glucose treated arterial elastin determined from peeling tests in the a circumferential and b longitudinal directions.

The interlamellar strength was also estimated using the CZM finite element model of peeling test. As shown in Figure 5.4, the simulated peeling force-displacement curves match well with corresponding experimental data. The CZM parameters identified from both peeling tests and finite element simulations are listed in Table 5.3. Figure 5.8 shows that the interlamellar strength (t_{DT}) measured from direct tension tests fell between the traction at damage initiation (t_{CZM}) estimated from the circumferential and longitudinal directions from peeling tests. The interlamellar traction-separation relations estimated for the untreated and glucose treated arterial elastin from peeling tests in the circumferential and longitudinal directions are plotted in Figure 5.9. In glucose treated groups, besides the increase of G_c and higher separation distance at damage initiation (δ_i), t_{CZM} estimated from CZM also increases with glucose exposure. However, glucose exposure has little influence on the separation distance at complete delamination (δ_c) of arterial elastin.

5.5 Discussion

Our study shows that non-enzymatic glycation has a prominent effect on the interlamellar bonding of arterial elastin. Glucose treated elastin exhibits increased peeling force, energy release rate and interlamellar strength compared with untreated samples (Figures 5.5 and 5.8). The separation distance at damage initiation (δ_i) also increases in the glucose treated samples. Together with the decreased overall sample thickness, or interlamellar spacing, our results suggest that the interlamellar failure strain increases with glycation. Therefore, glycation reduces the propensity to delamination of arterial elastin. These findings support the reported clinical evidence on inverse correlation

between diabetes and the risk of aortic dissection (Prakash et al. 2012; Theivacumar et al. 2014; He et al. 2015; Jiménez-Trujillo et al. 2016; Takagi and Umemoto 2017; Avdic et al. 2018; Liu et al. 2019; Tong et al. 2020).

Peeling and direct tension tests have been used broadly to assess the dissection properties of the arterial wall (Sommer et al. 2008; Tong et al. 2011; Pasta et al. 2012; Wang et al. 2014; Noble et al. 2016; Leng et al. 2018) and atherosclerotic plaque (Wang et al. 2011). Consistent with previous direct tension studies using human aorta (Sommer et al. 2008; Tong et al. 2011), arterial elastin samples favored a peeling-like damage mode towards the end of the damage phase (Figure 5.7b), which corresponds to the plateau part of the reaction force in Figure 5.7a. The two experimental approaches can provide complimentary information in understanding the layer separation properties. Peeling tests provide the average energy release rate over a relatively large interfacial area, but the interlamellar strength cannot be explicitly extracted using this method. On the other hand, direct tension tests measure the interlamellar strength. However, due to the complex peeling-like damage mode and involvement of multiple elastic lamellae in damage propagation near the end of a direct tension test (Figures 5.7a and 5.7b), the energy release rate between adjacent lamellae is missing in this method. In this study, the two experimental methods together with finite element modeling result in a more informative description of the interlamellar bonding within arterial elastin. The interlamellar strength governs the damage initiation point in interlamellar bonding, while the energy release rate determines whether or not damage and dissection will continue to propagate. The CZM finite element model was constructed based on measurements (G_c,

δ_i and F) from peeling tests. The CZM provides a comprehensive description of the mechanical behavior of interlamellar bonding of arterial elastin (Figure 5.9). Changes in the height and area of the traction-separation law profile show that glycation has an evident effect on the stress required to initiate damage and the energy required for damage to propagate. It is worth noting that the separation at damage initiation (δ_i) and the traction at damage initiation (t_{CZM}) are interdependent in the CZM. Once δ_i is determined, t_{CZM} can be estimated from the model. Numerically estimated traction at damage initiation (t_{CZM}) in the CZM agrees well with the experimentally measured interlamellar strength (t_{DT}) from direct tension tests (Figure 5.8). Taken together, this further validates that our approach of identifying δ_i is reliable. It is also interesting to point out that the stress at damage initiation from direct tension test falls between the interlamellar damage initiation in the circumferential and longitudinal directions (Figure 5.8), which suggests the anisotropic nature of the 3D elastin fiber network (Zou and Zhang 2009; Yu et al. 2018a, b; Wang et al. 2020) plays a role in contributing to the strength of the interlamellar bonding.

As demonstrated by peeling tests, larger force and energy is needed for the delamination to propagate in glycated elastin (Figure 5.5). Results of direct tension tests reveal that glucose treatment increases the interlamellar strength, or stress required to initiate delamination (Figure 5.8). Although the most significant changes were observed after 7 days of glucose treatment, the rising trend of F, G_c and t_{DT} over the entire incubation period suggests that the contribution of arterial elastin to interlamellar bonding is enhanced by longer glucose exposure (Figures 5.5 and 5.8). In addition, elastin samples

submerged in PBS alone did not have higher F, G_c and t_{DT} as exhibited in those treated in glucose over the same duration. The fact that no significant differences were observed between the results from untreated and PBS treated groups further rules out the possibility that time rather than solution composition is the factor leading to higher F, G_c and t_{DT}.

Nonenzymatic glycation can induce significant structural and functional changes of elastin which provide possible mechanisms for the higher peeling force, energy release rate and interlamellar strength found in our study. Glycation has been shown to strengthen individual elastin fibers through intermolecular crosslinking (Brownlee et al. 1984; Cerami et al. 1985; Aronson 2003). Nonenzymatic interactions between glucose and proteins can occur within several days to form a sequence of reversible covalent adducts, from Schiff base through to Amadori product, which subsequently transforms slowly through a series of further reactions and rearrangements into stable and irreversible AGEs over a time period ranging from several weeks to months (Brownlee et al. 1984; Cerami et al. 1985). This is in agreement with the stronger interlamellar bonding observed throughout the entire duration of incubation (up to three weeks) in this study (Figures 5.5 and 5.8). AGEs indefinitely attach to long-lived structural proteins, and ultimately give rise to intermolecular crosslinking of proteins through the presence of disulfide bonds and covalent crosslinks, and by trapping soluble proteins and binding them to long-lived structural proteins (Brownlee et al. 1984; Aronson 2003). Therefore, the interlamellar strength and toughness may be strengthened by the increased crosslinking associated with AGE formation. Glutaraldehyde induced crosslinking in

porcine thoracic aortas has been shown to increase the peeling force and energy release rate in peeling tests (Noble et al. 2016).

In this study, the median of Δd is related to the separation distance at damage initiation (δ_i). In peeling tests, the high frequency oscillations of the peeling force originate from discrete failure events of interlamellar elastin fibers. Previous experimental (Black et al. 2005) and theoretical (Hemmer and Hansen 1992; Pradhan et al. 2010) studies have shown that when loading a fibrous material, a sudden drop of force corresponds to micro-ruptures in the material. A recent study from our group suggests that the drops in the peeling force result from failure of a group of interlamellar fibers (Yu et al. 2020). Relating the CZM to experimental data, it is likely that the ramp up of the peeling force oscillation and the displacement increments (Δd) associated with each force ramp up are resulted from recruitment of interlamellar fibers. This gradual accumulation of strain energy at the dissection forefront is followed by a sudden force drop when subsequent cascade failure of interlamellar fibers occurs. This is the basis that links the tissue-level damage initiation to fiber-level failure. This approach has been successfully applied in a previous study of our group (Wang et al. 2020). Our study found significant increase of the displacement increment associated with each ramp up of the peeling force (Δd) in glucose treated arterial elastin (Figures 5.6i and 5.6j). Our study suggests that glycation lead to alterations in the damage initiation properties of arterial elastin. After being exposed to glucose for 21 days, a 50-100% increase in δ_i was found in elastin samples from their untreated counterparts (Table 5.3). Previous studies reported reduced thickness in glucose treated arterial elastin (Zou and Zhang 2012b; Wang et al.

2015), which gives rise to a denser structure in the radial direction with smaller distance between lamellae. Taken together, this suggests that glycation increases the interlamellar failure strain of arterial elastin. It is possible that with glycation the interlamellar fibers are more integrated with the elastic lamellae, thus enhances the resistance to interlamellar damage initiation. Previous studies reported lower degree of alignment (Stephen et al. 2014) and more isotropic mechanical response of elastin (Wang et al. 2015). It is possible that such alterations in in-plane structure and function of elastin may have an impact on the transmural properties of elastin network. While the distance at damage initiation increases with glycation, our study shows that glucose exposure has little influence on the separation distance at complete delamination (δ_c) (Figure 5.9). As interlamellar damage propagates with increasing transmural deformation, the major failure mechanisms of the elastin fiber network are dominated by slipping and rupture of inter-fiber crosslinks (Tang et al. 2010), thus δ_c is likely to be more structure related. Taken together, our study suggests that glycation takes a more dominant effect on the intra-fiber structural level.

Glycation also leads to a dehydrating effect on elastin (Lillie and Gosline 1996). Experimental and simulation studies have both shown that water is essential for maintaining the elasticity of elastin (Gosline 1978; Li et al. 2001). Loss of extrafibrillar water leads to in-plane stiffening of arterial elastin, as well as significant shrinkage of thickness and a denser structure in the radial direction of the tissue (Wang et al. 2018a). In general, a proper water content increases the in-plane failure resistance of arterial (Eisenberg et al. 1981) as well as other types of hydrated soft tissues (Fick and Espino 2011; Werbner et al. 2019). Limited studies have been performed to examine the effect of

dehydration on delamination properties of soft tissues. Dehydrated stratum corneum exhibited higher energy release rate and interlamellar strength during delamination (Wu et al. 2006). Dehydration caused by degeneration has been suggested to increase the potential for delamination between annulus fibrosus layers in intervertebral disc (Gregory et al. 2014). Although no direct connections have been established between the hydration level and the interlamellar bonding properties of arterial wall, it is suggested that excessive accumulation of glycosaminoglycans (GAGs) in the medial layer of the arterial wall increases the local swelling pressure and the risk of dissection (Roccabianca et al. 2014a, b). Therefore, it might be possible that the loss and regional redistribution of water in glycated elastin play a role in altering the interlamellar bonding properties.

5.6 Limitations

Although a slow extension rate for peeling tests was adopted in this study, viscoelastic effects may still exist and affect the measured peeling force and energy release rate (Tong et al. 2014). This study focuses on the effect of glycation on propagation of delamination, while the effect of glucose on other developmental stages of aortic dissection is currently unclear. Besides elastin, glycation can induce alterations in the structure and therefore interlamellar bonding properties of other ECM components and cells as well. For example, crosslinking and stiffening of collagen (Aronson 2003), diminished synthesis of GAGs (Willershausen-Zönnchen et al. 1991) and increased adhesion strength of endothelial cells (Kemeny et al. 2013). Moreover, since diabetes has a close association with other cardiovascular diseases such as hypertension and

atherosclerosis (Cerami et al. 1985; Sowers et al. 2001), which are in turn predisposing factors of aortic dissection (Spittell et al. 1993; Khan and Nair 2002; Nienaber and Clough 2015). Thus, more biomechanical and pathological investigations are needed before we can form a thorough understanding on the relationship between diabetes and the occurrence of aortic dissection.

5.7 Conclusions

Here we investigated the effect of glucose on the propensity to dissection of arterial elastin by combining mechanical testing, multiphoton imaging, and finite element modeling. It was found that nonenzymatic glycation increase the peeling force, energy release rate and interlamellar bonding strength in arterial elastin. The separation distance at damage initiation and interlamellar failure strain also increase with glucose treatment, however the separation distance at complete delamination of arterial elastin remains the same. Results of this study are consistent with the inverse relation reported in the literature that diabetes is associated with a reduced risk of aortic dissection. Nonenzymatic glycation induced crosslinking, more integrated structural reorganization of the elastin fiber network and the loss and regional redistribution of water in glycated elastin are possible mechanisms of the enhanced interlamellar bonding of glucose treated arterial elastin. Future studies combining pathological, biomechanics, and imaging studies are needed to fully understand the microstructural mechanisms of alternated interlamellar bonding in diseases.

CHAPTER 6 EFFECT OF AGING ON THE DISSECTION BEHAVIOR OF HUMAN DESCENDING THORACIC AORTA

6.1 Overview

Both clinical and biomechanical studies have pointed to aging as an important risk factor for type B aortic dissection. However, mechanisms responsible for the compromised aortic interlamellar bonding properties with aging are less understood. In this study, 17 human descending thoracic aortas were collected and divided into three age groups: <40, 40–60 and >60 years. Steady-state mode-I peeling tests were carried out in both the circumferential and longitudinal directions. The peeling force and interlamellar energy release rate decreases with age. All age groups exhibit power-law behavior during dissection propagation with varying exponent of the power-law distribution. A finite element model incorporating discrete interlamellar collagen fibers was employed to simulate peeling and dissection propagation. The interlamellar distance and in-plane shear modulus for the model was determined from experimental measurements. The model precisely recapitulated the power-law distribution that originated from avalanches of ruptures of various magnitudes, and shows decreasing density and increasing degree of dispersion of interlamellar collagen fibers with aging. Correlation analysis further indicates that the decrease in interlamellar collagen fiber density is largely responsible for the diminished interlamellar energy release rate and higher aortic dissection propensity of aging human descending thoracic aorta.

6.2 Introduction

Aortic dissection is a rare but devastating disease affecting 5-30 per million people per year (Khan and Nair, 2002). Depending on the anatomical regions involved, aortic dissection is classified into two major categories according to the Stanford scheme, of which type A involves the ascending thoracic aorta where 59-63% of cases occur, while type B involves the aorta distal to the origin of the left subclavian artery and accounts for 30-38% of cases (Spittell et al. 1993; Prêtre and Von Segesser 1997; Hagan et al. 2000; Khan and Nair, 2002; Durham et al., 2015; Sievers et al. 2020). Though essential to the reduction of mortality rate (Evangelista et al., 2018), early diagnosis of aortic dissection is challenging due to the similarity between the clinical manifestations of aortic dissection and other more prevalent health problems (Nienaber et al. 2016), and largely depends on the anatomical location involved and the haemodynamic stability of the patient for accuracy (Khan and Nair 2002; Nienaber et al. 2016). A better understanding of the underlying mechanisms and the corresponding risk factors would provide an avenue to successful management of aortic dissection and prevention of catastrophic events.

Age is a prominent risk factor of aortic dissection. The majority of patients with acute aortic dissection are in their sixth decade of their life or older (Estrera et al., 2007; Steuer et al., 2011; Jonker et al., 2013). Patients with type B aortic dissection are significantly older than patients with type A aortic dissection (Hagan et al. 2000). In addition, compared with younger patients, elderly patients with acute type B aortic dissection have a higher risk of aortic rupture as well as in-hospital and long-term

mortality (Mehta et al., 2004). Correspondingly, recent investigations using the controlled peeling test have provided biomechanical evidence supporting the effect of aging on aortic dissection propensity, as a decreasing peeling force and dissection energy with aging was found in human ascending thoracic, descending thoracic and abdominal aortas (Angouras et al., 2019; Chung et al., 2020; Horný et al., 2022; Salmasi et al., 2022; Sokolis and Papadodima, 2022; Tong et al., 2022; Xuan et al., 2023). However, the microscale mechanisms responsible for the compromised interlamellar bonding with aging have not been elucidated.

The propagation of aortic dissection is a collective event of the sequential recruitment and failure of discrete extracellular matrix components, which, when being continuously driven in controlled peeling test, gives rise to oscillations of the peeling force (Wang et al., 2021a, 2021b). A drop of the force corresponds to cascade failure of a group of interlamellar units. Previously in our group, by analyzing the distribution of the magnitude of force drops, avalanche-like failure and power-law behavior was found in the propagation of aortic dissection, which results from the structural inhomogeneity of interlamellar fibers as revealed by discrete fiber network based finite element simulations (Yu et al., 2020). Therefore, the power-law behavior may serve as an indicator for microstructural features of the aortic interlamellar spaces.

The objective of this study is to investigate changes in the dissection behavior of human descending thoracic aorta with aging and the associated microstructural mechanisms through an integrated experimental and computational approach. Steady-state peeling test was conducted on human aortic media samples ranging from 24 to 92

years of age to characterize the tissue-level interlamellar bonding properties as well as the power-law behavior. Finite element simulations considering discrete interlamellar collagen fibers were used to capture the avalanches and power-law distribution and provide insights into interlamellar structural remodeling with aging.

6.3 Material and methods

6.3.1 Sample preparation

Human descending thoracic aortas used for the biaxial tensile test as described in Chapter 3 were also used in this study, except aorta N16 due to limited tissue size. Refer to Table 3.1 for the age, gender and selected medical information of the aorta donors. An additional aorta was added in this study, of which the age, gender and selected medical information is given in Table 6.1. Aortas stored in -80°C were defrosted at −20°C for 5 h followed by 3 h at 4°C and then 1 h at room temperature. Loose connective tissues were removed from the adventitial surface. Two rectangular samples with a size of approximately 15 mm × 6 mm were obtained from each aorta. The long edge of one sample was oriented in the circumferential direction of the aorta while that of the other sample was oriented in the longitudinal direction. Since the propagation channel of aortic dissection is within the media (Nienaber et al. 2016; Manopoulos et al. 2018), the adventitial and intimal layers of each aorta was removed with a surgical scalpel, and only the medial layer was kept for mechanical testing. The thickness of each aortic media sample was measured with a caliper. Samples were divided into the same age groups as in Chapter 3: <40 years (n=4), 40-60 years (n=6), and >60 years (n=7).

Table 6.1. Age, gender and selected medical information of the donor of the additional human descending thoracic aorta used in this study. HTN - hypertension; HLP - hyperlipidemia; BMI = body mass index; M = male; Y=yes; CHF = congestive heart failure.

Age (years)	Gender	HTN	HLP	BMI	Cause of death
92	M	Y	Y	20.88	CHF

6.3.2 Peeling test

Refer to Section 2.1 for a detailed description of the experimental protocol. An incision of approximately 5 mm was made into the middle of the thickness of aortic media samples to initiate dissection. Samples were moisturized with 1× PBS spray before each test. Drops of the peeling force/width ($\Delta F/W$) from the peeling force/width – displacement curves, as shown in Figure 6.1, were collected, and the distribution of their probability density ($\Pi(\Delta F/W)$) was analyzed.

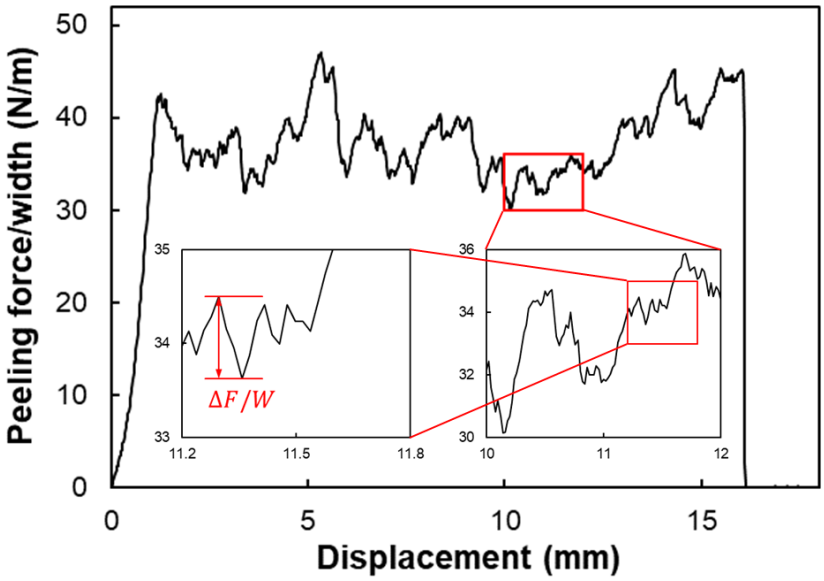

Figure 6.1 A representative experimental peeling force/width ($\boldsymbol{F/W}$) – displacement curve of human descending thoracic aortic media and its zoom-in graphs showing the high frequency oscillation of the peeling force and the drop of peeling force/width ($\boldsymbol{\Delta F/W}$).

6.3.3 Model setup and implementation

A two-dimensional (2D) finite element model previously developed by our group (Yu et al., 2020) was employed to simulate the peeling test. Briefly, two pieces of aortic media with length of 2 mm and thickness of 50 μm were connected by discrete fibers representing interlamellar collagen, as shown in Figure 6.2. Aortic media was meshed with four-node 2D elements and described with the incompressible neo-Hookean constitutive law. The interlamellar collagen fibers were modeled with the Timoshenko beam elements and followed the stress-strain relation $\sigma = 5.4 \times [Exp(5\varepsilon) - 1]$ where σ is the stress and ε is the engineering strain (Hadi et al., 2012). The failure strain of interlamellar collagen fibers ranged uniformly from 0.107 to 0.207 (Miyazaki and

Hayashi, 1999). The orientation of interlamellar fibers was distributed uniformly between $-\theta$ and θ from the dissection plane. Opposite horizontal displacement was prescribed for the top ends of the pieces of aortic media to simulate the peeling test. The simulation was implemented in Abaqus (version 6.14, Simulia, Providence, RI, USA). The peeling force was obtained as the sum of the horizontal nodal reaction forces from the top end of the right piece of aortic media.

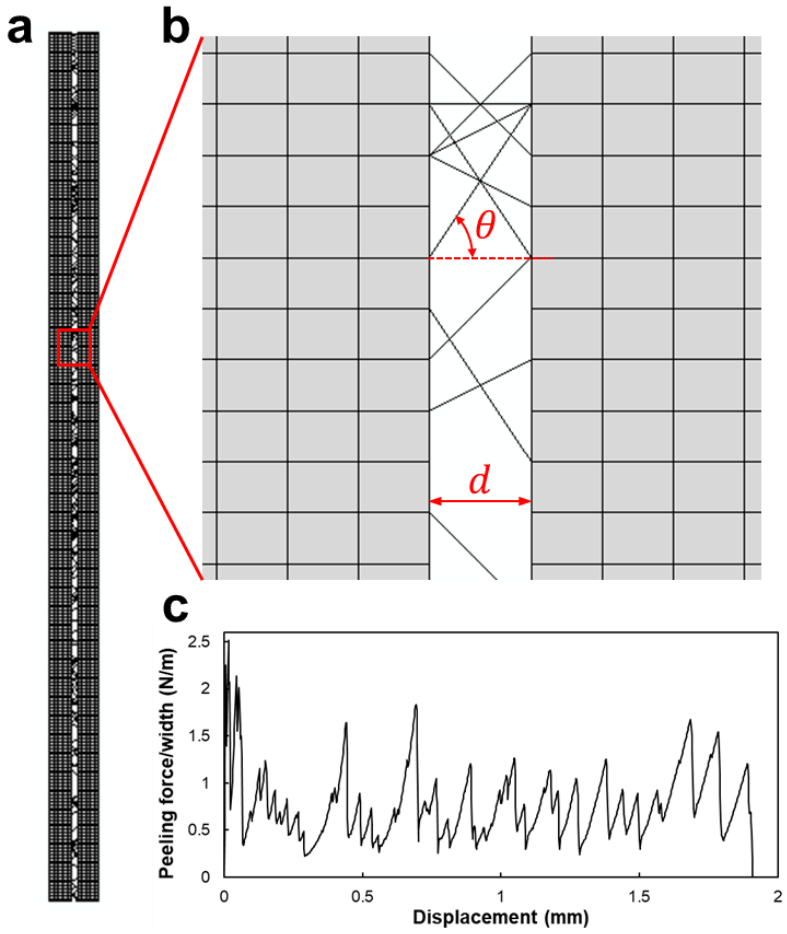

Figure 6.2 Finite element model (a) and a local zoom-in view (b) showing nonuniformly oriented interlamellar fibers. $\boldsymbol{\theta}$ denotes the (maximum) degree of interlamellar fiber dispersion and $\boldsymbol{d}$ denotes interlamellar distance. A representative peeling force/width ($\boldsymbol{F/W}$) – displacement curve obtained from finite element simulations is shown in c.

The distance between the two elastic layers, i.e., interlamellar distance, was obtained by subtracting the thickness of elastic lamellae from the total thickness of aortic media and dividing the remaining thickness by the number of interlamellar gaps as

$$d = \frac{(T_m - nT_{el})}{n-1} \tag{6.1}$$

where d is the mean interlamellar distance and T_m is the mean thickness of aortic media for each age group. $n = 102$ is the average number of elastic lamellae in human descending thoracic aorta, which was found to remain unchanged with aging (Jadidi et al., 2020). $T_{el} = 1.5$ μm is the average thickness of individual elastic lamella (Berry et al., 1993; Dingemans et al., 2000). The elastic energy stored in the tissue during peeling test can be calculated as $F(l - L)$, where l (contour length of one side of the sample as shown by the peeling force/width – displacement curve) and L (original length of the sample before peeling) are the respective deformed and undeformed length of the sample. The strain energy density of an incompressible neo-Hookean material under uniaxial tension is $(\mu/2)[\lambda^2 + (2/\lambda) - 3]$. Therefore, the shear modulus of aortic media was obtained by matching the neo-Hookean strain energy density to the elastic energy storage per unit volume of the tissue during peeling test as

$$\mu = \frac{2F(\lambda-1)}{WT\left(\lambda^2+\frac{2}{\lambda}-3\right)} \tag{6.2}$$

where F is the mean peeling force, $\lambda = l/L$ is the stretch of the sample, μ is the shear modulus, W is the width and T is the thickness of the sample, respectively. Subsequently, for each age group, the number of interlamellar fibers and the degree of interlamellar fiber dispersion (θ) were tuned to fit the simulated power-law exponent to that obtained

from the experimental data. Within each age group, equal number of interlamellar fibers was assumed for the circumferential and longitudinal directions, while θ was independently tuned for each direction. For both experimental and simulation results, the goodness of linear fit ($log\big(\Pi(\Delta F/W)\big) - log(\Delta F/W)$) for the power-law behavior was assessed by the root mean square error (RMSE) and the coefficient of determination (R^2).

6.3.4 Statistical analysis

Data are summarized using bar graphs and are presented as mean ± standard error of the mean (SEM). The Kolmogorov-Smirnov and the Shapiro-Wilk tests were used to examine the normality of the peeling force/width (F/W), energy release rate (G_c), aortic media thickness (T), and shear modulus (μ). Within each age group, paired t-test was used to compare F/W, G_c and μ between the circumferential and longitudinal directions. Across the three age groups, one-way analysis of variance (ANOVA) was used with Bonferroni correction for F/W, G_c, T and μ. For statistical analysis involving data that are not normally distributed, the Wilcoxon signed-rank test and the Kruskal-Wallis H test were used as nonparametric counterparts of the paired t-test and one-way ANOVA. Correlation analysis was performed between the estimated number of interlamellar fibers and G_c. All statistical analysis was performed in SPSS (Version 29, IBM Corp., Armonk, NY). $P < 0.05$ was considered statistically significant.

6.4 Results

The peeling force/width versus displacement curves of all age groups in both the circumferential and longitudinal directions are shown in Figure 6.3. The mean F/W and G_c of each age group are shown in Figure 6.4. The longitudinal and circumferential F/W (unit: N/m) decreases from 29.94 ± 1.26 and 42.79 ± 2.73 for the <40 age group to 26.32 ± 2.59 and 36.11 ± 3.42 for the 40-60 age group and then to 19.77 ± 1.83 and 25.33 ± 2.81 for the >60 age group, respectively. The longitudinal and circumferential G_c (unit: J/m^2) decreases from 67.98 ± 2.87 and 106.17 ± 5.37 for the <40 age group to 57.94 ± 6.11 and 84.08 ± 8.92 for the 40-60 age group and then to 42.30 ± 4.16 and 55.38 ± 6.68 for the >60 age group, respectively. For all three age groups, the longitudinal direction exhibits significantly higher F/W and G_c than the circumferential direction ($p<0.05$), except for G_c of the >60 years group. Significant difference was also found for F/W and G_c between the <40 and >60 years groups of both directions ($p<0.05$), as shown in Figure 6.4.

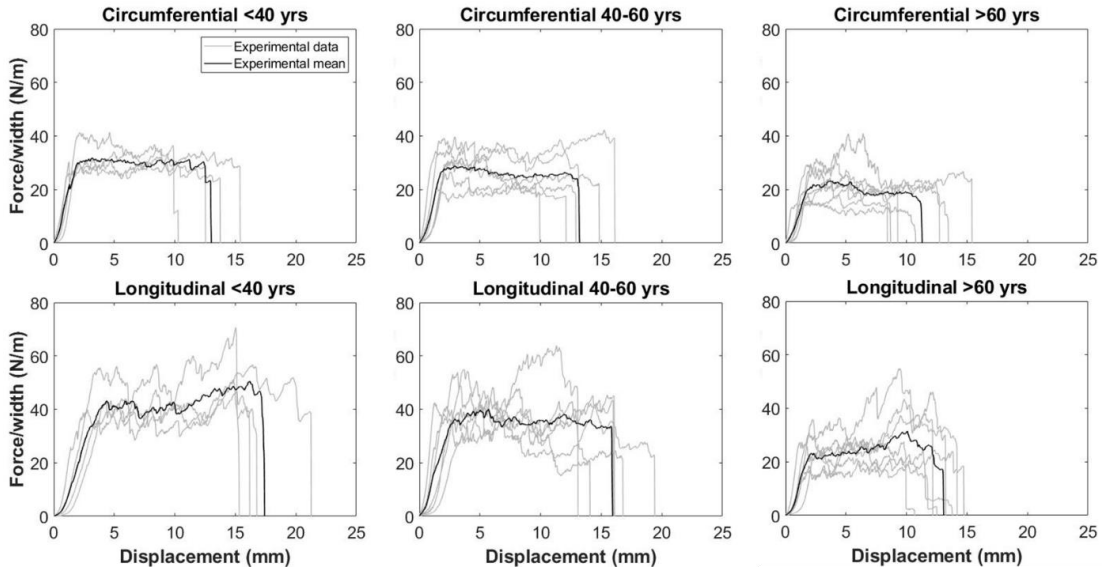

Figure 6.3 Experimental curves of peeling force/width ($\boldsymbol{F/W}$) vs. displacement from peeling tests of human descending thoracic aortic media in the circumferential and longitudinal directions.

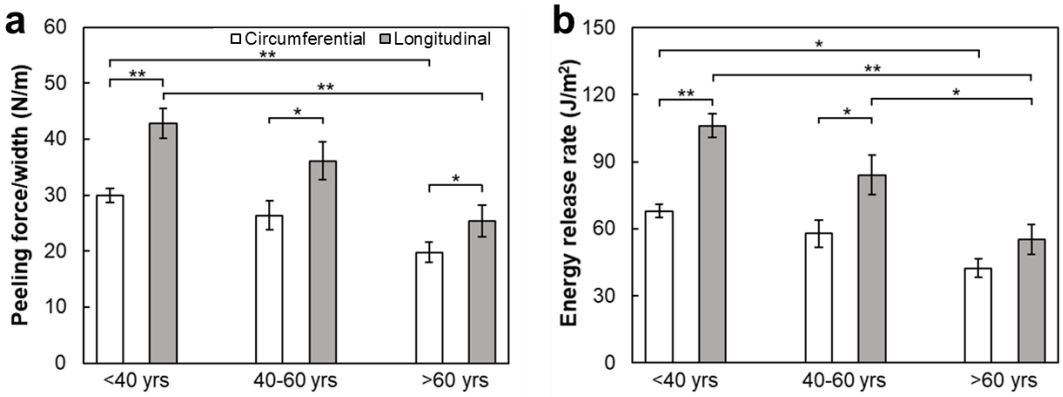

Figure 6.4 Changes of the mean peeling force/width (a) and energy release rate (b) of human descending thoracic aortic media with aging in the circumferential and longitudinal directions. Error bars represent standard error of the mean (SEM). (*p<0.05, **p<0.01)

Figure 6.5 shows changes of T and μ of aortic media with aging. Aortic media shows a thickening trend with aging as T increases from 1.25 ± 0.08 mm to 1.61 ± 0.07 mm and then to 1.66 ± 0.13 mm for the <40, 40-60 and >60 age groups, respectively. Correspondingly, the mean interlamellar distance d of the finite element models was determined to be 10.9 μm, 14.4 μm and 14.9 μm for the <40, 40–60 and >60 age groups, respectively. The longitudinal and circumferential μ (unit: kPa) was found to be 69.91 ± 6.68 and 64.30 ± 9.67 for the <40 age group, 56.57 ± 8.28 and 67.21 ± 8.55 for the 40-60 age group, and 97.52 ± 28.31 and 85.63 ± 11.81 for the >60 age group, respectively. No significant difference was found for μ among the three age groups for both directions, nor for μ between the circumferential and longitudinal directions of the same age group.

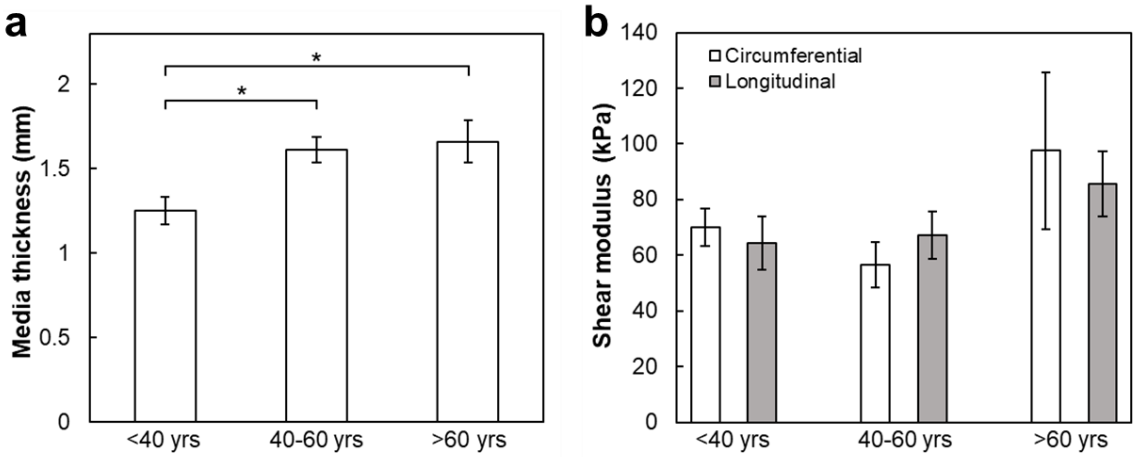

Figure 6.5 Changes of the thickness of aortic media (a) and shear modulus (b) of human descending thoracic aortic media with aging. Error bars represent standard error of the mean (SEM). (*p<0.05)

The probability density distributions of drops of peeling force/width obtained from peeling tests are given in Figure 6.6. Power-law behavior of dissection propagation was identified in all age groups in both the circumferential and longitudinal directions, as shown by the prominent linear profile of the $\Pi(\Delta F/W) - \Delta F/W$ relationship under the double logarithmic scale spanning almost two decades of $\Delta F/W$. The magnitude of the slope of the linear fit, β, corresponds to the exponent of the power-law distribution. In the circumferential direction, β was found to increase from 1.35 to 1.55 and then to 1.74 for the <40, 40-60, and >60 years groups, respectively. On the contrary, in the longitudinal direction, β was found to decrease from 1.49 to 1.46 and then to 1.17 for the <40, 40-60, and >60 years groups, respectively. Changes of the estimated interlamellar structural parameters with aging are summarized in Table 6.2.

Finite element simulations accurately recapitulated the power-law behavior and the associated exponent of dissection propagation, as shown in Figure 6.6. For all age groups in both the circumferential and longitudinal directions, the simulated power-law distribution spans over a decade with R^2 of the linear fit greater than 0.9. The estimated number of interlamellar fibers decreased from 450 to 350 and then to 250. In the circumferential direction, θ increases from 27° to 56° and then to 68° for the <40, 40-60 and >60 years groups, respectively; in the longitudinal direction, θ remains 27° from the <40 to the 40-60 years groups and increases to 68° for the >60 years group. The number of interlamellar fibers was found to be strongly correlated with the interlamellar energy release rate ($p<0.05$) for both directions, as shown in Figure 6.7.

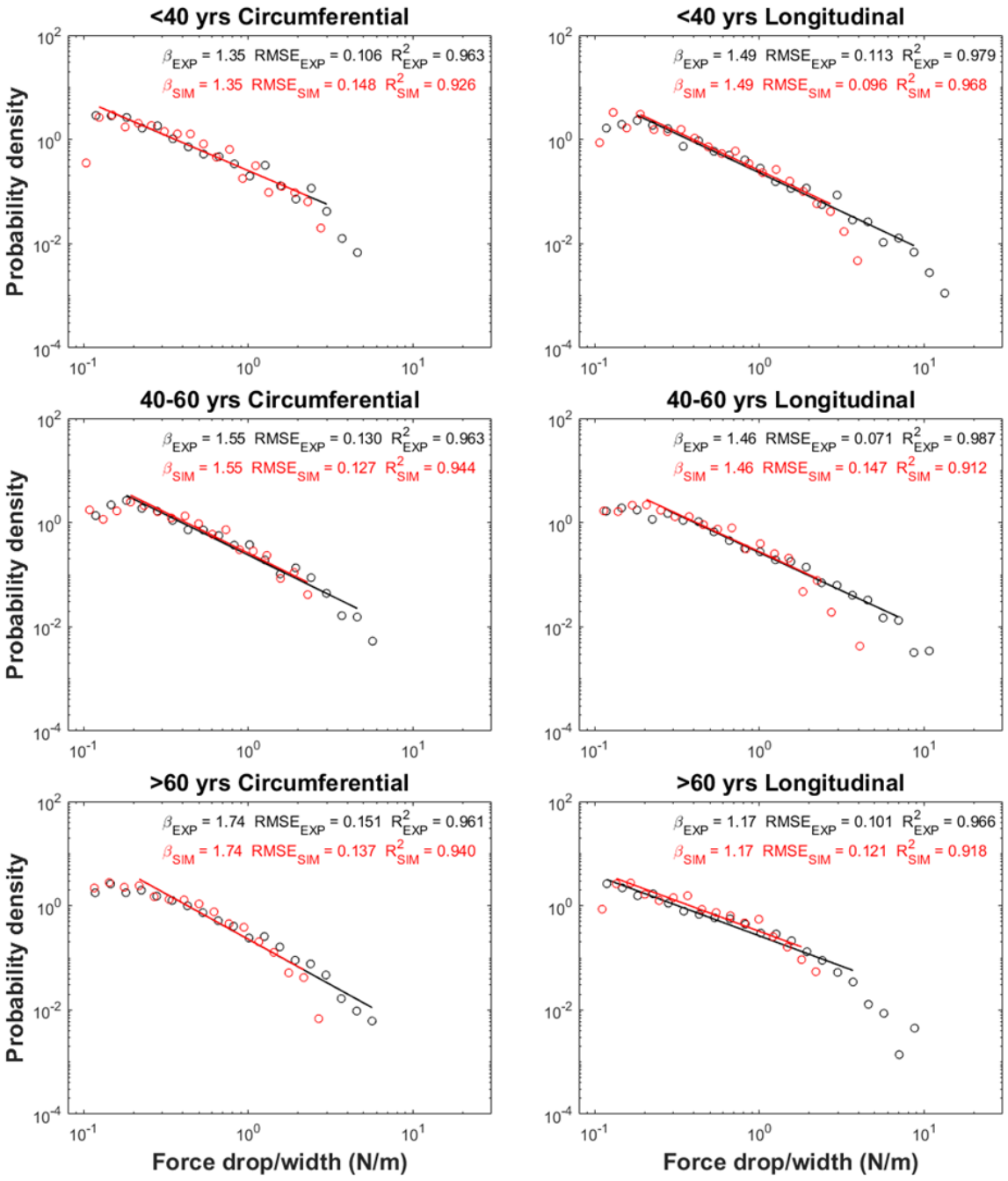

Figure 6.6 Double logarithmic plots of the probability density ($\boldsymbol{\Pi(\Delta F/W)}$) distribution of force drop/width ($\boldsymbol{\Delta F/W}$). Experimental data are shown in black and simulation data are shown in red. The straight lines represent the best power-law fit to the data. In the figure legend, subscripts "EXP" and "SIM" denote experimental and simulation data, respectively.

Table 6.2 Interlamellar fiber structural parameters including the number of fibers per 2 mm of bonded length and the maximum angle of interlamellar fiber dispersion ($\boldsymbol{\theta}$) estimated from finite element simulations.

	<40 yrs		40-60 yrs		>60 yrs	
	Circ	Long	Circ	Long	Circ	Long
number of fibers	450	450	350	350	250	250
out-of-plane dispersion, θ (°)	27	27	56	27	68	68

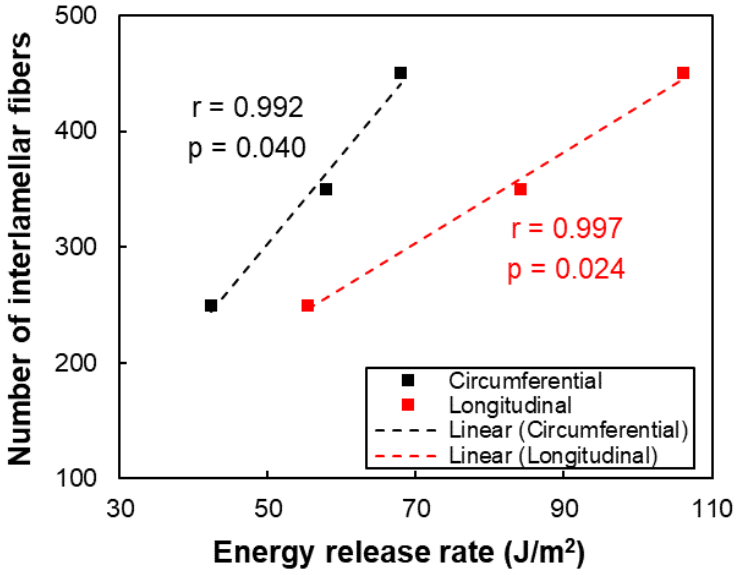

Figure 6.7 Correlation between the number of interlamellar fibers and the interlamellar energy release rate ($\boldsymbol{G_c}$) for both the circumferential and longitudinal directions. Straight dashed lines represent the best linear fit. The correlation coefficient ® and the p-value of the correlation analysis are given.

6.5 Discussion

Type B aortic dissection affects the descending thoracic aorta and has a greater incidence as well as higher morbidity and mortality among elderly patients (Mehta et al., 2004). Our study demonstrates that aging diminishes the interlamellar bonding of the

medial layer of human descending thoracic aorta, as both the peeling force and interlamellar toughness decreases with aging. Avalanches and power-law behavior was exhibited in all age groups, based on which prominent structural alterations of interlamellar collagen fibers including decreasing density and increasing degree of dispersion were found with aorta senescence. Correlation analysis further suggests that the decrease in interlamellar toughness is primarily caused by the decrease in interlamellar collagen density.

Results of the peeling tests are consistent with previous biomechanical investigations where lower peeling force and interlamellar energy release rate was found in the aging aorta (Angouras et al., 2019; Chung et al., 2020; Horný et al., 2022; Salmasi et al., 2022; Sokolis and Papadodima, 2022; Tong et al., 2022; Xuan et al., 2023). The significant decrease of F/W and G_c in the >60 years group also dovetails with the clinically reported mean age between 62 to 67 years of patients with type B aortic dissection (Hagan et al. 2000; Mehta et al., 2004; Estrera et al., 2007; Steuer et al., 2011; Jonker et al., 2013). Therefore, age is critical for risk stratification in type B aortic dissection.

Compared with quantitative structural characterization of aortic extracellular matrix in the circumferential-longitudinal plane, studies focusing on the interlamellar components are scarce (Tsamis et al., 2013). Despite the abundance of clinical and biomechanical data on the relationship between the occurrence of aortic dissection and age, remodeling of interlamellar components and its potential role in the diminishing interlamellar bonding of aging aorta has not been illustrated. Indeed, the obliqueness of

interlamellar fiber orientation (O'Connell et al., 2008) makes quantitative analysis from two-dimensional images of the circumferential-radial and longitudinal-radial cross-sections a great challenge. Computational modeling of the power-law behavior offers an alternative way to evaluate interlamellar fiber structure. The density of interlamellar collagen fibers is proportionally related to interlamellar energy release rate (Figure 6.7). This is corroborated by the dominant role of collagen in determining interlamellar toughness as previously reported (Wang et al., 2021b).

Although the effect of aging on interlamellar fiber dispersion has not been demonstrated before, as another important predisposing factor for aortic dissection, aneurysm significantly increases the out-of-plane dispersion of collagen in abdominal aorta when compared with healthy tissues (Niestrawska et al., 2016). Such dispersion is not only responsible for the avalanches and rapid propagation of aortic dissection (Yu et al., 2020), but might contribute to the in-plane stiffening behavior of human aorta with aging by promoting interlamellar fiber engagement under in-plane tensile loading.

6.6 Conclusions

Our study shows that age is an important risk factor for type B aortic dissection, as aging diminishes the interlamellar bonding of the medial layer of human descending thoracic aorta. Alterations of interlamellar collagen structure occur with aging including lower fiber density and higher degree of fiber dispersion, of which the former is a primary cause of the decreasing interlamellar energy release rate. Future studies focusing on the three-dimensional organization of interlamellar collagen reconstructed from two-

dimensional images of aortic wall cross-sections are needed to improve our understanding of aging-induced aortic remodeling and aortic dissection.

CHAPTER 7 CONCLUSIONS AND OUTLOOK

7.1 Conclusions

The mechanical functions of soft biological tissues are dictated by the structure of their microstructural constituents. The descending thoracic aorta undergoes prominent structural remodeling and disruptions during aging and disease progression. In this dissertation, we studied the mechanical and failure behavior of the descending thoracic aortic wall through an integrated experimental, computational and imaging approach. Findings of this dissertation provide new insights into the etiological mechanisms and health assessment metrics of the aorta from a biomechanical and structural perspective, which could ultimately benefit clinical decision-making, development of interventional devices and therapeutics, and arterial tissue engineering.

Aging induced aortic stiffening is associated with multiple co-morbidities and is caused by the remodeling of individual aortic wall constituents as well as their interactions. Changes of the biaxial mechanical behavior of human descending thoracic aorta with aging were studied (Wang et al., 2023). Both the circumferential and longitudinal directions of the aortic wall stiffen with aging. The increase of stiffness is faster in the longitudinal direction than the circumferential direction, leading to a reverse of the degree of in-plane anisotropy. A constitutive model considering collagen crosslinking was developed to describe the biaxial stress-stretch response of human descending thoracic aorta, and points to collagen crosslinking as a critical contributor to aortic stiffening with aging.

Elastin and collagen fibers are the major structural constituents that endow the

aortic wall with load-bearing and damage-resistance capabilities. Aortic dissection is a life-threatening disease that propagates between elastic lamellae of aortic media. The mechanical and structural contributions of elastin and collagen fibers to interlamellar bonding in the aortic wall were quantitatively demonstrated (Wang et al., 2021b). Collagen has a higher contribution to interlamellar stiffness, strength and toughness. Elastic fibers sustain load in the interlamellar space parallelly with collagen and may fail upon the false lumen starts to form because of the similarity between the strength of interlamellar elastin and the pressure of the true lumen. The higher force and energy observed in longitudinal peeling is due to the combination of in-plane anisotropy of ECM fibers and the boundary condition of controlled peeling test.

As an important step towards a comprehensive understanding of the relationship between diabetes and cardiovascular pathologies, the effect of nonenzymatic glycation on interlamellar bonding of aortic elastin was investigated (Wang et al., 2021a). The strength and toughness of the interlamellar bonding of aortic elastin increases with glycation as well as the interlamellar failure strain, thus lowering the propensity to aortic dissection. These results provide key mechanical mechanisms for the inverse correlation between diabetic mellitus and the occurrence of aortic dissection.

The risk of type-B aortic dissection increases with age and the majority of patients with acute type-B aortic dissection are in their sixth decade of their life or older. Effects of aging on the dissection properties of human descending thoracic aorta and the underlying structural mechanisms were analyzed. The force and energy release rate for dissection propagation in aortic media decreases with aging. Avalanches and power-law

behavior was identified in dissection propagation of aortas of all age groups. Computational modeling of the power-law behavior reveals remarkable alterations of interlamellar collagen structure, including lower density and higher degree of dispersion, of which the former is largely responsible for the decrease of interlamellar energy release rate.

7.2 Outlook

Future studies are necessary for a more thorough understanding of the mechanical and structural mechanisms of aging and diseases of the descending thoracic aorta. Refined mechanical, structural and compositional characterization of healthy and diseased aortas as well as computational modeling with improved fidelity are recommended.

The propagation of aortic dissection *in vivo* is a complicated process that is affected by a combination of the hemodynamic environment as well as the mechanical, structural and geometrical properties of the aortic wall. Rate-dependent mixed-mode delamination testing will allow for the construction of a comprehensive interlamellar cohesive zone model, which can be incorporated into a computational model with realistic geometry of the aorta and pulsatile/cyclic loading conditions to better recapitulate the mechanics of aortic dissection. In addition to the inhomogeneity of interlamellar fibers investigated in this dissertation, focal and layering discontinuity of the aortic ECM might each play a unique role in regulating the initiation and progression of aortic dissection. Advanced experimental techniques as well as computational

modeling considering such mechanical and structural discontinuities would facilitate the establishment of new risk indicators of aortic dissection.

Understanding aortic remodeling with aging and diabetes requires knowledge of the composition and organization of the ECM at both fiber and molecular levels. Multiphoton microscopy with high penetration depth can provide information for the layer-specific orientation distribution and waviness of elastin and collagen fibers with aging, which will be beneficial to developing more robust structure-based constitutive descriptors of the aorta. Also, changes of the interlamellar fiber density and dispersion with aging could be validated with reconstructed high resolution multiphoton images of the circumferential-radial and longitudinal-radial cross-sections of the aortic wall. Quantitative evaluation of various categories of crosslinking using mass spectroscopy and/or Raman spectroscopy is recommended for new insights into the mechanisms of altered mechanical functions of aorta in aging and diabetes.

APPENDIX A KINEMATICS OF BONDED FIBER AND CROSSLINK UNDER BIAXIAL TENSION

Under biaxial tension, the deformation gradient, $\boldsymbol{F}$, is given by:

$$\boldsymbol{F} = \begin{bmatrix} \lambda_1 & 0 & 0 \\ 0 & \lambda_2 & 0 \\ 0 & 0 & \frac{1}{\lambda_1 \lambda_2} \end{bmatrix} \tag{A.1}$$

where λ_1 and λ_2 are stretches in the $\boldsymbol{X_1}$ (longitudinal) and $\boldsymbol{X_2}$ (circumferential) directions respectively, as shown in Figure 3.1. The right Cauchy-Green deformation tensor, $\boldsymbol{C}$, is given by:

$$\boldsymbol{C} = \boldsymbol{F}^T\boldsymbol{F} = \begin{bmatrix} {\lambda_1}^2 & 0 & 0 \\ 0 & {\lambda_2}^2 & 0 \\ 0 & 0 & \frac{1}{{\lambda_1}^2 {\lambda_2}^2} \end{bmatrix} \tag{A.2}$$

In the undeformed configuration, the unit vectors that are parallel ($\boldsymbol{E_1}$ and $\boldsymbol{E_2}$) or normal ($\boldsymbol{E_{1R}}$ and $\boldsymbol{E_{2R}}$) to the orientation of the two collagen fiber families are defined in section 2.2.1. Since the geometry and mechanical properties of bonded fiber and crosslink are symmetric about the longitudinal direction of the aortic sample as are the boundary conditions of biaxial tension (Figure 3.1), only the deformation of fibers oriented in the direction of $\boldsymbol{E_1}$ and their associated crosslinks are considered here. The unit vectors parallel to the orientation of crosslinks in the undeformed configuration are obtained using Equation 3.2 as:

$$\boldsymbol{L_1^+} = \begin{Bmatrix} \cos\theta\cos\alpha_0 - \sin\theta\sin\alpha_0 \\ \sin\theta\cos\alpha_0 + \cos\theta\sin\alpha_0 \\ 0 \end{Bmatrix}, \text{ and } \boldsymbol{L_1^-} = \begin{Bmatrix} -\cos\theta\cos\alpha_0 - \sin\theta\sin\alpha_0 \\ -\sin\theta\cos\alpha_0 + \cos\theta\sin\alpha_0 \\ 0 \end{Bmatrix} \tag{A.3}$$

The square of fiber stretch under biaxial tension, $I_{4,1}$, is obtained as:

$$I_{4,1} = \boldsymbol{E_1} \cdot \boldsymbol{CE_1} = \boldsymbol{e_1} \cdot \boldsymbol{e_1} = {\lambda_1}^2 \cos^2\theta + {\lambda_2}^2 \sin^2\theta > 1 \quad \text{(A.4)}$$

where $\boldsymbol{e_1}(=\boldsymbol{FE_1})$ is the push-forward of the unit vector in the direction of collagen fibers in the deformed configuration.

The squares of crosslink stretch under biaxial tension, I_1^+ and I_1^-, are obtained as:

$$I_1^+ = \boldsymbol{L_1^+} \cdot \boldsymbol{CL_1^+} = \boldsymbol{l_1^+} \cdot \boldsymbol{l_1^+} = {\lambda_1}^2 \cos^2(\theta + \alpha_0) + {\lambda_2}^2 \sin^2(\theta + \alpha_0) > 1, \text{ and}$$

$$I_1^- = \boldsymbol{L_1^-} \cdot \boldsymbol{CL_1^-} = \boldsymbol{l_1^-} \cdot \boldsymbol{l_1^-} = {\lambda_1}^2 \cos^2(\alpha_0 - \theta) + {\lambda_2}^2 \sin^2(\alpha_0 - \theta) > 1 \quad \text{(A.5)}$$

where $\boldsymbol{l_1^+}(=\boldsymbol{FL_1^+})$ and $\boldsymbol{l_1^-}(=\boldsymbol{FL_1^-})$ are push-forwards of the unit vector in the direction of crosslinks in the deformed configuration.

The invariants I_8^{1+} and I_8^{1-} under biaxial deformation are given by:

$$I_8^{1+} = \boldsymbol{L_1^+} \cdot \boldsymbol{CE_1} = \boldsymbol{l_1^+} \cdot \boldsymbol{e_1} = \|\boldsymbol{l_1^+}\|\|\boldsymbol{e_1}\| \cos\alpha^+ = {\lambda_1}^2 \cos\theta \cos(\theta + \alpha_0) + {\lambda_2}^2 \sin\theta \sin(\theta + \alpha_0), \text{ and}$$

$$I_8^{1-} = \boldsymbol{L_1^-} \cdot \boldsymbol{CE_1} = \boldsymbol{l_1^-} \cdot \boldsymbol{e_1} = \|\boldsymbol{l_1^+}\|\|\boldsymbol{e_1}\| \cos\alpha^- = -{\lambda_1}^2 \cos\theta \cos(\alpha_0 - \theta) + {\lambda_2}^2 \sin\theta \sin(\alpha_0 - \theta) \quad \text{(A.6)}$$

The cosine of the angle between bonded fiber and crosslink in the deformed configuration is given by Equation 3.6 as:

$$I_{8*}^{1+} = \cos\alpha^+ = \frac{I_8^{1+}}{\sqrt{I_{4,1} I_1^+}} =$$

$$\frac{\cos\theta \cos(\theta+\alpha_0) + r^2 \sin\theta \sin(\theta+\alpha_0)}{\sqrt{\cos^2\theta\cos^2(\theta+\alpha_0) + r^2\cos^2\theta\sin^2(\theta+\alpha_0) + r^2\sin^2\theta\cos^2(\theta+\alpha_0) + r^4\sin^2\theta\sin^2(\theta+\alpha_0)}}, \text{ and}$$

$$I_{8*}^{1-} = \cos\alpha^- = \frac{I_8^{1-}}{\sqrt{I_{4,1} I_1^-}} =$$

$$\frac{-\cos\theta \cos(\alpha_0-\theta) + r^2 \sin\theta \sin(\alpha_0-\theta)}{\sqrt{\cos^2\theta\cos^2(\alpha_0-\theta) + r^2\cos^2\theta\sin^2(\alpha_0-\theta) + r^2\sin^2\theta\cos^2(\alpha_0-\theta) + r^4\sin^2\theta\sin^2(\alpha_0-\theta)}} \quad \text{(A.7)}$$

where $r = \lambda_2/\lambda_1$ is the ratio of stretches between the circumferential and longitudinal directions.

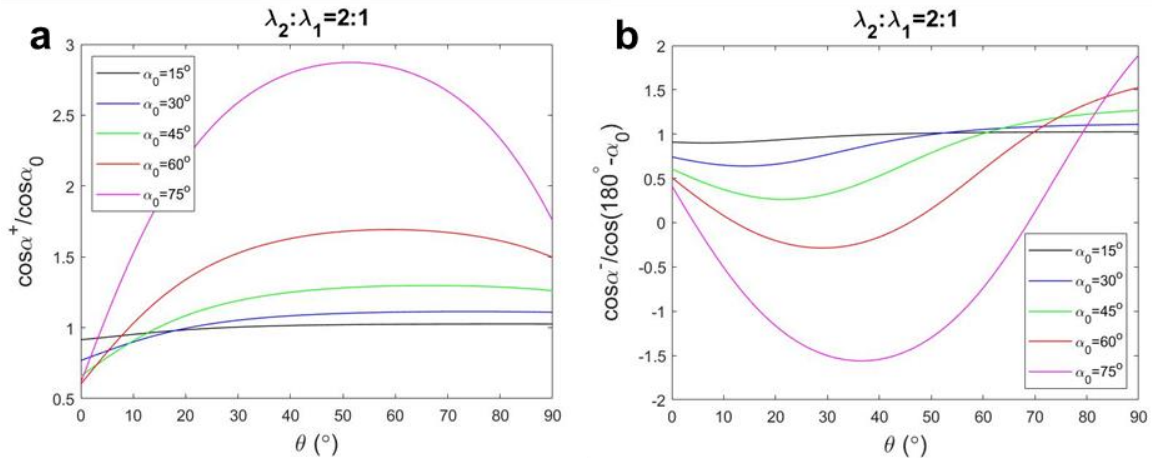

Figure A.1 Change of a $\boldsymbol{cos\alpha^{+}/cos\alpha_0}$ and b $\boldsymbol{cos\alpha^{-}/cos(180°-\alpha_0)}$ with varying $\boldsymbol{\theta}$ (the angle between the longitudinal direction of the aortic sample $\boldsymbol{X_1}$ and collagen fiber direction $\boldsymbol{E_1}$) and $\boldsymbol{\alpha_0}$ (the angle between collagen fiber direction $\boldsymbol{E_1}$ and crosslink direction $\boldsymbol{L_1^+}$) when the biaxial stretch ratio between the circumferential ($\boldsymbol{\lambda_2}$) and longitudinal ($\boldsymbol{\lambda_1}$) directions is 2:1.

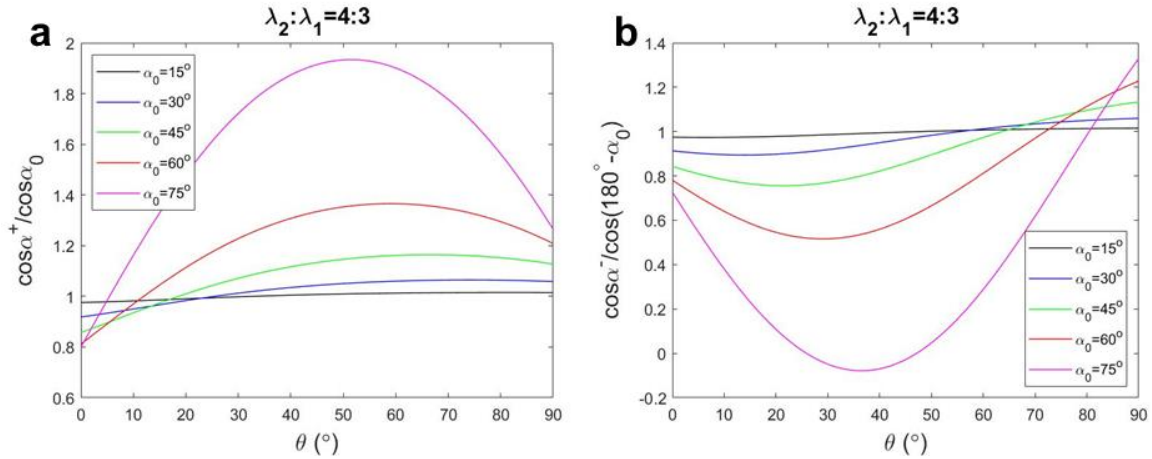

Figure A.2 Change of a $\boldsymbol{cos\alpha^{+}/cos\alpha_0}$ and b $\boldsymbol{cos\alpha^{-}/cos(180°-\alpha_0)}$ with varying $\boldsymbol{\theta}$ (the angle between the longitudinal direction of the aortic sample $\boldsymbol{X_1}$ and collagen fiber direction $\boldsymbol{E_1}$) and $\boldsymbol{\alpha_0}$ (the angle between collagen fiber direction $\boldsymbol{E_1}$ and crosslink direction $\boldsymbol{L_1^+}$) when the biaxial stretch ratio between the circumferential ($\boldsymbol{\lambda_2}$) and longitudinal ($\boldsymbol{\lambda_1}$) directions is 4:3.

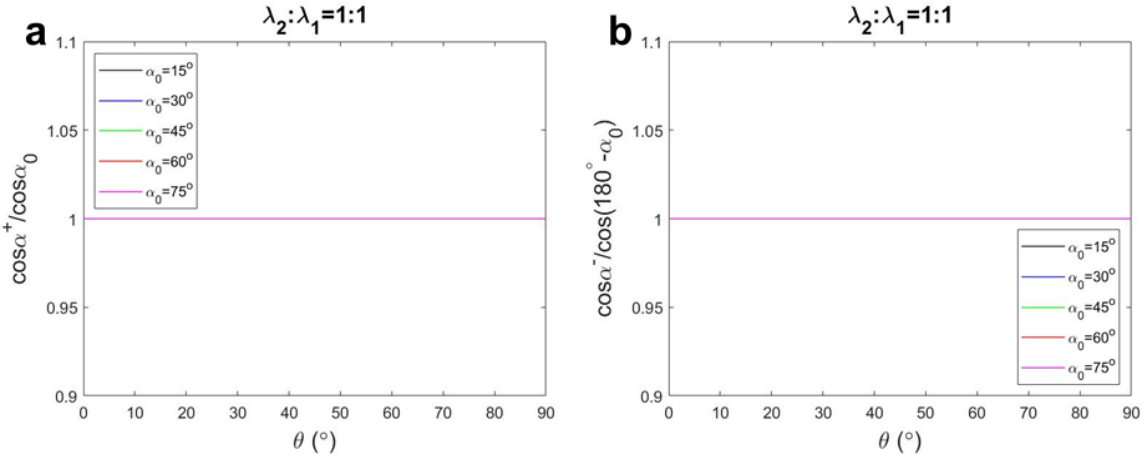

Figure A.3 Change of a $\boldsymbol{cos\alpha^+/cos\alpha_0}$ and b $\boldsymbol{cos\alpha^-/cos(180^\circ-\alpha_0)}$ with varying $\boldsymbol{\theta}$ (the angle between the longitudinal direction of the aortic sample $\boldsymbol{X_1}$ and collagen fiber direction $\boldsymbol{E_1}$) and $\boldsymbol{\alpha_0}$ (the angle between collagen fiber direction $\boldsymbol{E_1}$ and crosslink direction $\boldsymbol{L_1^+}$) when the biaxial stretch ratio between the circumferential ($\boldsymbol{\lambda_2}$) and longitudinal ($\boldsymbol{\lambda_1}$) directions is 1:1.

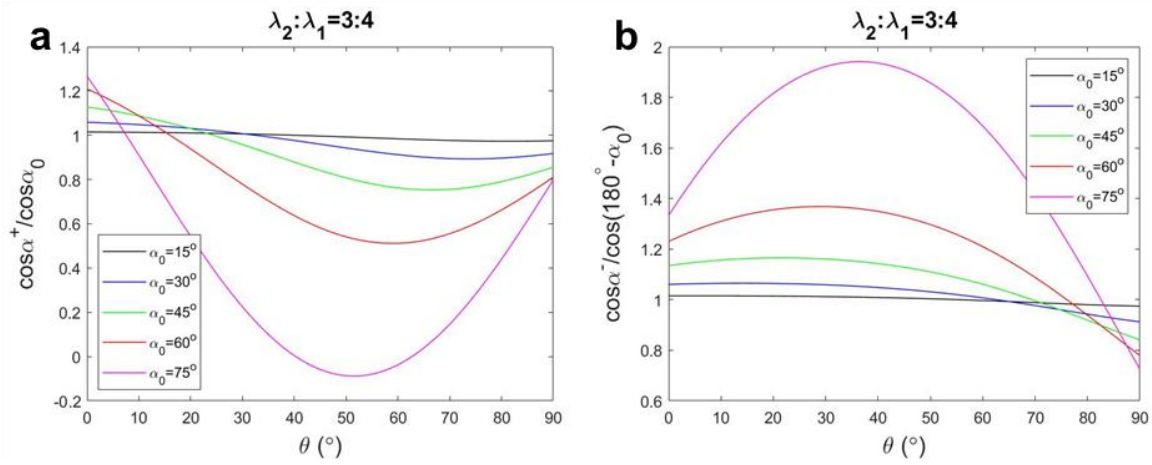

Figure A.4 Change of a $\boldsymbol{cos\alpha^+/cos\alpha_0}$ and b $\boldsymbol{cos\alpha^-/cos(180^\circ-\alpha_0)}$ with varying $\boldsymbol{\theta}$ (the angle between the longitudinal direction of the aortic sample $\boldsymbol{X_1}$ and collagen fiber direction $\boldsymbol{E_1}$) and $\boldsymbol{\alpha_0}$ (the angle between collagen fiber direction $\boldsymbol{E_1}$ and crosslink direction $\boldsymbol{L_1^+}$) when the biaxial stretch ratio between the circumferential ($\boldsymbol{\lambda_2}$) and longitudinal ($\boldsymbol{\lambda_1}$) directions is 3:4.

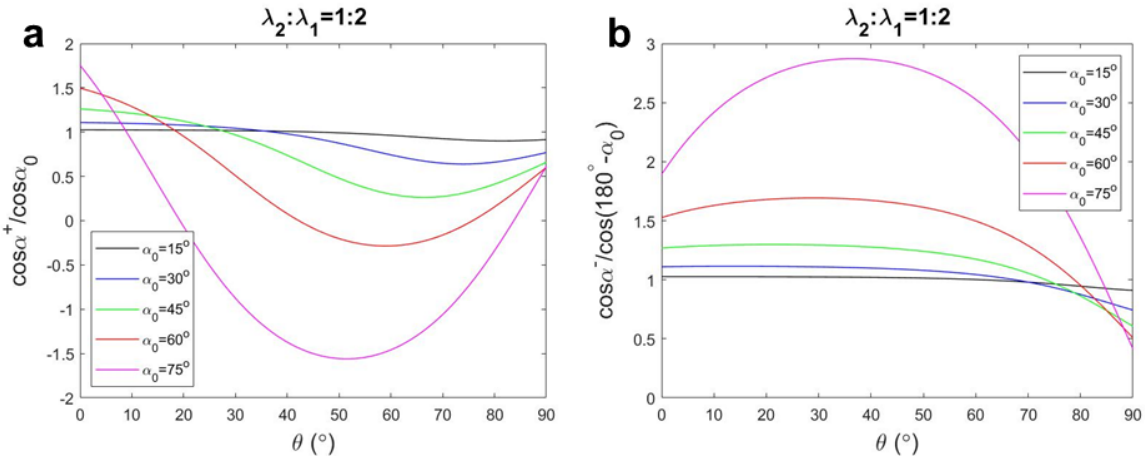

Figure A.5 Change of a $\boldsymbol{cos\alpha^{+}/cos\alpha_0}$ and b $\boldsymbol{cos\alpha^{-}/cos(180° - \alpha_0)}$ with varying $\boldsymbol{\theta}$ (the angle between the longitudinal direction of the aortic sample $\boldsymbol{X_1}$ and collagen fiber direction $\boldsymbol{E_1}$) and $\boldsymbol{\alpha_0}$ (the angle between collagen fiber direction $\boldsymbol{E_1}$ and crosslink direction $\boldsymbol{L_1^+}$) when the biaxial stretch ratio between the circumferential ($\boldsymbol{\lambda_2}$) and longitudinal ($\boldsymbol{\lambda_1}$) directions is 1:2.

BIBLIOGRAPHY

Amabili M, Asgari M, Breslavsky ID, Franchini G, Giovanniello F, Holzapfel GA (2021) Microstructural and mechanical characterization of the layers of human descending thoracic aortas. Acta Biomaterialia 134:401-421.

Amabili M, Balasubramanian P, Bozzo I, Breslavsky ID, Ferrari G (2019) Layer-specific hyperelastic and viscoelastic characterization of human descending thoracic aortas. Journal of the Mechanical Behavior of Biomedical Materials 99:27-46.

Andreotti L, Bussotti A, Cammelli D, Di Giovine F, Sampognaro S, Sterrantino G, Varcasia G, Arcangeli P (1985) Aortic connective tissue in ageing—a biochemical study. Angiology 36(12):872-879.

Angouras DC, Kritharis EP, Sokolis DP (2019) Regional distribution of delamination strength in ascending thoracic aortic aneurysms. Journal of the Mechanical Behavior of Biomedical Materials 98:58-70.

Aronson D (2003) Cross-linking of glycated collagen in the pathogenesis of arterial and myocardial stiffening of aging and diabetes. Journal of Hypertension 21:3-12.

Avdic T, Franzeán S, Zarrouk M, Acosta S, Nilsson P, Gottsäter A, Svensson AM, Gudbjörnsdottir S, Eliasson B (2018) Reduced long-term risk of aortic aneurysm and aortic dissection among individuals with type 2 diabetes mellitus: a nationwide observational study. Journal of the American Heart Association 7:e007618.

Avolio A, Jones D, Tafazzoli-Shadpour M (1998) Quantification of alterations in structure and function of elastin in the arterial media. Hypertension 32:170-175.

Barenblatt GI (1962) The mathematical theory of equilibrium cracks in brittle fracture. Advances in Applied Mechanics 7:55-129.

Berry CL, Sosa‐Melgarejo JA, Greenwald SE (1993) The relationship between wall tension, lamellar thickness, and intercellular junctions in the fetal and adult aorta: its relevance to the pathology of dissecting aneurysm. Journal of Pathology 169(1):15-20.

Black LD, Brewer KK, Morris SM, Schreiber BM, Toselli P, Nagent MA, Suki B, Stone PJ (2005) Effects of elastase on the mechanical and failure properties of engineered elastin-rich matrices. Journal of Applied Physiology 98:1434–1441.

Blount KJ, Hagspiel KD (2009) Aortic diameter, true lumen, and false lumen growth rates in chronic type B aortic dissection. American Journal of Roentgenology 192:W222-W229.

Bonow RO, Smaha LA, Smith SC, Mensah GA, Lenfant C (2002) World Heart Day 2002: The international burden of cardiovascular disease: Responding to the emerging global epidemic. Circulation 106:1602-1605.

Brankovic SA, Hawthorne EA, Yu X, Zhang Y, Assoian RK (2019) MMP12 deletion preferentially attenuates axial stiffening of aging arteries. Journal of Biomechanical Engineering 141(8):081004.

Brownlee M., Cerami A, Vlassara H (1988) Advanced glycosylation end products in tissue and the biochemical basis of diabetic complications. New England Journal of Medicine 318:1315-1321.

Brownlee M, Vlassara H, Cerami A (1984) Nonenzymatic glycosylation and the pathogenesis of diabetic complications. Annals of Internal Medicine 101:527-537.

Brüel A, Ørtoft G, Oxlund H (1998) Inhibition of cross-links in collagen is associated with reduced stiffness of the aorta in young rats. Atherosclerosis 140(1):135-145.

Brüel A, Oxlund H (1996) Changes in biomechanical properties, composition of collagen and elastin, and advanced glycation endproducts of the rat aorta in relation to age. Atherosclerosis 127(2):155-165.

Buehler MJ (2008) Nanomechanics of collagen fibrils under varying cross-link densities: atomistic and continuum studies. Journal of the Mechanical Behavior of Biomedical Materials 1(1):59-67.

Cameron JD, Bulpitt CJ, Pinto ES, Rajkumar C (2003) The aging of elastic and muscular arteries: A comparison of diabetic and nondiabetic subjects. Diabetes Care 26:2133-2138.

Carmo M, Colombo L, Bruno A, Corsi FRM, Roncoroni L, Cuttin MS, Radice F, Mussini E, Settembrini PG (2002) Alteration of elastin, collagen and their cross-links in abdominal aortic aneurysms. European Journal of Vascular and Endovascular Surgery 23(6):543-549.

Carson MW, Roach MR (1990) The strength of the aortic media and its role in the propagation of aortic dissection. Journal of Biomechanics 23:579-588.

Cattell MA, Anderson JC, Hasleton PS (1996) Age-related changes in amounts and concentrations of collagen and elastin in normotensive human thoracic aorta. Clinica Chimica Acta 245(1):73-84.

Cavinato C, Murtada SI, Rojas A, Humphrey JD (2021) Evolving structure-function relations during aortic maturation and aging revealed by multiphoton microscopy. Mechanisms of Ageing and Development 196:111471.

Cecelja M, Chowienczyk P (2012) Role of arterial stiffness in cardiovascular disease. JRSM Cardiovascular Disease 1(4):1-10.

Cerami A, Vlassara H, Brownlee M (1985) Protein glycosylation and the pathogenesis of atherosclerosis. Metabolism 34:37-44.

Chandran PL, Barocas VH (2006) Affine versus non-affine fibril kinematics in collagen networks: theoretical studies of network behavior. Journal of Biomechanical Engineering 128(2):259-270.

Chaturvedi N (2007) The burden of diabetes and its complications: Trends and implications for intervention. Diabetes Research and Clinical Practice 76(Suppl.1): S3–12.

Chen JS, Han W, Wu CT, Duan W (1997) On the perturbed Lagrangian formulation for nearly incompressible and incompressible hyperelasticity. Computer Methods in Applied Mechanics and Engineering 142:335-351.

Chen YC, Chen M, Gaffney EA, Brown CP (2017) Effect of crosslinking in cartilage-like collagen microstructures. Journal of the Mechanical Behavior of Biomedical Materials 66:138-143.

Chitsaz S, Azadani AN, Matthews PB, Chuter TA, Tseng EE, Ge L (2012) Hemodynamic determinants of aortic dissection propagation by 2D computational modeling: Implications for endovascular stent-grafting. Journal of Cardiovascular Surgery 53:631-640.

Chow MJ, Choi M, Yun SH, Zhang Y (2013a) The effect of static stretch on elastin degradation in arteries. PLoS ONE 8:e81951.

Chow MJ, Mondonedo JR, Johnson VM, Zhang Y (2013b) Progressive structural and biomechanical changes in elastin degraded aorta. Biomechanics and Modeling in Mechanobiology 12:361-372.

Chow MJ, Turcotte R, Lin CP, Zhang Y (2014) Arterial extracellular matrix: A mechanobiological study of the contributions and interactions of elastin and collagen. Biophysical Journal 106(12):2684-2692.

Chung JCY, Wong E, Tang M, Eliathamby D, Forbes TL, Butany J, Simmons CA, Ouzounian M (2020) Biomechanics of aortic dissection: a comparison of aortas associated with bicuspid and tricuspid aortic valves. Journal of the American Heart Association 9(15):e016715.

Clark TE, Lillie MA, Vogl AW, Gosline JM, Shadwick RE (2015) Mechanical contribution of lamellar and interlamellar elastin along the mouse aorta. Journal of Biomechanics 48:3599-3605.

Concannon J, Dockery P, Black A, Sultan S, Hynes N, McHugh PE, Moerman KM, McGarry JP (2020) Quantification of the regional bioarchitecture in the human aorta. Journal of Anatomy 236(1):142-155.

De D, Pawar N, Gupta AN (2020) Glucose-induced structural changes and anomalous diffusion of elastin. Colloids and Surfaces B: Biointerfaces 188:110776.

Depalle B, Qin Z, Shefelbine SJ, Buehler MJ (2015) Influence of cross-link structure, density and mechanical properties in the mesoscale deformation mechanisms of collagen fibrils. Journal of the Mechanical Behavior of Biomedical Materials 52:1-13.

Dernellis J, Panaretou M (2005) Aortic stiffness is an independent predictor of progression to hypertension in nonhypertensive subjects. Hypertension 45(3):426-431.

Dillon-Murphy D, Noorani A, Nordsletten D, Figueroa CA (2016) Multi-modality image-based computational analysis of haemodynamics in aortic dissection. Biomechanics and Modeling in Mechanobiology 15:857-876.

Dingemans KP, Teeling P, Lagendijk JH, Becker AE (2000) Extracellular matrix of the human aortic media: an ultrastructural histochemical and immunohistochemical study of the adult aortic media. The Anatomical Record 258(1):1-14.

Doyle BJ, Norman PE (2016) Computational biomechanics in thoracic aortic dissection: Today's approaches and tomorrow's opportunities. Annals of Biomedical Engineering 44:71-83.

Dugdale DS (1960) Yielding of steel sheets containing slits. Journal of the Mechanics and Physics of Solids 8:100-104.

Durham CA, Cambria RP, Wang LJ, Ergul EA, Aranson NJ, Patel VI, Conrad MF (2015) The natural history of medically managed acute type B aortic dissection. Journal of Vascular Surgery 61(5):1192-1199.

Eisenberg RL, Bank WO, Hedgock MW (1981) Renal failure after major angiography can be avoided with hydration. American Journal of Roentgenology 136:859-861.

Erbel R, Alfonso F, Boileau C, Dirsch O, Eber B, Haverich A, Rakowski H, Struyven J, Radegran K, Sechtem U, Taylor J, Zollikofer Ch, Klein WW, Mulder B, Providencia LA (2001) Diagnosis and management of aortic dissection: Recommendations of the

Task Force on Aortic Dissection, European Society of Cardiology. European Heart Journal 22:1642–1681.

Estrera AL, Miller CC, Goodrick J, Porat EE, Achouh PE, Dhareshwar J, Meada R, Azizzadeh A, Safi HJ (2007) Update on outcomes of acute type B aortic dissection. The Annals of Thoracic Surgery 83(2):S842-S845.

Evangelista A, Isselbacher EM, Bossone E, Gleason TG, Eusanio MD, Sechtem U, Ehrlich MP, Trimarchi S, Braverman AC, Myrmel T, Harris KM, Hutchinson S, O'Gara P, Suzuki T, Nienaber CA, Eagle KA (2018) Insights from the international registry of acute aortic dissection: a 20-year experience of collaborative clinical research. Circulation 137(17):1846-1860.

Everson-Rose SA, Lewis TT (2005) Psychosocial factors and cardiovascular diseases. Annual Review of Public Health 26:469-500.

Eyre DR, Paz MA, Gallop PM (1984) Cross-linking in collagen and elastin. Annual Review of Biochemistry 53(1):717-748.

Ferrara A, Pandolfi A (2008) Numerical modelling of fracture in human arteries. Computer Methods in Biomechanics and Biomedical Engineering 11:553-567.

Ferrara A, Pandolfi A (2010) A numerical study of arterial media dissection processes. International Journal of Fracture 166:21-33.

Ferruzzi J, Madziva D, Caulk AW, Tellides G, Humphrey JD (2018) Compromised mechanical homeostasis in arterial aging and associated cardiovascular consequences. Biomechanics and Modeling in Mechanobiology 17(5):1281-1295.

Ferruzzi J, Vorp DA, Humphrey JD (2011) On constitutive descriptors of the biaxial mechanical behaviour of human abdominal aorta and aneurysms. Journal of The Royal Society Interface 8(56):435-450.

Fick JM, Espino DM (2011) Articular cartilage surface rupture during compression: Investigating the effects of tissue hydration in relation to matrix health. Journal of the Mechanical Behavior of Biomedical Materials 4:1311-1317.

Franchini G, Breslavsky ID, Holzapfel GA, Amabili M (2021) Viscoelastic Characterization of Human Descending Thoracic Aortas Under Cyclic Load. Acta Biomaterialia 130:291-307.

Fujimoto D (1982) Aging and cross-linking in human aorta. Biochemical and Biophysical Research Communications 109(4):1264-1269.

García-Herrera CM, Celentano DJ, Cruchaga MA, Rojo FJ, Atienza JM, Guinea GV, Goicolea JM (2012) Mechanical characterisation of the human thoracic descending aorta: experiments and modelling. Computer Methods in Biomechanics and Biomedical Engineering 15(2):185-193.

Gasser TC, Holzapfel GA (2006) Modeling the propagation of arterial dissection. European Journal of Mechanics-A/Solids 25:617-633.

Gasser TC, Ogden RW, Holzapfel GA (2006) Hyperelastic modelling of arterial layers with distributed collagen fibre orientations. Journal of The Royal Society Interface 3:15-35.

Geest JPV, Sacks MS, Vorp DA (2004) Age dependency of the biaxial biomechanical behavior of human abdominal aorta. Journal of Biomechanical Engineering 126(6): 815-822.

Gentleman E, Lay AN, Dickerson DA, Nauman EA, Livesay GA, Dee KC (2003) Mechanical characterization of collagen fibers and scaffolds for tissue engineering. Biomaterials 24: 3805-3813.

Gosline JM (1978) Hydrophobic interaction and a model for the elasticity of elastin. Biopolymers 17:677-695.

Gregory DE, Bae WC, Sah RL, Masuda K (2014) Disc degeneration reduces the delamination strength of the annulus fibrosus in the rabbit annular disc puncture model. The Spine Journal 14:1265-1271.

Gültekin O, Holzapfel GA (2018) A brief review on computational modeling of rupture in soft biological tissues. In: Oñate E, Peric D, de Souza Neto E, Chiumenti M (eds) Advances in Computational Plasticity. Computational Methods in Applied Sciences, vol 46. Springer, Cham, pp 113-144.

Hadi MF, Sander EA, Barocas VH (2012) Multiscale model predicts tissue-level failure from collagen fiber-level damage. Journal of Biomechanical Engineering 134(9):091005.

Hagan PG, Nienaber CA, Isselbacher EM, Bruckman D, Karavite DJ, Russman PL, Evangelista A, Fattori R, Suzuki T, Oh JK, Moore AG, Malouf JF, Pape LA, Gaca C, Sechtem U, Lenferink S, Deutsch HJ, Diedrichs H, Marcos y Robles J, Llovet A, Gilon D, Das SK, Armstrong WF, Deeb GM, Eagle KA (2000) The international registry of acute aortic dissection (IRAD): New insights into an old disease. JAMA: The Journal of the American Medical Association 283:897-903.

Haskett D, Johnson G, Zhou A, Utzinger U, Vande Geest J (2010) Microstructural and biomechanical alterations of the human aorta as a function of age and location. Biomechanics and Modeling in Mechanobiology 9:725-736.

He X, Liu X, Liu W, Wang B, Liu Y, Li Z, Wang T, Tan R, Gao B, Zeng H (2015) Association between diabetes and risk of aortic dissection: a case-control study in a Chinese population. PLoS ONE 10:e0142697.

Hemmer PC, Hansen A (1992) The distribution of simultaneous fiber failures in fiber bundles. Journal of Applied Mechanics 59:909-914.

Hickson SS, Butlin M, Graves M, Taviani V, Avolio AP, McEniery CM, Wilkinson IB (2010) The relationship of age with regional aortic stiffness and diameter. JACC: Cardiovascular Imaging 3(12):1247-1255.

Holzapfel GA, Gasser TC, Ogden RW (2000) A new constitutive framework for arterial wall mechanics and a comparative study of material models. Journal of Elasticity 61:1-48.

Holzapfel GA, Gasser TC, Stadler M (2002) A structural model for the viscoelastic behavior of arterial walls: Continuum formulation and finite element analysis. European Journal of Mechanics-A/Solids 21:441-463.

Holzapfel GA, Niestrawska JA, Ogden RW, Reinisch AJ, Schriefl AJ (2015) Modelling non-symmetric collagen fibre dispersion in arterial walls. Journal of The Royal Society Interface 12(106):20150188.

Holzapfel GA, Ogden RW (2020) An arterial constitutive model accounting for collagen content and cross-linking. Journal of the Mechanics and Physics of Solids 136: 103682.

Holzapfel GA, Sommer G, Auer M, Regitnig P, Ogden RW (2007) Layer-specific 3D residual deformations of human aortas with non-atherosclerotic intimal thickening. Annals of Biomedical Engineering 35:530-545.

Holzapfel GA, Sommer G, Gasser CT, Regitnig P (2005) Determination of layer-specific mechanical properties of human coronary arteries with nonatherosclerotic intimal thickening and related constitutive modeling. American Journal of Physiology – Heart and Circulatory Physiology 289:H2048–H2058.

Holzapfel GA, Sommer G, Regitnig P (2004) Anisotropic mechanical properties of tissue components in human atherosclerotic plaques. Journal of Biomechanical Engineering 126:657-665.

Horný L, Roubalová L, Kronek J, Chlup H, Adámek T, Blanková A, Petřivý Z, Suchý T, Tichý P (2022) Correlation between age, location, orientation, loading velocity and delamination strength in the human aorta. Journal of the Mechanical Behavior of Biomedical Materials 133:105340.

Hoshino H, Takahashi M, Kushida K, Ohishi T, Kawana K, Inoue T (1995) Quantitation of the crosslinks, pyridinoline, deoxypyridinoline and pentosidine, in human aorta with dystrophic calcification. Atherosclerosis 112(1):39-46.

Humphrey JD (2002) Cardiovascular Solid Mechanics. Springer, New York.

Humphrey JD, Holzapfel GA (2012) Mechanics, mechanobiology, and modeling of human abdominal aorta and aneurysms. Journal of Biomechanics 45:805-814.

Humphrey JD, Na S (2002) Elastodynamics and arterial wall stress. Annals of Biomedical Engineering 30:509-523.

Jadidi M, Habibnezhad M, Anttila E, Maleckis K, Desyatova A, MacTaggart J, Kamenskiy A (2020) Mechanical and structural changes in human thoracic aortas with age. Acta Biomaterialia 103:172-188.

Jiménez-Trujillo I, González-Pascual M, Jiménez-Garća R, Hernández-Barrera V, Miguel-Yanes JM, Méndez-Bailón M, de Miguel-Diez J, Salinero-Fort MÁ, Perez-Farinos N, Carrasco-Garrido P, Lopez-De-Andrés A (2016) Type 2 diabetes mellitus and thoracic aortic aneurysm and dissection: an observational population-based study in Spain from 2001 to 2012. Medicine 95:e3618.

John R, Thomas J (1972) Chemical compositions of elastins isolated from aortas and pulmonary tissues of humans of different ages. Biochemical Journal 127(1):261-269.

Jonker FH, Trimarchi S, Muhs BE, Rampoldi V, Montgomery DG, Froehlich JB, Peterson MD, Bartnes K, Gourineni V, Ramanath VS, Braverman AC, Nienaber CA, Isselbacher EM, Eagle KA, IRAD Investigators (2013) The role of age in complicated acute type B aortic dissection. The Annals of Thoracic Surgery 96(6):2129-2134.

Kemeny SF, Cicalese S, Figueroa DS, Clyne AM (2013) Glycated collagen and altered glucose increase endothelial cell adhesion strength. Journal of Cellular Physiology 228:1727-1736.

Kendall K (1975) Thin-film peeling-the elastic term. Journal of Physics D: Applied Physics 8:1449-1452.

Khan IA, Nair CK (2002) Clinical, diagnostic, and management perspectives of aortic dissection. Chest 122:311-328.

Kielty CM, Sherratt MJ, Shuttleworth CA (2002) Elastic fibres. Journal of Cell Science 155:2817-2828.

Kim J, Baek S (2011) Circumferential variations of mechanical behavior of the porcine thoracic aorta during the inflation test. Journal of Biomechanics 44(10):1941-1947.

Kim J, Hong JW, Baek S (2013) Longitudinal differences in the mechanical properties of the thoracic aorta depend on circumferential regions. Journal of Biomedical Materials Research Part A 101(5):1525-1529.

Kim J, Staiculescu MC, Cocciolone AJ, Yanagisawa H, Mecham RP, Wagenseil JE (2017) Crosslinked elastic fibers are necessary for low energy loss in the ascending aorta. Journal of Biomechanics 61:199-207.

Kinloch AJ, Lau CC, Williams JG (1994) The peeling of flexible laminates. International Journal of Fracture 66:45-70.

Kodama K, Nishigami K, Sakamoto T, Sawamura T, Hirayama T, Misumi H, Nakao K (2008) Tight heart rate control reduces secondary adverse events in patients with type B acute aortic dissection. Circulation (14_suppl_1) 118:S167-S170.

Konova E, Baydanoff S, Atanasova M, Velkova A (2004) Age-related changes in the glycation of human aortic elastin. Experimental Gerontology 39:249-254.

Kwansa AL, De Vita R, Freeman JW (2016) Tensile mechanical properties of collagen type I and its enzymatic crosslinks. Biophysical Chemistry 214:1-10.

Langewouters GJ, Wesseling KH, Goedhard WJA (1984) The static elastic properties of 45 human thoracic and 20 abdominal aortas in vitro and the parameters of a new model. Journal of Biomechanics 17(6):425-435.

Leng X, Chen X, Deng X, Sutton MA, Lessner SM (2015) Modeling of experimental atherosclerotic plaque delamination. Annals of Biomedical Engineering 43:2838-2851.

Leng X, Davis LA, Deng X, Sutton MA, Lessner SM (2016) Numerical modeling of experimental human fibrous cap delamination. Journal of the Mechanical Behavior of Biomedical Materials 59:322-336.

Leng X, Zhou B, Deng X, Davis L, Lessner SM, Sutton MA, Shazly T (2018) Experimental and numerical studies of two arterial wall delamination modes. Journal of the Mechanical Behavior of Biomedical Materials 77:321-330.

Li B, Alonso DOV, Bennion BJ, Daggett V (2001) Hydrophobic hydration is an important source of elasticity in elastin-based biopolymers. Journal of the American Chemical Society 123:11991-11998.

Lillie MA, Gosline JM (2002) The viscoelastic basis for the tensile strength of elastin. International Journal of Biological Macromolecules 30:119-127.

Lillie MA, Gosline JM (1996) Swelling and viscoelastic properties of osmotically stressed elastin. Biopolymers 39:641-652.

Lindeman JH, Ashcroft BA, Beenakker JWM, van Es M, Koekkoek NB, Prins FA, Tielemans JF, Abdul-Hussien H, Bank RA, Oosterkamp TH (2010) Distinct defects in collagen microarchitecture underlie vessel-wall failure in advanced abdominal aneurysms and aneurysms in Marfan syndrome. Proceedings of the National Academy of Sciences of the United States of America 107(2):862-865.

Lin S, Gu L (2015) Influence of crosslink density and stiffness on mechanical properties of type I collagen gel. Materials 8(2):551-560.

Liu H, Shi L, Zeng T, Ji Q, Shi Y, Huang Y, Zhang L, Xiao T, Ye J, Lin Y, Liu L (2019) Type 2 diabetes mellitus reduces clinical complications and mortality in Stanford type B aortic dissection after thoracic endovascular aortic repair: A 3-year follow-up study. Life Sciences 230: 104-110.

Lu Q, Ganesan K, Simionescu DT, Vyavahare NR (2004) Novel porous aortic elastin and collagen scaffolds for tissue engineering. Biomaterials 25:5227-5237.

MacLean NF, Dudek NL, Roach MR (1999) The role of radial elastic properties in the development of aortic dissections. Journal of Vascular Surgery 29:703-710.

Manopoulos C, Karathanasis I, Kouerinis I, Angouras DC, Lazaris A, Tsangaris S, Sokolis DP (2018) Identification of regional/layer differences in failure properties and thickness as important biomechanical factors responsible for the initiation of aortic dissections. Journal of Biomechanics 80:102-110.

Mansouri MR, Fuchs PF, Criscione JC, Schrittesser B, Beter J (2021) The contribution of mechanical interactions to the constitutive modeling of fiber-reinforced elastomers. European Journal of Mechanics-A/Solids 85:104081.

Mattson JM, Turcotte R, Zhang Y (2017) Glycosaminoglycans contribute to extracellular matrix fiber recruitment and arterial wall mechanics. Biomechanics and Modeling in Mechanobiology 16:213-225.

Mehta RH, Bossone E, Evangelista A, T O'Gara P, Smith DE, Cooper JV, Oh JK, Januzzi JL, Hutchison S, Gilon D, Pape LA, Nienaber CA, Isselbacher EM, Eagle KA,

International Registry of Acute Aortic Dissection (IRAD) Investigators (2004) Acute type B aortic dissection in elderly patients: clinical features, outcomes, and simple risk stratification rule. The Annals of Thoracic Surgery 77(5):1622-1628.

Merei B, Badel P, Davis L, Sutton MA, Avril S, Lessner SM (2017) Atherosclerotic plaque delamination: Experiments and 2D finite element model to simulate plaque peeling in two strains of transgenic mice. Journal of the Mechanical Behavior of Biomedical Materials 67:19-30.

Merodio J, Ogden RW (2006) The influence of the invariant I8 on the stress–deformation and ellipticity characteristics of doubly fiber-reinforced non-linearly elastic solids. International Journal of Non-Linear Mechanics 41(4):556-563.

Miyazaki H, Hayashi K (1999) Tensile tests of collagen fibers obtained from the rabbit patellar tendon. Biomedical Microdevices 2:151-157.

Nienaber CA, Clough RE (2015) Management of acute aortic dissection. The Lancet 385:800-811.

Nienaber CA, Clough RE, Sakalihasan N, Suzuki T, Gibbs R, Mussa F, Jenkins MP, Thompson MM, Evangelista A, Yeh JS, Cheshire N, Rosendahl U, Pepper J (2016) Aortic dissection. Nature Reviews. Disease Primers 2(1):1-18.

Niestrawska JA, Viertler C, Regitnig P, Cohnert TU, Sommer G, Holzapfel GA (2016) Microstructure and mechanics of healthy and aneurysmatic abdominal aortas: experimental analysis and modelling. Journal of The Royal Society Interface 13: 20160620.

Noble C, Smulders N, Lewis R, Carré MJ, Franklin SE, MacNeil S, Taylor ZA (2016) Controlled peel testing of a model tissue for diseased aorta. Journal of Biomechanics 49:3667-3675.

North BJ, Sinclair DA (2012) The intersection between aging and cardiovascular disease. Circulation Research 110(8):1097-1108.

O'Connell MK, Murthy S, Phan S, Xu C, Buchanan JA, Spilker R, Dalman RL, Zarins CK, Denk W, Taylor CA (2008) The three-dimensional micro- and nanostructure of the aortic medial lamellar unit measured using 3D confocal and electron microscopy imaging. Matrix Biology 27:171-181.

O'Rourke MF, Safar ME (2005) Relationship between aortic stiffening and microvascular disease in brain and kidney: cause and logic of therapy. Hypertension 46(1):200-204.

Pal S, Tsamis A, Pasta S, D'Amore A, Gleason TG, Vorp DA, Maiti S (2014) A mechanistic model on the role of "radially-running" collagen fibers on dissection properties of human ascending thoracic aorta. Journal of Biomechanics 47:981-988.

Parmigiani JP, Thouless MD (2006) The roles of toughness and cohesive strength on crack deflection at interfaces. Journal of the Mechanics and Physics of Solids 54:266-287.

Pasta S, Phillippi JA, Gleason TG, Vorp DA (2012) Effect of aneurysm on the mechanical dissection properties of the human ascending thoracic aorta. The Journal of Thoracic and Cardiovascular Surgery 143:460-467.

Pasta S, Phillippi JA, Tsamis A, D'Amore A, Raffa GM, Pilato M, Scardulla C, Watkins SC, Wagner WR, Gleason TG, Vorp DA (2016) Constitutive modeling of ascending thoracic aortic aneurysms using microstructural parameters. Medical Engineering & Physics 38:121-130.

Pradhan S, Hansen A, Chakrabarti BK (2010) Failure processes in elastic fiber bundles. Reviews of Modern Physics 82:499-555.

Prakash SK, Pedroza C, Khalil YA, Milewicz DM (2012) Diabetes and reduced risk for thoracic aortic aneurysms and dissections: A nationwide case-control study. Journal of the American Heart Association 1(2):e000323.

Prêtre R, Von Segesser LK (1997) Aortic dissection. The Lancet 349(9063):1461-1464.

Purslow PP (1983) Positional variations in fracture toughness, stiffness and strength of descending thoracic pig aorta. Journal of Biomechanics 16(11):947-953.

Qiu H, Zhu Y, Sun Z, Trzeciakowski JP, Gansner M, Depre C, Resuello RR, Natividad FF, Hunter WC, Genin GM, Elson EL, Vatner DE, Meininger GA, Vatner SF (2010) Vascular smooth muscle cell stiffness as a mechanism for increased aortic stiffness with aging. Circulation Research 107(5):615-619.

Rajagopal K, Bridges C, Rajagopal KR (2007) Towards an understanding of the mechanics underlying aortic dissection. Biomechanics and Modeling in Mechanobiology 6:345-359.

Rasmussen BL, Bruenger E, Sandberg LB (1975) A new method for purification of mature elastin. Analytical Biochemistry 64(1):255-259.

Reiser K, McCormick RJ, Rucker RB (1992) Enzymatic and nonenzymatic cross‐linking of collagen and elastin. The FASEB Journal 6(7):2439-2449.

Riambau V, Böckler D, Brunkwall J, Cao P, Chiesa R, Coppi G, Czerny M, Fraedrich G, Haulon S, Jacobs MJ, Lachat ML, Moll FL, Setacci C, Taylor PR, Thompson M, Trimarchi S, Verhagen HJ, Verhoeven EL, ESVS Guidelines Committee, Kolh P, de Borst GJ, Chakfe N, Debus ES, Hinchliffe RJ, Kakkos S, Koncar I, Lindholt JS, Vega de Ceniga M, Vermassen F, Verzini F, Document R, Kolh P, Black JH 3rd, Busund R, Bjorck M, Dake M, Dick F, Eggebrecht H, Evangelista A, Grabenwoger M, Milner R, Naylor AR, Ricco JB, Rousseau H, Schmidli J (2017) Editor's choice–management of descending thoracic aorta diseases: clinical practice guidelines of the European Society for Vascular Surgery (ESVS). European Journal of Vascular and Endovascular Surgery 53(1):4-52.

Rinaudo A, D'Ancona G, Lee JJ, Pilato G, Amaducci A, Baglini R, Follis F, Pilato M, Pasta S (2014) Predicting Outcome of Aortic Dissection with Patent False Lumen by Computational Flow Analysis. Cardiovascular Engineering and Technology 5:176-188.

Roach MR, Song SH (1994) Variations in strength of the porcine aorta as a function of location. Clinical and Investigative Medicine 17:308-318.

Roccabianca S, Ateshian GA, Humphrey JD (2014a) Biomechanical roles of medial pooling of glycosaminoglycans in thoracic aortic dissection. Biomechanics and Modeling in Mechanobiology 13:13-25.

Roccabianca S, Bellini C, Humphrey JD (2014b) Computational modelling suggests good, bad and ugly roles of glycosaminoglycans in arterial wall mechanics and mechanobiology. Journal of The Royal Society Interface 11:20140397.

Roccabianca S, Figueroa CA, Tellides G, Humphrey JD (2014c) Quantification of regional differences in aortic stiffness in the aging human. Journal of the Mechanical Behavior of Biomedical Materials 29:618-634.

Rosenbloom J, Abrams WR, Mecham R (1993) Extracellular matrix 4: the elastic fiber. The FASEB Journal 7:1208-1218.

Rouleau L, Tremblay D, Cartier R, Mongrain R, Leask RL (2012) Regional variations in canine descending aortic tissue mechanical properties change with formalin fixation. Cardiovascular Pathology 21(5):390-397.

Sacks MS (2000) Biaxial mechanical evaluation of planar biological materials. Journal of Elasticity 61(1):199-246.

Sacks MS, Zhang W, Wognum S (2016) A novel fibre-ensemble level constitutive model for exogenous cross-linked collagenous tissues. Interface Focus 6(1):20150090.

Sáez P, Peña E, Martínez MA (2014) A structural approach including the behavior of collagen cross-links to model patient-specific human carotid arteries. Annals of Biomedical Engineering 42(6):1158-1169.

Salmasi MY, Sasidharan S, Frattolin J, Edgar L, Stock U, Athanasiou T, Moore Jr J (2022) Regional variation in biomechanical properties of ascending thoracic aortic aneurysms. European Journal of Cardio-Thoracic Surgery 62(3):ezac392.

Schellekens JCJ, De Borst R (1993) On the numerical integration of interface elements. International Journal for Numerical Methods in Engineering 36(1):43-66.

Schlatmann TJ, Becker AE (1977) Histologic changes in the normal aging aorta: implications for dissecting aortic aneurysm. The American Journal of Cardiology 39(1):13-20.

Schram MT, Henry RMA, Van Dijk RAJM, Kostense PJ, Dekker JM, Nijpels G, Heine RJ, Bouter LM, Westerhof N, Stehouwer CDA (2004) Increased central artery stiffness in impaired glucose metabolism and type 2 diabetes: the Hoorn Study. Hypertension 43:176-181.

Schriefl AJ, Zeindlinger G, Pierce DM, Regitnig P, Holzapfel GA (2012) Determination of the layer-specific distributed collagen fibre orientations in human thoracic and abdominal aortas and common iliac arteries. Journal of The Royal Society Interface 9(71):1275-1286.

Seyedsalehi S, Zhang L, Choi J, Baek S (2015) Prior distributions of material parameters for Bayesian calibration of growth and remodeling computational model of abdominal aortic wall. Journal of Biomechanical Engineering 137(10):101001.

Shen ZL, Dodge MR, Kahn H, Ballarini R, Eppell SJ (2008) Stress-strain experiments on individual collagen fibrils. Biophysical Journal 95:3956-3963.

Sherebrin MH, Hegney JE, Roach MR (1989) Effects of age on the anisotropy of the descending human thoracic aorta determined by uniaxial tensile testing and digestion by NaOH under load. Canadian Journal of Physiology and Pharmacology 67(8):871-878.

Sherifova S, Holzapfel GA (2019) Biomechanics of aortic wall failure with a focus on dissection and aneurysm: A review. Acta Biomaterialia 99:1-17.

Sievers HH, Rylski B, Czerny M, Baier AL, Kreibich M, Siepe M, Beyersdorf F (2020) Aortic dissection reconsidered: type, entry site, malperfusion classification adding clarity and enabling outcome prediction. Interactive Cardiovascular and Thoracic Surgery 30(3):451-457.

Silverstein MC, Bilici K, Morgan SW, Wang Y, Zhang Y, Boutis GS (2015) 13C, 2H NMR studies of structural and dynamical modifications of glucose-exposed porcine aortic elastin. Biophysical Journal 108:1758-1772.

Sims TJ, Rasmussen LM, Oxlund H, Bailey AJ (1996) The role of glycation cross-links in diabetic vascular stiffening. Diabetologia 39:946-951.

Smart EJ, Ying YS, Donzell WC, Anderson RGW (1996) A role for caveolin in transport of cholesterol from endoplasmic reticulum to plasma membrane. Journal of Biological Chemistry 271(46): 29427–29435.

Snedeker JG, Gautieri A (2014) The role of collagen crosslinks in ageing and diabetes-the good, the bad, and the ugly. Muscles, Ligaments and Tendons Journal 4(3):303-308.

Sokolis DP, Papadodima SA (2022) Regional delamination strength in the human aorta underlies the anatomical localization of the dissection channel. Journal of Biomechanics 141:111174.

Sokolis DP (2007) Passive mechanical properties and structure of the aorta: segmental analysis. Acta Physiologica 190(4):277-289.

Sommer G, Gasser TC, Auer M, Regitnig P, Holzapfel GA (2008) Dissection properties of the human aortic media: an experimental study. Journal of Biomechanical Engineering 130:021007.

Sowers JR, Epstein M, Frohlich ED (2001) Diabetes, hypertension, and cardiovascular disease an update. Hypertension 37:1053-1059.

Spencer AJM (1984) Constitutive theory for strongly anisotropic solids. In Continuum theory of the mechanics of fibre-reinforced composites 1-32. Springer, Vienna.

Spina M, Garbin G (1976) Age-related chemical changes in human elastins from non-atherosclerotic areas of thoracic aorta. Atherosclerosis 24(1-2):267-279.

Spina M, Garbisa S, Hinnie J, Hunter JC, Serafini-Fracassini A (1983) Age-related changes in composition and mechanical properties of the tunica media of the upper thoracic human aorta. Arteriosclerosis 3(1):64-76.

Spittell PC, Spittell JA, Joyce JW, Tajik AJ, Edwards WD, Schaff HV, Stanson AW (1993) Clinical features and differential diagnosis of aortic dissection: Experience with 236 cases (1980 through 1990). Mayo Clinic Proceedings 68:642-651.

Stehouwer CDA, Ferreira I (2006) Diabetes, lipids and other cardiovascular risk factors, in: Arterial Stiffness in Hypertension. Elsevier, p. 427.

Stemper BD, Yoganandan N, Pintar FA (2007) Mechanics of arterial subfailure with increasing loading rate. Journal of Biomechanics 40:1806-1812.

Stephen EA, Venkatasubramaniam A, Good TA, Topoleski LDT (2014) The effect of glycation on arterial microstructure and mechanical response. Journal of Biomedical Materials Research Part A 102(8):2565-2572.

Steuer J, Eriksson MO, Nyman R, Björck M, Wanhainen A (2011) Early and long-term outcome after thoracic endovascular aortic repair (TEVAR) for acute complicated type B aortic dissection. European Journal of Vascular and Endovascular Surgery 41(3):318-323.

Sugita S, Matsumoto T (2018) Local distribution of collagen fibers determines crack initiation site and its propagation direction during aortic rupture. Biomechanics and Modeling in Mechanobiology 17:577-587.

Sun H, Zhong M, Miao Y, Ma X, Gong HP, Tan HW, Zhang Y, Zhang W (2009) Impaired elastic properties of the aorta in fat-fed, streptozotocin-treated rats. Cardiology 114(2):107–113.

Taghizadeh H, Tafazzoli-Shadpour M (2017) Characterization of mechanical properties of lamellar structure of the aortic wall: Effect of aging. Journal of the Mechanical Behavior of Biomedical Materials 65:20-28.

Takagi H, Umemoto T (2017) Negative association of diabetes with thoracic aortic dissection and aneurysm. Angiology 68:216-224.

Tam ASM, Sapp MC, Roach MR (1998) The effect of tear depth on the propagation of aortic dissections in isolated porcine thoracic aorta. Journal of Biomechanics 31:673-676.

Tang Y, Ballarini R, Buehler MJ, Eppell SJ (2010) Deformation micromechanisms of collagen fibrils under uniaxial tension. Journal of The Royal Society Interface 7:839-850.

Theivacumar NS, Stephenson MA, Mistry H, Valenti D (2014) Diabetics are less likely to develop thoracic aortic dissection: a 10-year single-center analysis. Annals of Vascular Surgery 28(2):427-432.

Thubrikar MJ, Agali P, Robicsek F (1999) Wall stress as a possible mechanism for the development of transverse intimal tears in aortic dissections. Journal of Medical Engineering & Technology 23(4):127-134.

Thunes JR, Phillippi JA, Gleason TG, Vorp DA, Maiti S (2018) Structural modeling reveals microstructure-strength relationship for human ascending thoracic aorta. Journal of Biomechanics 71:84-93.

Tian L, Wang Z, Liu Y, Eickhoff JC, Eliceiri KW, Chesler NC (2016) Validation of an arterial constitutive model accounting for collagen content and crosslinking. Acta Biomaterialia 31:276-287.

Tiessen IM, Roach MR (1993) Factors in the initiation and propagation of aortic dissections in human autopsy aortas. Journal of Biomechanical Engineering 115:123-125.

Toda T, Tsuda N, Nishimori I, Leszczynski DE, Kummerow FA (1980) Morphometrical analysis of the aging process in human arteries and aorta. Cells Tissues Organs 106(1):35-44.

Tong J, Abudupataer M, Xu X, Zhang Z, Li J, Lai H, Wang C, Zhu K (2022) Gender differences in the dissection properties of ascending thoracic aortic aneurysms. Interactive CardioVascular and Thoracic Surgery 35(2):ivac068.

Tong J, Cheng Y, Holzapfel GA (2016) Mechanical assessment of arterial dissection in health and disease: Advancements and challenges. Journal of Biomechanics 49:2366-2373.

Tong J, Cohnert T, Regitnig P, Kohlbacher J, Birner-Gruenberger R, Schriefl AJ, Sommer G, Holzapfel GA (2014) Variations of dissection properties and mass fractions with thrombus age in human abdominal aortic aneurysms. Journal of Biomechanics 47:14-23.

Tong J, Sommer G, Regitnig P, Holzapfel GA (2011) Dissection properties and mechanical strength of tissue components in human carotid bifurcations. Annals of Biomedical Engineering 39:1703-1719.

Tong J, Xin YF, Xu X, Yang F, Zhang Z (2020) Effect of diabetes mellitus on the dissection properties of the rabbit descending thoracic aortas. Journal of Biomechanics 100:109592.

Tsamis A, Krawiec JT, Vorp DA (2013) Elastin and collagen fibre microstructure of the human aorta in ageing and disease: A review. Journal of The Royal Society Interface 10:20121004.

Tsamis A, Phillippi JA, Koch RG, Pasta S, D'Amore A, Watkins SC, Wagner WR, Gleason TG, Vorp DA (2013) Fiber micro-architecture in the longitudinal-radial and circumferential-radial planes of ascending thoracic aortic aneurysm media. Journal of Biomechanics 46:2787-2794.

Turon A, Dávila CG, Camanho PP, Costa J (2007) An engineering solution for mesh size effects in the simulation of delamination using cohesive zone models. Engineering Fracture Mechanics 74:1665-1682.

Valiaev A, Dong WL, Schmidler S, Clark RL, Chilkoti A, Zauscher S (2008) Hydration and conformational mechanics of single, end-tethered elastin-like polypeptides. Journal of the American Chemical Society 130(33):10939-10946.

Vande Geest JP, Sacks MS, Vorp DA (2004) Age dependency of the biaxial biomechanical behavior of human abdominal aorta. Journal of Biomechanical Engineering 126:815-822.

Vishwanath V, Frank KE, Elmets CA, Dauchot PJ, Monnier VM (1986) Glycation of skin collagen in type I diabetes mellitus: Correlation with long-term complications. Diabetes 35(8):916-921.

Vlassara H, Brownlee M, Cerami A (1986) Nonenzymatic glycosylation: role in the pathogenesis of diabetic complications. Clinical Chemistry 32(10 Suppl):B37-41.

Vorp DA (2007) Biomechanics of abdominal aortic aneurysm. Journal of Biomechanics 40:1887-1902.

Wagenseil JE, Mecham RP (2009) Vascular extracellular matrix and arterial mechanics. Physiological Reviews 89(3):957-989.

Wang L, Roper SM, Hill NA, Luo X (2017) Propagation of dissection in a residually-stressed artery model. Biomechanics and Modeling in Mechanobiology 16:139-149.

Wang MC, Tsai WC, Chen JY, Huang JJ (2005) Stepwise increase in arterial stiffness corresponding with the stages of chronic kidney disease. American Journal of Kidney Diseases 45(3):494-501.

Wang R, Mattson JM, Zhang Y (2023) Effect of aging on the biaxial mechanical behavior of human descending thoracic aorta: Experiments and constitutive modeling considering collagen crosslinking. Journal of the Mechanical Behavior of Biomedical Materials 140:105705.

Wang R, Yu X, Gkousioudi A, Zhang Y (2021a) Effect of glycation on interlamellar bonding of arterial elastin. Experimental Mechanics 61:81-94.

Wang R, Yu X, Zhang Y (2021b) Mechanical and structural contributions of elastin and collagen fibers to interlamellar bonding in the arterial wall. Biomechanics and Modeling in Mechanobiology 20:93-106.

Wang Y, Hahn J, Zhang Y (2018a) Mechanical properties of arterial elastin with water loss. Journal of Biomechanical Engineering 140: 041012.

Wang Y, Johnson JA, Spinale FG, Sutton MA, Lessner SM (2014) Quantitative measurement of dissection resistance in intimal and medial layers of human coronary arteries. Experimental Mechanics 54:677-683.

Wang Y, Li H, Zhang Y (2018b) Understanding the viscoelastic behavior of arterial elastin in glucose via relaxation time distribution spectrum. Journal of the Mechanical Behavior of Biomedical Materials 77:634-641.

Wang Y, Ning J, Johnson JA, Sutton MA, Lessner SM (2011) Development of a quantitative mechanical test of atherosclerotic plaque stability. Journal of Biomechanics 44:2439-2445.

Wang Y, Zeinali-Davarani S, Davis EC, Zhang Y (2015) Effect of glucose on the biomechanical function of arterial elastin. Journal of the Mechanical Behavior of Biomedical Materials 49:244-254.

Watanabe M, Sawai T, Nagura H, Suyama K (1996) Age-related alteration of cross-linking amino acids of elastin in human aorta. The Tohoku Journal of Experimental Medicine 180(2):115-130.

Weisbecker H, Pierce DM, Regitnig P, Holzapfel GA (2012) Layer-specific damage experiments and modeling of human thoracic and abdominal aortas with non-atherosclerotic intimal thickening. Journal of the Mechanical Behavior of Biomedical Materials 12:93-106.

Wenger MPE, Bozec L, Horton MA, Mesquidaz P (2007) Mechanical properties of collagen fibrils. Biophysical Journal 93:1255-1263.

Werbner B, Spack K, O'Connell GD (2019) Bovine annulus fibrosus hydration affects rate-dependent failure mechanics in tension. Journal of Biomechanics 89:34-39.

Wheeler JB, Mukherjee R, Stroud RE, Jones JA, Ikonomidis JS (2015) Relation of murine thoracic aortic structural and cellular changes with aging to passive and active mechanical properties. Journal of the American Heart Association 4(3):e001744.

Whittle MA, Robins SP, Hasleton PS, Anderson JC (1987) Biochemical investigation of possible lesions in human aorta that predispose to dissecting aneurysms: pyridinoline crosslinks. Cardiovascular Research 21(3):161-168.

Willershausen‐Zönnchen B, Lemmen C, Hamn G (1991) Influence of high glucose concentrations on glycosaminoglycan and collagen synthesis in cultured human gingival fibroblasts. Journal of Clinical Periodontology 18(3):190-195.

Winlove CP, Parker KH, Avery NC, Bailey AJ (1996) Interactions of elastin and aorta with sugars in vitro and their effects on biochemical and physical properties. Diabetologia 39:1131-1139.

Wolff SP, Jiang ZY, Hunt JV (1991) Protein glycation and oxidative stress in diabetes mellitus and ageing. Free Radical Biology and Medicine 10(5):339-352.

Wolinsky H, Glagov S (1964) Structural basis for the static mechanical properties of the aortic media. Circulation Research 14(5):400-413.

Wolinsky H, Glagov S (1967) A lamellar unit of aortic medial structure and function in mammals. Circulation Research 20(1):99-111.

Wu KS, van Osdol WW, Dauskardt RH (2006) Mechanical properties of human stratum corneum: Effects of temperature, hydration, and chemical treatment. Biomaterials 27:785-795.

Xuan Y, Wang Z, Guccione JM, Tseng EE, Ge L (2023) Regional and directional delamination properties of healthy human ascending aorta and sinotubular junction. Journal of the Mechanical Behavior of Biomedical Materials 138:105603.

Yu X, Zhang Y (2022) A discrete fiber network finite element model of arterial elastin network considering inter-fiber crosslinking property and density. Journal of the Mechanical Behavior of Biomedical Materials 134:105396.

Yu X, Suki B, Zhang Y (2020) Avalanches and power law behavior in aortic dissection propagation. Science Advances 6(21):eaaz1173.

Yu X, Turcotte R, Seta F, Zhang Y (2018a) Micromechanics of elastic lamellae: unravelling the role of structural inhomogeneity in multi-scale arterial mechanics. Journal of The Royal Society Interface 15(147):20180492.

Yu X, Wang Y, Zhang Y (2018b) Transmural variation in elastin fiber orientation distribution in the arterial wall. Journal of the Mechanical Behavior of Biomedical Materials 77:745-753.

Žagar G, Onck PR, Van Der Giessen E (2015) Two fundamental mechanisms govern the stiffening of cross-linked networks. Biophysical Journal 108(6):1470-1479.

Zeinali-Davarani S, Choi J, Baek S (2009) On parameter estimation for biaxial mechanical behavior of arteries. Journal of Biomechanics 42(4):524-530.

Zeinali-Davarani S, Chow MJ, Turcotte R, Zhang Y (2013) Characterization of biaxial mechanical behavior of porcine aorta under gradual elastin degradation. Annals of Biomedical Engineering 41:1528-1538.

Zeinali-Davarani S, Wang Y, Chow MJ, Turcotte R, Zhang Y (2015) Contribution of collagen fiber undulation to regional biomechanical properties along porcine thoracic aorta. Journal of Biomechanical Engineering 137(5):051001.

Zhang Y, Dunn ML, Drexler ES, McCowan CN, Slifka AJ, Ivy DD, Shandas R (2005) A microstructural hyperelastic model of pulmonary arteries under normo-and hypertensive conditions. Annals of Biomedical Engineering 33(8):1042-1052.

Zhang Y, Dunn ML, Hunter KS, Lanning C, Ivy DD, Claussen L, Chen SJ, Shandas R (2007) Application of a microstructural constitutive model of the pulmonary artery to patient-specific studies: validation and effect of orthotropy. Journal of Biomechanical Engineering 129(2):193-201.

Zhang Y, Lu Q, Feng J, Yu P, Zhang S, Teng Z, Gillard JH, Song R, Jing Z (2014) A pilot study exploring the mechanisms involved in the longitudinal propagation of acute aortic dissection through computational fluid dynamic analysis. Cardiology 128(2):220-225.

Zou Y, Zhang Y (2009) An experimental and theoretical study on the anisotropy of elastin network. Annals of Biomedical Engineering 37:1572-1583.

Zou Y, Zhang Y (2012a) Mechanical evaluation of decellularized porcine thoracic aorta. Journal of Surgical Research 175(2):359-368.

Zou Y, Zhang Y (2012b) The biomechanical function of arterial elastin in solutes. Journal of Biomechanical Engineering 134:071002.

CURRICULUM VITAE